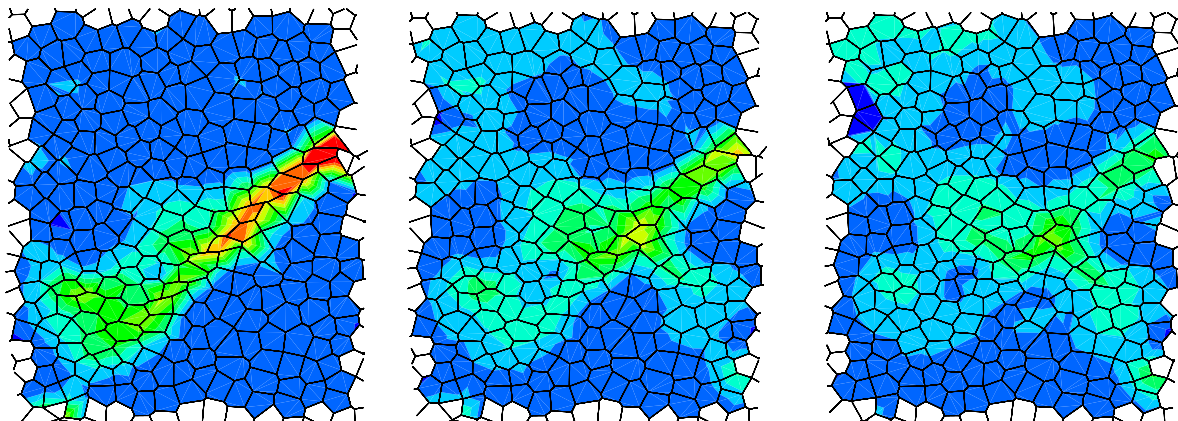


Modeling deformation properties of 2D aluminum foams

Master's thesis

Sietze van Buuren



Supervisors:
K.R. Mangipudi
Prof.dr.ir. P.R. Onck
December 21, 2007



University of Groningen
Zernike Institute
for Advanced Materials

Abstract

A 2D beam model for an open-cell metal foam is used to simulate elastic and plastic deformation of 2D aluminum foams. The results are analysed with the help of strain maps which can visualize the localization of strain in the cellular network. A converged sample size is determined for tension and compression.

Comparison of the solid material parameters with the corresponding foam parameters varying over relative density gives rise to scaling relations. Scaling for the Young's modulus and the plastic collapse strength is confirmed for a unit cell with a bilinear elastic-plastic material. A scaling relation for the plastic modulus of a unit cell with the same material is proposed and discussed. Similar relationships are studied for a Voronoi network with a bilinear material and a material which hardens by a power law. Comparison of the hardening exponent of the foam with the hardening exponent of the solid material showed that the overall hardening behaviour consists of a material contribution due to the strain hardening behaviour of the solid material as well as a geometric contribution due to the reorientation of the cell walls.

The influence of the heat treatments T6-strengthening and annealing is simulated using solid material parameters obtained from experimental results. A preliminary study for failure is performed monitoring the evolution of the internal stresses in the beam elements.

Contents

List of Figures	vii
1 Introduction	1
1.1 Experiments	1
1.2 Simulations	2
2 The model	3
2.1 Equilibrium of the beam element	3
2.2 Kinematics of thin beam deformation	4
2.3 Principle of virtual work	7
2.4 Viscoplastic framework	9
2.5 Coupling	10
2.5.1 Uncoupled model	10
2.5.2 Coupled model	12
3 Program architecture	15
3.1 Voronoi tessellations	15
3.1.1 Network generation	16
3.2 FORTRAN code	17
3.3 Strain mapping	17
4 Sample size effects	21
4.1 Boundary conditions	21
4.2 Tension	23
4.3 Compression	24
4.4 Strain maps: compression and tension	26

5	Hardening effects	27
5.1	Linear hardening	28
5.1.1	Deformation of a strut in an hexagonal unit cell	28
5.1.2	Scaling relationships for regular hexagonal honeycombs	33
5.1.3	Scaling relationships for converged Voronoi networks	39
5.2	Power law hardening	43
5.2.1	Deformation of a strut in an hexagonal unit cell	43
5.2.2	Scaling relationships for regular hexagonal honeycombs	47
5.2.3	Scaling relationships for converged Voronoi networks	48
5.2.4	Strain maps for different hardening exponents	50
5.3	Non-uniform cross-section	54
6	Heat treatments	57
6.1	Definition of the heat treatments	57
6.2	Regular hexagonal honeycombs	59
6.2.1	Deformation of a strut in an hexagonal unitcell	59
6.2.2	Hardening	60
6.3	Converged Voronoi networks	61
6.3.1	Tension versus compression	61
6.3.2	Hardening	62
6.3.3	Failure	62
7	Conclusion	65
7.1	Conclusion	65
7.2	Recommendations	66
8	Acknowledgements	67
	Appendices	69
	References	73

List of Figures

2.1	The foam is modeled using struts, which exist out of 2D beam elements	3
2.2	The 2D beam element	4
2.3	Beam element with nodal quantities and geometrical variables	5
2.4	Transformation of coordinates	8
2.5	A schematic figure of the stress profile for the uncoupled model	11
2.6	A schematic figure of the stress profile for the coupled model	13
3.1	A flowchart of the FORTRAN program	16
3.2	Schematic picture of a part of a 2D foam sample	18
3.3	The different strain map methods	18
3.4	Strain maps for different cell discretizations	20
4.1	The boundary conditions chosen for the Voronoi networks	21
4.2	Compression strain maps for different boundary conditions	22
4.3	Average stress strain curves for different sample sizes in tension	22
4.4	Sample size effect on Young's modulus and the yield stress in tension	23
4.5	Average stress strain curves for different sample sizes in compression	24
4.6	Sample size effect on Young's modulus and the peak stress in compression	24
4.7	Strain maps for tension and compression on a 40×20 Voronoi network	26
5.1	Bilinear response of the foam and the solid material	27
5.2	The unit cell and its (free) boundary conditions	28
5.3	Comparison between coupled model and uncoupled model for linear hardening	30
5.4	Plasticity development for linear hardening and free BC's	31
5.5	Plasticity development for linear hardening and constrained BC's	32
5.6	Deflection of a cell wall in a hexagonal honeycomb structure	33
5.7	Overview of the linear hardening results for the unit cell	34
5.8	Scaling of Young's modulus and the plastic collapse strength for a unit cell	35

5.9	Change in slope of the stress strain curves for relative densities 4%-12%	35
5.10	Change in slope of the stress strain curves for relative densities 16%-24%	36
5.11	Scaling of H^* for the unit cell	36
5.12	Reconstruction of the stress strain curves of the unit cell for linear hardening	37
5.13	Reconstruction of stress strain curve of unit cell for linear hardening in compression	38
5.14	Stress strain curves of a 16×20 Voronoi network with linear hardening	39
5.15	Scaling of Young's modulus and the plastic collapse strength for a voronoi network	40
5.16	Scaling of the plastic modulus for a Voronoi network	40
5.17	Synergy of material and geometrical hardening in the Voronoi network	41
5.18	Comparison of coupled and uncoupled model for power law hardening	42
5.19	Plasticity development, power law hardening, free BC's	43
5.20	Plasticity development, power law hardening, constrained BC's	44
5.21	Solid material curves for different hardening exponents	44
5.22	Stress strain curves for unit cell with different hardening exponents	45
5.23	Stress profiles for different hardening exponents	46
5.24	Plasticity development for different hardening exponents	46
5.25	Stress strain curves of unit cell for different hardening exponents	47
5.26	Hardening exponents versus relative density for the unit cell	48
5.27	Hardening exponents versus relative density for a Voronoi network	49
5.28	Hardening exponents versus relative density for a Voronoi network	49
5.29	Stress strain curves of a Voronoi network for different hardening exponents	50
5.30	Strain maps in tension for different solid material hardening exponents	52
5.31	Strain maps in compression for different solid material hardening exponents	53
5.32	Schematic of the non-uniform cross-section	54
5.33	Comparison between the uniform and non-uniform cross-section	55
5.34	Stress profiles of the unit cell with non-uniform cross-section	56
5.35	Spread of plasticity in the upper strut of the unit cell with non-uniform cross-section	56
6.1	Diagram explaining the used heat treatments, T6-strengthening and annealing	57
6.2	Fitted and experimental stress strain curves in tension for two solid materials	58
6.3	Stress strain curves for the unit cell with T6 and O heat treatment	59
6.4	Stress profiles for the unit cell with T6 and O heat treatment	59
6.5	Spread of plasticity for the unit cell with T6 and O heat treatment	60
6.6	Stress strain curves of the two heat treatments for the unit cell	60

6.7	Hardening exponents versus relative density for different input hardening exponents	61
6.8	Stress strain curves for T6 and O in tension and compression	62
6.9	m^* versus relative density for a Voronoi structure of 16×20 cells	63
6.10	Stress strain curves and damage curves for a Voronoi network in tension	63
6.11	Failure stress and failure strain versus relative density	64
8.1	Stress contour plots for linear hardening with free BC's	69
8.2	Stress contour plots for linear hardening with constrained BC's	70
8.3	Stress contour plots for power law hardening with free BC's	71
8.4	Stress contour plots for power law hardening with constrained BC's	72

1

Introduction

Metal foams have various applications, ranging from light weight sandwich constructions used for example in airplanes to heat exchangers used for example in cooling installations. Light weight properties and a large surface to volume ratio make these materials excellent for these applications. However, in both cases the foam will be subjected to extreme conditions of loading and thermal shocks. To design components which can withstand these conditions, it is needed to understand the mechanical properties of the foam [4].

In this thesis the deformation of foams is studied making use of finite element calculations. This work is part of a collaborative effort with the Material Science group, aimed at understanding the fracture of foams using a combination of modeling and experiments.

1.1 Experiments

Experiments show that a foam sample in compression will deform (after a initial linear elastic reponse) in a ductile manner. Due to plastic hinging at strut junctions struts will orient perpendicular to the loading direction and bands of collapsed cells will occur. These bands will absorb the majority of the deformation partially unloading the remainder of the sample. At large strains the struts will start to touch each other and the foam will start to harden again. This last stage is called densification.

In tension the struts will align parallel to the loading direction and also elongate in this direction. Fracture in the struts is responsible for the final failure. In comparison to compression the strains up to failure are small [1],[2].

To improve certain properties of the foam one can apply different heat treatments to the foam. By heating the foam to different temperatures and cooling it down at different rates, different cell wall microstructures are formed. A change in cell wall microstructure can significantly change the mechanical properties of the foam.

Two different sorts of heat treatments and their influence on the microstructure and mechanical properties are explained in detail in section 6.1. More details on the specification of T6-strengthened and annealed materials and their influence on foam properties are treated in chapter 6.

1.2 Simulations

In this Master's Thesis foams are represented by Voronoi tessellations which form a 2D network of Euler-Bernoulli beams after discretizing all the struts. During a systematic study, linear and power law strain hardening for the solid material is used. The model is capable of capturing gradual plastification of the strut cross-section. A detailed description of this model can be found in chapter 2.

A regular hexagonal honeycomb structure is analyzed through a representative 'unit cell'. For this unit cell scaling relations between material and foam properties were analysed. These relations include the scaling of Young's modulus, the plastic collapse strength and the plastic modulus. Similar relations have been performed for foams. The hardening exponent of foams is compared with the hardening exponent of the solid material for different relative densities.

To make sure boundary effects are not interfering with the results, a converged sample size needed to be found. For compression and tension, converged sample sizes were found by looking at the overall behaviour, Young's modulus, peak stress (in compression) and the yield stress (in tension). The softening behaviour in compression of a foam sample is investigated in further detail with the use of strain maps. Finally, using strain maps a comparison is made between compression and tension.

Results of tensile experiments on T6 and annealed bulk materials were used as input parameters for simulations to investigate the mechanical properties of T6 and annealed foams. This is done for different relative densities. Finally, failure was analysed in tension for both heat treatments. By monitoring the stresses in the beam elements the struts can be assigned as failed when one or more elements exceed a certain failure stress (there is no unloading). A preliminary study for failure is done making use of this method.

2

The model

Making a proper model for single strut deformation is essential for modeling larger foam structures. To describe the 2D elements the Euler-Bernoulli beam theory is used. A viscoplastic framework is used to incorporate plasticity. Finally, a coupled model to incorporate the coupling of curvature and axial straining is described.

2.1 Equilibrium of the beam element

Open cell foams are a simple network with neighbouring nodes connected through struts. In the model these struts consist of 2D beam elements (See figure 2.1).

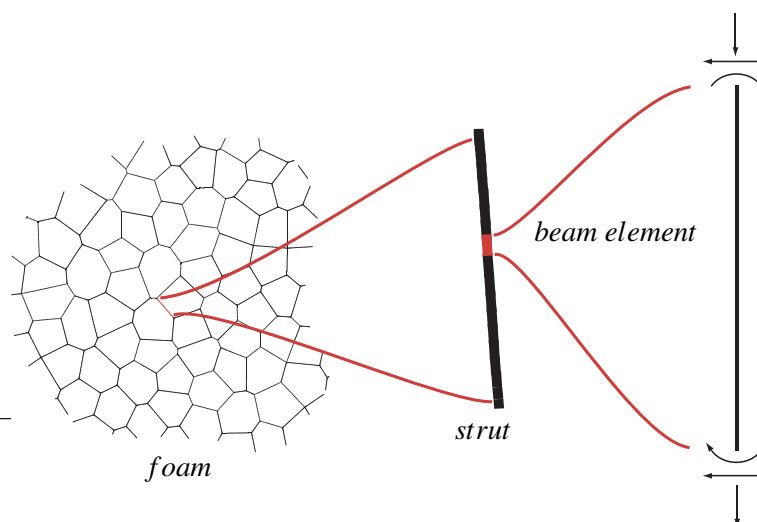


Figure 2.1: The foam is modeled using struts, which exist of 2D beam elements.

Each node of a beam element has three degrees of freedom: two displacements (\hat{u}_i, \hat{v}_i) and a rotation ($\hat{\phi}_i$). The corresponding forces and moment are denoted respectively as $f_{\hat{x}_i}, f_{\hat{y}_i}$ and \hat{m}_i , where i is

the node number. The (^) is used to indicate that the variable is local. The quantities are organized in two nodal vectors $\hat{\mathbf{u}}$ and $\hat{\mathbf{f}}$:

$$\hat{\mathbf{u}} = \begin{bmatrix} \hat{u}_1 \\ \hat{v}_1 \\ \hat{\phi}_1 l_0 \\ \hat{u}_2 \\ \hat{v}_2 \\ \hat{\phi}_2 l_0 \end{bmatrix}, \quad \hat{\mathbf{f}} = \begin{bmatrix} f_{\hat{x}_1} \\ f_{\hat{y}_1} \\ \hat{m}_1/l_0 \\ f_{\hat{x}_2} \\ f_{\hat{y}_2} \\ \hat{m}_2/l_0 \end{bmatrix} \quad (2.1)$$

For numerical reasons the rotational degrees of freedom are scaled by a reference length (l_0) which is the average strut length.

If an external force $\hat{\mathbf{f}}$ is acting on the beam element in figure 2.2a and there are no distributed forces acting on the element, then the external virtual work of the beam element is

$$\begin{aligned} \delta W_e &= \hat{f}_i \delta \hat{u}_i \\ &= f_{\hat{x}_1} \delta \hat{u}_1 + f_{\hat{x}_2} \delta \hat{u}_2 + \hat{m}_1 \delta \hat{\phi}_1 + f_{\hat{y}_1} \delta \hat{v}_1 + f_{\hat{y}_2} \delta \hat{v}_2 + \hat{m}_2 \delta \hat{\phi}_2. \end{aligned} \quad (2.2)$$

The external equilibrium of the element yields:

$$f_{\hat{x}_1} + f_{\hat{x}_2} = 0, \quad (2.3)$$

$$f_{\hat{y}_1} + f_{\hat{y}_2} = 0, \quad (2.4)$$

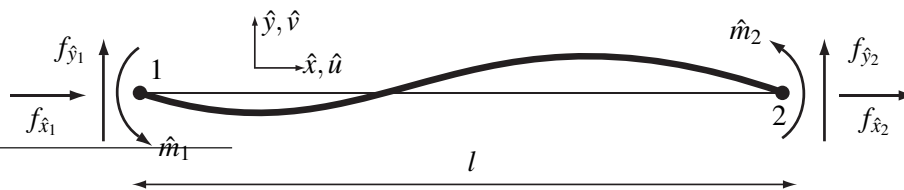
$$\hat{m}_1 + \hat{m}_2 + f_{\hat{y}_2} l = 0, \quad (2.5)$$

where l is the length of the element. Equation (2.2) can be rewritten with the help of equation (2.3)-(2.5) to

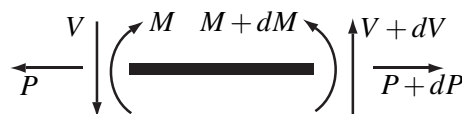
$$\delta W_e = f_{\hat{x}_2} (\delta \hat{u}_2 - \delta \hat{u}_1) + f_{\hat{y}_1} (\delta \hat{v}_2 - \delta \hat{v}_1 + \delta \hat{\phi}_1 l) + \hat{m}_2 (\delta \hat{\phi}_2 - \delta \hat{\phi}_1). \quad (2.6)$$

2.2 Kinematics of thin beam deformation

Making use of the Euler-Bernoulli beam theory the constitutive behaviour of the beam element is derived. The differential equations governing the linear elastic deformation of the thin beam under



(a) The beam element with nodal forces and moments.



(b) Infinitesimal part of the beam element with forces and moments.

Figure 2.2: The 2D beam element.

consideration are:

$$EA \frac{d^2 \hat{u}}{d\hat{x}^2} = 0, \quad (2.7)$$

$$EI \frac{d^4 \hat{v}}{d\hat{x}^4} = 0. \quad (2.8)$$

In these equations A stands for the area of the cross-section of the beam, E is Young's modulus and I is the moment of inertia. These equations give rise to the following relations respectively for transverse deflection and axial displacement.

$$\hat{v}(\hat{x}) = a_0 + a_1 \hat{x} + a_2 \hat{x}^2 + a_3 \hat{x}^3, \quad (2.9)$$

$$\hat{u}(\hat{x}) = b_0 + b_1 \hat{x}. \quad (2.10)$$

Requiring these equations to satisfy the proper boundary conditions, $\hat{v}(\hat{x})$ and $\hat{u}(\hat{x})$ can be expressed as functions of the nodal degrees of freedom. Applying the boundary conditions $\hat{u}(0) = u_{\hat{x}_1}$ and $\hat{u}(l) = u_{\hat{x}_2}$ to equation (2.10) results in

$$\hat{u}(\hat{x}) = [N_{u,1}(\hat{x}) \quad N_{u,2}(\hat{x})] \begin{bmatrix} \hat{u}_1 \\ \hat{u}_2 \end{bmatrix}, \quad (2.11)$$

where

$$N_{u,1}(\hat{x}) = 1 - \hat{x}/l, \quad (2.12)$$

$$N_{u,2}(\hat{x}) = \hat{x}/l. \quad (2.13)$$

If one applies the boundary conditions $\hat{v}(0) = u_{\hat{y}_1}$, $\hat{v}(l) = u_{\hat{y}_2}$, $\frac{d\hat{v}}{d\hat{x}}(0) = \hat{\phi}_1$ and $\frac{d\hat{v}}{d\hat{x}}(l) = \hat{\phi}_2$ to equation (2.9), the result is

$$\hat{v}(\hat{x}) = [N_{v,1}(\hat{x}) \quad N_{v,2}(\hat{x}) \quad N_{v,3}(\hat{x}) \quad N_{v,4}(\hat{x})] \begin{bmatrix} \hat{v}_1 \\ \hat{\phi}_1 l \\ \hat{v}_2 \\ \hat{\phi}_2 l \end{bmatrix}, \quad (2.14)$$

where

$$N_{v,1}(\hat{x}) = \frac{1}{l^3} (2\hat{x}^3 - 3\hat{x}^2 + l^3), \quad (2.15)$$

$$N_{v,2}(\hat{x}) = \frac{1}{l^3} (\hat{x}^3 l - 2\hat{x} l^2 + \hat{x} l^3), \quad (2.16)$$

$$N_{v,3}(\hat{x}) = \frac{1}{l^3} (-2\hat{x}^3 + 3\hat{x}^2 l), \quad (2.17)$$

$$N_{v,4}(\hat{x}) = \frac{1}{l^3} (\hat{x}^3 l - \hat{x}^2 l^2). \quad (2.18)$$

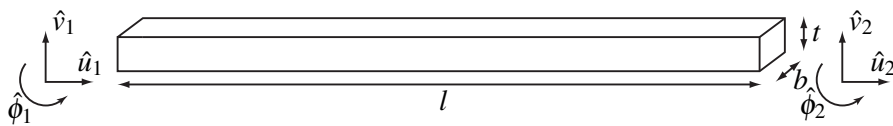


Figure 2.3: Beam element with nodal quantities and geometrical variables.

Equations (2.12)-(2.13) and (2.15)-(2.18) are the shape functions. The nodal quantities and geometric variables are explained in figure 2.3. Euler-Bernoulli beam theory also describes that

$$AE \frac{du}{dx} = P, \quad (2.19)$$

$$EI \frac{d^2 \hat{v}}{d\hat{x}^2} = EI \kappa = M, \quad (2.20)$$

$$EI \frac{d^3 \hat{v}}{d\hat{x}^3} = V. \quad (2.21)$$

Used in combination with the nodal displacement $\hat{\mathbf{u}}$ expressions for $f_{\hat{x}_2}$, $f_{\hat{y}_1}$, \hat{m}_1 and \hat{m}_2 can be obtained. The axial force in the beam is

$$f_{\hat{x}_2} = \frac{AE}{l} (\hat{u}_2 - \hat{u}_1) \quad (2.22)$$

and the shear force in the beam is

$$f_{\hat{y}_1} = \frac{EI}{l^3} (12\hat{v}_1 + 6l\hat{\phi}_1 - 12\hat{v}_2 + 6l\hat{\phi}_2). \quad (2.23)$$

The bending moment at the first node and respectively the second node of the beam are

$$\hat{m}_1 = M(\hat{x} = 0) = \frac{EI}{l^3} (6l\hat{v}_1 + 4l^2\hat{\phi}_1 - 6l\hat{v}_2 + 2l^2\hat{\phi}_2l), \quad (2.24)$$

$$\hat{m}_2 = M(\hat{x} = l) = \frac{EI}{l^3} (6l\hat{v}_1 + 2l^2\hat{\phi}_1 - 6l\hat{v}_2 + 4l^2\hat{\phi}_2l). \quad (2.25)$$

Now $f_{\hat{x}_2} = P$, $f_{\hat{y}_1} = V$ and $\hat{m}_2 = M(\hat{x} = l)$ are chosen as the generalized stresses:

$$\hat{\mathbf{s}} = \begin{bmatrix} \hat{s}_1 \\ \hat{s}_2 \\ \hat{s}_3 \end{bmatrix} = \begin{bmatrix} f_{\hat{x}_2} \\ f_{\hat{y}_1} \\ \hat{m}_2/l \end{bmatrix}. \quad (2.26)$$

The generalized stresses can be rewritten to the following:

$$\hat{s}_1 = \frac{EA}{l} (\hat{u}_2 - \hat{u}_1), \quad (2.27)$$

$$\hat{s}_2 = 12 \frac{EI}{l^3} (\hat{v}_1 - \hat{v}_2 + \hat{\phi}_1 l) + 6 \frac{EI}{l^3} (\hat{\phi}_2 - \hat{\phi}_1) l, \quad (2.28)$$

$$\hat{s}_3 = 6 \frac{EI}{l^3} (\hat{v}_1 - \hat{v}_2 + \hat{\phi}_1 l) + 4 \frac{EI}{l^3} ((\hat{\phi}_2 - \hat{\phi}_1) l), \quad (2.29)$$

from which the generalized strains can be extracted. This results in

$$\hat{\mathbf{e}} = \begin{bmatrix} \hat{e}_1 \\ \hat{e}_2 \\ \hat{e}_3 \end{bmatrix} = \begin{bmatrix} \hat{u}_2 - \hat{u}_1 \\ \hat{v}_1 - \hat{v}_2 + \hat{\phi}_1 l \\ (\hat{\phi}_2 - \hat{\phi}_1) l \end{bmatrix}. \quad (2.30)$$

From the generalized stresses and strains the following stress-strain relation can be derived

$$\hat{s}_1 = \frac{EA}{l} \hat{e}_1, \quad (2.31)$$

$$\hat{s}_2 = 12 \frac{EI}{l^3} \hat{e}_2 + 6 \frac{EI}{l^3} \hat{e}_3, \quad (2.32)$$

$$\hat{s}_3 = 6 \frac{EI}{l^3} \hat{e}_2 + 4 \frac{EI}{l^3} \hat{e}_3, \quad (2.33)$$

which is in matrix form

$$\begin{bmatrix} \hat{s}_1 \\ \hat{s}_2 \\ \hat{s}_3 \end{bmatrix} = \begin{bmatrix} AE/l & 0 & 0 \\ 0 & 12EI/l^3 & 6EI/l^3 \\ 0 & 6EI/l^3 & 4EI/l^3 \end{bmatrix} \begin{bmatrix} \hat{e}_1 \\ \hat{e}_2 \\ \hat{e}_3 \end{bmatrix} = \hat{\mathbf{C}}\hat{\mathbf{e}}. \quad (2.34)$$

Equation (2.34) describes the constitutive behaviour at a local level. $\hat{\mathbf{C}}$ is called the local stiffness tensor, it captures the constitutive behaviour.

With the nodal displacement vector and the chosen generalized strains the strain to displacement relationship can be written as

$$\hat{\mathbf{e}} = \hat{\mathbf{B}}\hat{\mathbf{u}}, \quad (2.35)$$

where

$$\hat{\mathbf{B}} = \begin{bmatrix} -1 & 0 & 0 & 1 & 0 & 0 \\ 0 & 1 & l/l_0 & 0 & -1 & 0 \\ 0 & 0 & -l/l_0 & 0 & 0 & l/l_0 \end{bmatrix}. \quad (2.36)$$

In the case of inelastic deformation the total strain is the sum of an elastic and an inelastic strain:

$$\hat{\mathbf{e}} = \hat{\mathbf{e}}^{\text{el}} + \hat{\mathbf{e}}^*, \quad (2.37)$$

where the inelastic part has a plastic and an optional fracture component (e.g. $\hat{\mathbf{e}}^* = \hat{\mathbf{e}}^{\text{pl}} + \hat{\mathbf{e}}^{\text{fr}}$).

In the following section equation (2.34), (2.35) and (2.37) are used with the weak form of equilibrium in discrete form to come to a final expression for our finite element framework.

2.3 Principle of virtual work

The principle of virtual work is

$$(\delta\hat{\mathbf{e}})^T \hat{\mathbf{s}} = (\delta\hat{\mathbf{u}})^T \hat{\mathbf{f}}. \quad (2.38)$$

Taking the time derivative one obtains the incremental principle of virtual work

$$(\delta\hat{\mathbf{e}})^T \dot{\hat{\mathbf{s}}} + (\delta\dot{\hat{\mathbf{e}}})^T \hat{\mathbf{s}} = (\delta\dot{\hat{\mathbf{u}}})^T \hat{\mathbf{f}}. \quad (2.39)$$

The relations for stress-strain and its time derivative (making use of equation (2.35)) are given respectively by:

$$\hat{\mathbf{s}} = \hat{\mathbf{C}}\hat{\mathbf{e}}^{\text{el}} \quad (2.40)$$

$$\dot{\hat{\mathbf{s}}} = \hat{\mathbf{C}}\dot{\hat{\mathbf{e}}}^{\text{el}} = \hat{\mathbf{C}}(\dot{\hat{\mathbf{e}}} - \dot{\hat{\mathbf{e}}}^*) = \hat{\mathbf{C}}(\hat{\mathbf{B}}\dot{\hat{\mathbf{u}}} - \dot{\hat{\mathbf{e}}}^*) = \hat{\mathbf{C}}(\mathbf{B}\dot{\mathbf{u}} - \dot{\hat{\mathbf{e}}}^*) \quad (2.41)$$

The last equality holds because $\hat{\mathbf{u}} = \mathbf{T}\mathbf{u}$ and $\mathbf{B} = \hat{\mathbf{B}}\mathbf{T}$. Here \mathbf{T} is a transformation matrix, which transforms the coordinates from a rotated frame of reference under an arbitrary angle θ to a global frame of reference (please see figure 2.4). This transformation matrix \mathbf{T} will look like

$$\mathbf{T} = \begin{bmatrix} C & S & 0 & 0 & 0 & 0 \\ -S & C & 0 & 0 & 0 & 0 \\ 0 & 0 & 1 & 0 & 0 & 0 \\ 0 & 0 & 0 & C & S & 0 \\ 0 & 0 & 0 & -S & C & 0 \\ 0 & 0 & 0 & 0 & 0 & 1 \end{bmatrix}, \quad (2.42)$$

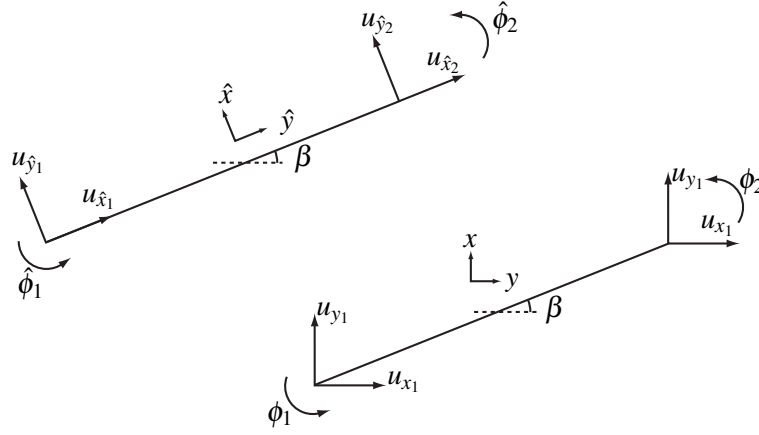


Figure 2.4: Transformation of coordinates. The 2D beam element is rotated at an arbitrary angle. The upper left beam element has coordinates in a local frame reference, while the bottom right element's coordinates are transformed to a global frame of reference.

where $C = \cos \beta$ and $S = \sin \beta$. Using \mathbf{T} one can transform for example $\hat{\mathbf{B}}$ to

$$\mathbf{B} = \hat{\mathbf{B}}\mathbf{T} = \begin{bmatrix} -C & -S & 0 & C & S & 0 \\ -S & C & l/l_0 & S & -C & 0 \\ 0 & 0 & -l/l_0 & 0 & 0 & l/l_0 \end{bmatrix}. \quad (2.43)$$

Because an updated Lagrangian scheme is used $\mathbf{u} = \mathbf{0}$ and equation (2.41) changes to

$$\hat{\mathbf{s}} = \hat{\mathbf{C}}(\dot{\mathbf{B}}\mathbf{u}^{\text{el}} + \mathbf{B}\dot{\mathbf{u}}^{\text{el}}) = \hat{\mathbf{C}}\mathbf{B}\dot{\mathbf{u}}^{\text{el}}. \quad (2.44)$$

We can now rewrite equation (2.39) making use of (2.37) and de previous equation to

$$(\delta\mathbf{u})^T \mathbf{k}_e \dot{\mathbf{u}} - (\delta\hat{\mathbf{e}})^T \hat{\mathbf{C}}\hat{\mathbf{e}}^* + (\delta\hat{\mathbf{e}})^T \hat{\mathbf{s}} = (\delta\dot{\mathbf{u}})^T \hat{\mathbf{f}}, \quad (2.45)$$

where $\mathbf{k}_e = \mathbf{B}^T \mathbf{C} \mathbf{B}$. Here \mathbf{k}_e will look like

$$\mathbf{k}_e = \begin{bmatrix} \tau C^2 + 12\xi S^2 & (\tau - 12\xi)CS & -6\tau Sl/l_0 & -\tau C^2 - 12\xi S^2 & (12\xi - \tau)CS & -6\tau Sl/l_0 \\ & \tau S^2 + 12\xi C^2 & 6\tau Cl/l_0 & (12\xi - \tau)CS & -\tau S^2 - 12\xi C^2 & 6\tau Cl/l_0 \\ & & 4\tau l^2/l_0^2 & 6\tau Sl/l_0 & -6\tau Sl/l_0 & 2\tau l^2/l_0^2 \\ & & & \tau C^2 + 12\xi S^2 & (\tau - 12\xi)CS & 6\tau Sl/l_0 \\ & & & & \tau S^2 + 12\xi C^2 & -6\tau Sl/l_0 \\ & & & & & 4\tau l^2/l_0^2 \end{bmatrix}, \quad (2.46)$$

symmetry

where $\tau = \frac{EA}{l}$ and $\xi = \frac{EI}{l^3}$. The last part on the left hand side of equation (2.45) gives rise to a geometric stiffness considering non-linear expressions in the axial terms. We take for the geometric stiffness matrix

$$\mathbf{k}_g = \begin{bmatrix} 0 & c_1 S & c_s S & 0 & -c_1 S & c_2 S \\ 0 & c_1 C & c_s C & 0 & -c_1 C & c_2 C \\ 0 & c_2 & c_3 & 0 & -c_2 & -c_4 \\ 0 & -c_1 S & -c_2 S & 0 & c_1 S & -c_2 S \\ 0 & -c_1 C & -c_2 C & 0 & c_1 C & -c_2 C \\ 0 & c_2 & -c_4 & 0 & -c_2 & c_3 \end{bmatrix}, \quad (2.47)$$

where $c_1 = \frac{6}{5} \frac{\hat{s}_1}{l}$, $c_2 = \frac{1}{10} \frac{\hat{s}_1}{l_0}$, $c_3 = \frac{2}{15} \hat{s}_1 \frac{l}{l_0^2}$ and $c_4 = \frac{1}{30} \hat{s}_1 \frac{l}{l_0^2}$.

With these rearrangements equations (2.45) becomes

$$(\delta \mathbf{u})^T \left[(\mathbf{k}_e + \mathbf{k}_g) \dot{\mathbf{u}} - \mathbf{B}^T \hat{\mathbf{C}} \dot{\hat{\mathbf{e}}}^* \right] = (\delta \mathbf{u})^T \dot{\mathbf{f}}. \quad (2.48)$$

The problem with this equation is that the inelastic strain rate is required at the current time step. The assumption is made that plasticity is the limit of power law creep. Then the inelastic strain component in equation (2.48) can be incrementally computed at every timestep and this allows the model for implementation in a linear finite element framework. Proceeding in this manner equation (2.48) can be written in the form

$$\mathbf{k} \dot{\mathbf{u}} = \dot{\mathbf{f}} + \dot{\mathbf{f}}^*. \quad (2.49)$$

In literature \mathbf{k} usually is referred to as the local stiffness matrix

$$\mathbf{k} = \mathbf{k}_e + \mathbf{k}_g \quad (2.50)$$

and $\dot{\mathbf{f}}^*$ is the viscoplastic force:

$$\dot{\mathbf{f}}^* = \mathbf{B}^T \hat{\mathbf{C}} \dot{\hat{\mathbf{e}}}^*. \quad (2.51)$$

Finally, one can arrive at the following finite element equations for the whole system by element assembly

$$\mathbf{K} \Delta \mathbf{U} = \Delta \mathbf{F}, \quad (2.52)$$

where \mathbf{K} is the global stiffness matrix:

$$\mathbf{K} = \bigwedge_{n=1}^N (\mathbf{k}_g^{(n)} + \mathbf{k}_e^{(n)}) \quad (2.53)$$

and

$$\Delta \mathbf{F} = \bigwedge_{n=1}^N (\Delta \mathbf{f}^{(n)} + \Delta \mathbf{f}^{*(n)}), \quad (2.54)$$

where N is the total number of elements and n refers to the element number. The \bigwedge -symbol indicates the assembly of the global stiffness matrix and force vector.

2.4 Viscoplastic framework

Before solving the finite element equation to get the unknown displacements one needs to calculate the viscoplastic force. For this the inelastic strain rates are needed.

A computationally convenient way around the time independent nature of plasticity is to use a viscoplastic formulation. Here, a creep law is used, which approaches time independent plasticity as the creep exponent (n) approaches infinity. Emphasized needs to be the fact that this creep law is only used as a numerical tool. It has nothing to do with the physical phenomenon creep.

The creep law for the axial strain is

$$\dot{\epsilon}_x = \dot{\epsilon}_0 \left(\frac{\sigma_x}{\sigma_0} \right)^n. \quad (2.55)$$

The creep exponent must be an odd integer, $n = 101$ turns out to be sufficient. Assuming that the assumptions for the Euler-Bernouli theory still hold during plastic deformation, using $\dot{\varepsilon}_x^{vp} = y\dot{\kappa}^{vp}$ equation (2.55) can be rewritten to

$$\sigma_x^{vp} = \sigma_0 \left(\frac{y\dot{\kappa}^{vp}}{\dot{\varepsilon}_0} \right)^{\frac{1}{n}} \quad (2.56)$$

For a beam with a rectangular cross-section with thickness t and out-of-plane thickness b the moment can be calculated using $M = \int_{-t/2}^{t/2} \sigma_x y dA$, resulting in

$$M = \frac{t^2 \sigma_0 b}{2} \frac{n}{2n+1} \left(\frac{t}{2\dot{\varepsilon}_0} \dot{\kappa}^{vp} \right)^{\frac{1}{n}}. \quad (2.57)$$

If this expression is rearranged one can obtain a relation for the local curvature rate

$$\dot{\kappa} = \dot{\kappa}_0 \left(\frac{M}{M_0} \right)^n, \quad (2.58)$$

where

$$M_0 = \frac{t^2 \sigma_0 b}{2} \frac{n}{2n+1} \quad \text{and} \quad \dot{\kappa}_0 = \frac{\dot{\varepsilon}_0}{2}. \quad (2.59)$$

If $n \rightarrow \infty$, M_0 is the ‘‘plastic moment’’, corresponding to the yielding of the complete cross-section and $M_p = t^2 \sigma_0 b / 4 = M_0$.

2.5 Coupling

In this section the Gibson and Ashby (G&A) model for plastic buckling of foams is improved. The G&A model assumes that complete yielding of the beam cross-section occurs instantaneous when the yield stress is reached. The gradual transition from a fully elastic to a partial elastic element and partial plastic to a fully plastic element is ignored. No hardening is taken care of while considering coupling between axial and bending strains. In the used model both mechanisms are incorporated into a non-layered model. A description is given for a coupled and an uncoupled model. The latter is described because it is used for scaling relationships described in chapter 5. In the coupled model the influence of axial strain is taken into account for moment calculation, where as in the uncoupled the stress profile always remains symmetric. One will also find a detailed comparison of both models in chapter 5.

2.5.1 Uncoupled model

The incorporation of the gradual plastification of the beam element is an important improvement compared to the G&A model.

In figure 2.5 a schematic representation is shown of the stress profile for a beam element to which an arbitrary moment is applied.

For the uncoupled case the axial strain of a horizontal fiber is related to the curvature through

$$\varepsilon_x(y) = -\kappa y, \quad (2.60)$$

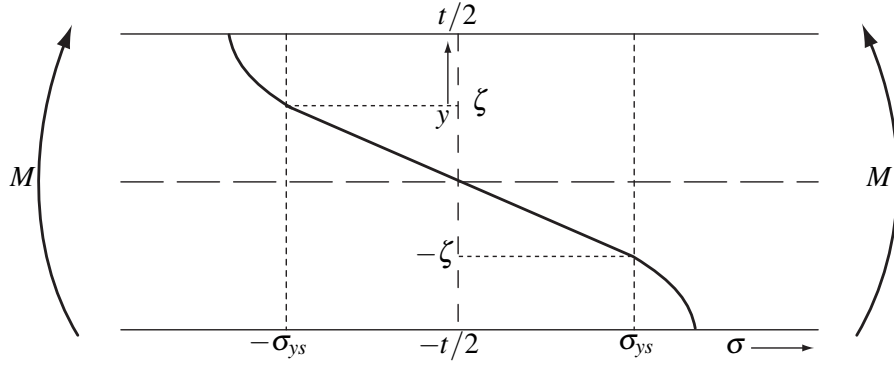


Figure 2.5: A schematic figure of the stress profile for the uncoupled model. This is the stress profile for power law hardening.

where κ is the curvature of the beam along the neutral axis. The moment and the axial force for any cross-section is obtained by integrating the stress $\sigma(y)$ over the thickness of the beam. The assumption is made that these relations also hold during plastic deformation.

For the axial stress with linear hardening the following relations during elasticity and plasticity are used.

$$\sigma = \begin{cases} E\varepsilon & \text{for } 0 \leq |\varepsilon| \leq \varepsilon_{ys} \\ \text{sign}(\varepsilon)(\sigma_{ys}(1 - \gamma) + H|\varepsilon|) & \text{for } |\varepsilon| > \varepsilon_{ys} \end{cases} \quad (2.61)$$

and for power law hardening these equations are

$$\sigma = \begin{cases} E\varepsilon & \text{for } 0 \leq |\varepsilon| \leq \varepsilon_{ys} \\ \text{sign}(\varepsilon)\sigma_{ys}(1 + E/\sigma_{ys}(|\varepsilon| - \varepsilon_{ys}))^m & \text{for } |\varepsilon| > \varepsilon_{ys} \end{cases}, \quad (2.62)$$

where $\varepsilon_{ys} (= \sigma_{ys}/E)$ represents the yield strain, m the hardening exponent and $\gamma = H/E$ in which H is the plastic modulus. The onset of plasticity occurs when the top and bottom fiber reaches the yield stress (this will happen at the same instant, because the stress profile is symmetric). From now on the beam will have a plastic shell and an elastic core. Depending on the bending moment the spread of plasticity and the size of the elastic core will differ. If the moment increases the elastic core will shrink. As $\kappa \rightarrow \infty$ the elastic core diminishes to a single neutral fiber of infinitesimal thickness.

According to this the moment for linear hardening will be

$$M = -2b \int_0^{t/2} \sigma_x(y) y dy \quad (2.63)$$

$$= -2b \left(\int_0^{\zeta} E \kappa y^2 + \int_{\zeta}^{t/2} \text{sign}(|\varepsilon|)(\sigma_{ys}(1 - \gamma) + H|\varepsilon|) y dy \right) \quad (2.64)$$

and the moment for power law hardening is

$$M = -2b \left(\int_0^{\zeta} E \kappa y^2 + \int_{\zeta}^{t/2} \text{sign}(|\bar{\varepsilon}|)\sigma_{ys}(1 + E/\sigma_{ys}(|\bar{\varepsilon}| - \varepsilon_{ys}))^m y dy \right), \quad (2.65)$$

which consists out of a plastic and an elastic part. The stress $\sigma_x(y)$ in the equations is the stress from respectively equation (2.61) and (2.62) as function of the axial strain: $\sigma_x(y) = \sigma(\varepsilon_x(y))$. Boundary between the elastic and the plastic region of the beam is $\zeta = -\frac{t}{2} \frac{\kappa_0}{\kappa}$. In these functions κ_0 is the

curvature at the onset of yielding. This results in the final expression for the moment with linear hardening

$$M(\kappa) = \begin{cases} EI\kappa & \text{for } 0 \leq |\kappa| \leq |\kappa_0| \\ EI\kappa \left((1 + \gamma) \left(\frac{\kappa_0}{\kappa} \right)^3 + \gamma \right) + \text{sign}(\kappa) M_p (1 - \gamma) \left(1 - \left(\frac{\kappa_0}{\kappa} \right)^2 \right) & \text{for } |\kappa| > |\kappa_0| \end{cases} \quad (2.66)$$

and the moment with power law hardening

$$M(\kappa) = \begin{cases} EI\kappa & \text{for } 0 \leq |\kappa| \leq |\kappa_0| \\ EI\kappa \left(\frac{\kappa_0}{\kappa} \right)^3 + \text{sign}(\kappa) \frac{2}{2+m} M_p \left(\frac{\kappa_0}{\kappa} \right)^m \left(1 - \left(\frac{\kappa_0}{\kappa} \right)^{2+m} \right) & \text{for } |\kappa| > |\kappa_0| \end{cases}, \quad (2.67)$$

which are functions of the curvature κ and where $M_p = \frac{1}{4} b t^2 \sigma_{ys}$.

The force is calculated through $P = 2b \int_0^{t/2} \sigma(\bar{\varepsilon}) dy$, where $\sigma(\bar{\varepsilon})$ refers to linear hardening and power law hardening respectively from equation (2.61) and (2.62). This results in

$$P(\bar{\varepsilon}) = \begin{cases} EA\bar{\varepsilon} & \text{for } 0 \leq |\bar{\varepsilon}| \leq \varepsilon_{ys} \\ \text{sign}(\varepsilon) (\sigma_{ys} (1 - \gamma) + H |\bar{\varepsilon}|) A & \text{for } |\bar{\varepsilon}| > \varepsilon_{ys} \end{cases} \quad (2.68)$$

for linear hardening and

$$P(\bar{\varepsilon}) = \begin{cases} EA\bar{\varepsilon} & \text{for } 0 \leq |\bar{\varepsilon}| \leq \varepsilon_{ys} \\ \sigma_{ys} \text{sign}(\bar{\varepsilon}) (1 + E/\sigma_{ys} (|\bar{\varepsilon}| - \varepsilon_{ys}))^m A & \text{for } |\bar{\varepsilon}| > \varepsilon_{ys} \end{cases} \quad (2.69)$$

for power law hardening, which are a function only of the axial strain $\bar{\varepsilon}$. Here A is the area of the cross-section of the beam element.

2.5.2 Coupled model

The coupled model also takes into account the effect of axial straining on the moment and curvature on the axial force. Therefore, the function for axial strain inside the beam element changes to

$$\varepsilon_x(y) = \bar{\varepsilon} - \kappa y. \quad (2.70)$$

Now both the force and moment expression will depend on κ and $\bar{\varepsilon}$ i.e. $P(\bar{\varepsilon}, \kappa)$ and $M(\bar{\varepsilon}, \kappa)$. The same constitutive law for the material is used (equation (2.62)), but now as a function of the strain $\varepsilon_x(y)$ from equation (2.70).

For the uncoupled model the stress and strain profiles remain symmetric, however, for the the coupled model this is not anymore the case. Because of this the integral has to be divided in three parts. One part for the top plastic fibers, one part for the elastic core and part for the bottom plastic fibers. During the calculation one needs to closely track the boundaries between elastic and plastic regions (ζ^{\oplus} and ζ^{\ominus} , see figure 2.6). For example, it can occur that there are only top plastic (or bottom plastic) fibers. If this happens one part of the integral should be left out in the calculation. Another possibility is that the complete cross-section started yielding. For this case only one part of the integral needs to be calculated. All of these exceptions are taken care of in the code.

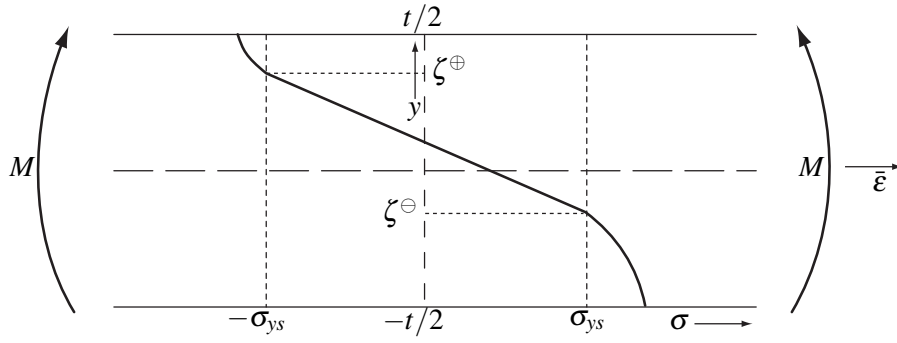


Figure 2.6: A schematic figure of the stress profile for the coupled model.

The complete integral is divided into three parts

$$M(\bar{\epsilon}, \kappa) = -b \int_{-t/2}^{t/2} \sigma_x(y) y dy \quad (2.71)$$

$$\begin{aligned} &= -b \left(\int_{-t/2}^{\zeta^{\ominus}} \text{sign}(\epsilon_x(y)) \sigma_{ys} (1 + \alpha(|\epsilon_x(y)| - \epsilon_{ys}))^m y dy \right. \\ &\quad + \int_{\zeta^{\ominus}}^{\zeta^{\oplus}} E \epsilon_x(y) y dy \\ &\quad \left. + \int_{\zeta^{\oplus}}^{t/2} \text{sign}(\epsilon_x(y)) \sigma_{ys} (1 + \alpha(|\epsilon_x(y)| - \epsilon_{ys}))^m y dy \right), \end{aligned} \quad (2.72)$$

which finally becomes

$$\begin{aligned} M(\bar{\epsilon}, \kappa) &= -b \left(\frac{\sigma_{ys}}{(m+1)\alpha\kappa} \left(- (1 + \alpha(|\bar{\epsilon} + \kappa \frac{t}{2}| - \epsilon_{ys}))^{m+1} \frac{t}{2} - (1 + \alpha(|\bar{\epsilon} - \kappa \zeta^{\ominus}| - \epsilon_{ys}))^{m+1} \zeta^{\ominus} \right) \right. \\ &\quad + \frac{\sigma_{ys} \text{sign}(\bar{\epsilon} + \kappa \frac{t}{2})}{(m+1)(m+2)\alpha^2 \kappa^2} \left((1 + \alpha(|\bar{\epsilon} + \kappa \frac{t}{2}| - \epsilon_{ys}))^{m+2} - (1 + \alpha(|\bar{\epsilon} - \kappa \zeta^{\ominus}| - \epsilon_{ys}))^{m+2} \right) \\ &\quad + E \left(\frac{\kappa}{3} (\zeta^{\ominus 3} - \zeta^{\oplus 3}) + \frac{\bar{\epsilon}}{2} (\zeta^{\oplus 2} - \zeta^{\ominus 2}) \right) \\ &\quad + \frac{\sigma_{ys}}{(m+1)\alpha\kappa} \left((1 + \alpha(|\bar{\epsilon} - \kappa \zeta^{\oplus}| - \epsilon_{ys}))^{m+1} \zeta^{\oplus} - (1 + \alpha(|\bar{\epsilon} - \kappa \frac{t}{2}| - \epsilon_{ys}))^{m+1} \frac{t}{2} \right) \\ &\quad \left. + \frac{\sigma_{ys} \text{sign}(\bar{\epsilon} - \kappa \frac{t}{2})}{(m+1)(m+2)\alpha^2 \kappa^2} \left((1 + \alpha(|\bar{\epsilon} - \kappa \zeta^{\oplus}| - \epsilon_{ys}))^{m+2} - (1 + \alpha(|\bar{\epsilon} - \kappa \frac{t}{2}| - \epsilon_{ys}))^{m+2} \right) \right), \end{aligned} \quad (2.73)$$

where $\alpha = E/\sigma_{ys}$, $\zeta^{\oplus} = \frac{\sigma_{ys}}{|\kappa|E} + \text{sign}(\kappa\bar{\epsilon}) \left| \frac{\bar{\epsilon}}{\kappa} \right|$ and $\zeta^{\ominus} = -\frac{\sigma_{ys}}{|\kappa|E} + \text{sign}(\kappa\bar{\epsilon}) \left| \frac{\bar{\epsilon}}{\kappa} \right|$. The first two lines of equation (2.73) correspond to the plastic top fibers, the third line represents the elastic core and the last two lines correspond to the plastic bottom fibers.

The force is calculated in a similar fashion. Again the integral is divided into three parts.

$$P(\bar{\varepsilon}, \kappa) = b \int_{-t/2}^{t/2} \sigma_x(y) dy \quad (2.74)$$

$$= b \left(\int_{-t/2}^{\zeta^\ominus} \text{sign}(\varepsilon_x(y)) \sigma_{ys} (1 + \alpha(|\varepsilon_x(y)| - \varepsilon_{ys}))^m dy \right. \\ \left. + \int_{\zeta^\ominus}^{\zeta^\oplus} E \varepsilon_x(y) dy \right. \\ \left. + \int_{\zeta^\oplus}^{t/2} \text{sign}(\varepsilon_x(y)) \sigma_{ys} (1 + \alpha(|\varepsilon_x(y)| - \varepsilon_{ys}))^m dy \right), \quad (2.75)$$

which becomes

$$P(\bar{\varepsilon}, \kappa) = -b \left(\frac{(1 + \alpha(|\bar{\varepsilon} + \kappa \frac{t}{2}| - \varepsilon_{ys}))^{m+1} - (1 + \alpha(|\bar{\varepsilon} - \kappa \zeta^\ominus| - \varepsilon_{ys}))^{m+1}}{(1+m)\alpha\kappa} \right. \\ \left. + E \left(\frac{\kappa}{2} (\zeta^{\ominus 2} - \zeta^{\oplus 2}) + \bar{\varepsilon} (\zeta^\oplus - \zeta^\ominus) \right) \right. \\ \left. + \frac{(1 + \alpha(|\bar{\varepsilon} - \kappa \frac{t}{2}| - \varepsilon_{ys}))^{m+1} - (1 + \alpha(|\bar{\varepsilon} - \kappa \zeta^\oplus| - \varepsilon_{ys}))^{m+1}}{(1+m)\alpha\kappa} \right). \quad (2.76)$$

The moment and force relations (resp. relation (2.73) and (2.76)) hold for linear and power law hardening. For power law hardening the factor α is unchanged, while for linear hardening $\alpha = H/\sigma_{ys}$ and $m = 1$.

However, these equations cannot be directly employed for a perfect plastic material. For uniaxial loading $\kappa = 0$, while κ appears either in equation (2.77) and equation (2.78) in the denominator. For this case the force and moment are analysed separately. This results in

$$M(\bar{\varepsilon}, \kappa) = b \frac{\sigma_{ys}}{2} \left(\text{sign}(\bar{\varepsilon} + \kappa \frac{t}{2}) (\frac{t^2}{4} - \zeta^{\ominus 2}) + \text{sign}(\bar{\varepsilon} - \kappa \frac{t}{2}) (\zeta^{\oplus 2} - \frac{t^2}{4}) \right) + \frac{2b}{3} E \kappa (\zeta^{\oplus 3} - \zeta^{\ominus 3}) \quad (2.77)$$

for the moment and in

$$P(\bar{\varepsilon}, \kappa) = -b \sigma_{ys} \left(\text{sign}(\bar{\varepsilon} + \kappa \frac{t}{2}) (\zeta^\ominus + \frac{t}{2}) + \text{sign}(\bar{\varepsilon} - \kappa \frac{t}{2}) (\zeta^\oplus - \frac{t}{2}) \right) + \frac{b}{2} E \kappa (\zeta^{\oplus 2} - \zeta^{\ominus 2}) \quad (2.78)$$

for the force.

3

Program architecture

The simulation can be divided into three stages. The first stage is the network generation. A matlab algorithm is used to generate Voronoi tessellations prior to the actual simulation, which will be the second stage. This stage consists out of a FORTRAN program calculating the strains, stresses and displacements in the network for a given applied strain. The third stage is a postprocessing program, also done in FORTRAN, which generates a strain map based on the displacements output by the simulation in the second stage.

3.1 Voronoi tessellations

Voronoi networks are used as input for the simulations. The generation of random distribution of the Voronoi cells involves similar physics as the foaming process, where bubbles nucleate at random points forming the foam. The growth process of an isotropic structure is similar to a Voronoi tessellations based on a set of random points (nuclei) under the following assumptions.[9]

1. All nuclei appear simultaneously.
2. All nuclei remain fixed in location throughout the growth process.
3. For each nucleus the growth occurs at the same rate in all directions.
4. The linear growth rate is the same for each cell associated with a nucleus.
5. Growth ceases for each cell whenever and wherever it comes into contact with a neighbouring cell.

It is clear the process of forming a foam is more complex, however, the structure of many foams is in close agreement with Voronoi tessellations under previous stated assumptions [1].

3.1.1 Network generation

Cell size distribution

The network generation starts with generations of random points (seeds) in a rectangle with area A_0 . After the first seed has been generated the subsequent seeds will be accepted only if the distance to any existing seeds is greater than a minimum allowable distance δ . This proces will continue until the the rectangle is filled with n seeds. Through the δ parameter the size distribution of the cells can be controlled.

Randomness

To classify the randomness of the structure the minimum allowable distance between the seeds is normalized by

$$d_0 = \sqrt{\frac{2A_0}{\sqrt{3}n}}. \tag{3.1}$$

Now we can define a parameter α to quantize the randomness: $\alpha = \delta/d_0$. For a regular honeycomb $\alpha = 1$ and for a completely random Voronoi tessellation $\alpha = 0$.

The set of points after this procedure is used to create the Voronoi tessellations. Now, Delaunay triangulation is done, meaning that adjacent seeds are connected to each other by straight lines. After this Voronoi polygons are created by truncating the perpendicular bisectors (for the created

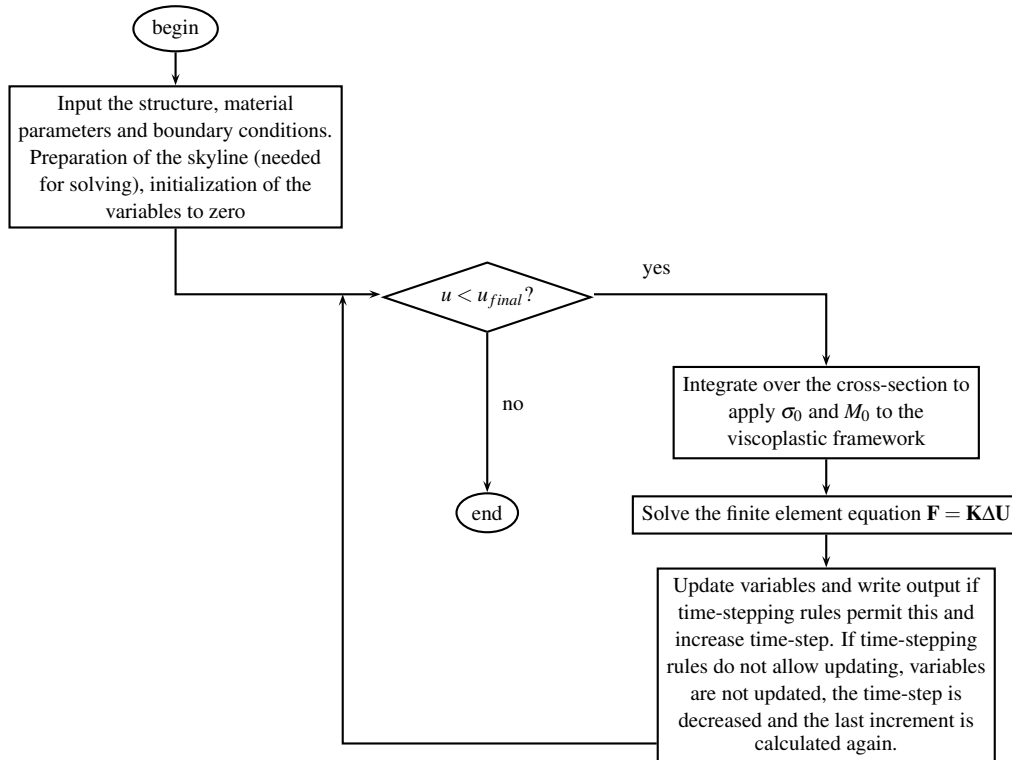


Figure 3.1: A flowchart of the FORTRAN program.

lines) at their interscction points. After the tessellation is done another Delaunay triangulation is performed which is used later on for the strain mapping.

All of this is done with the commercial software Matlab, which already has built-in routines for Delaunay triangulation and Voronoi tessellation generation.

3.2 FORTRAN code

The finite element framework is calculated with the use of a FORTRAN program. Because of the high level of complexity and the large amount of lines of code in the program, only the basic outline of the program will be discussed here.

The program is an extension of an existing finite element framework code. Figure 3.1 shows a simplified flowchart of the program. For this thesis the majority of the modifications were made in the most right top box, where the hardening properties of the material come into the picture. Of course we also deal with the first box, where the material parameters, input structure and boundary conditions are set. For different kinds of input structures time-stepping needs to be adjusted accordingly, which takes place in the bottom right function box. In this box the output is also written which is important for analysis and postprocessing.

3.3 Strain mapping

Strain mapping is a postprocessing procedure to visualize the strain in a foam for detailed analysis. The method is based on [5] pp. 62. It was originally designed for small deformation i.e. elastic deformation, but since our simulation deals with large deformations we should work with accumulation of incremental strains instead of total strains.

A simulation performed on a foam outputs incremental displacements for each node at every timestep. Using these incremental displacements (Δu_i^j) the strain in each triangle can be calculated. This results in the following incremantal strains

$$\begin{bmatrix} \Delta \varepsilon_{11} \\ \Delta \varepsilon_{22} \\ \Delta \varepsilon_{12} \end{bmatrix} = \begin{bmatrix} N_1^p & 0 & N_1^r & 0 & N_1^q & 0 \\ 0 & N_2^p & 0 & N_2^r & 0 & N_2^q \\ N_1^p/2 & N_1^p/2 & N_2^p/2 & N_1^r/2 & N_2^q/2 & N_1^q/2 \end{bmatrix} \begin{bmatrix} \Delta u_1^p \\ \Delta u_2^p \\ \Delta u_1^r \\ \Delta u_2^r \\ \Delta u_1^q \\ \Delta u_2^q \end{bmatrix}, \quad (3.2)$$

where N_i^j ($i = 1, 2$ and $j = p, q, r$) are the shape functions. These shape functions have the following form [10]

$$\begin{aligned} N_1^p &= (y_2 - y_3)/A & N_2^p &= (x_3 - x_2)/A, \\ N_1^q &= (y_3 - y_1)/A & N_2^q &= (x_1 - x_3)/A, \\ N_1^r &= (y_1 - y_2)/A & N_2^r &= (x_2 - x_1)/A, \end{aligned} \quad (3.3)$$

where A refers to the area of the triangle and x_1 - x_3 and y_1 - y_3 refer to respectively the x -coordinates and the y -coordinates of the triangle's nodes.

Now, the strain map can be constructed in two ways: on method is by taking the average incremental strain of all the triangles surrounding a node normalized by the area of the triangles. This method

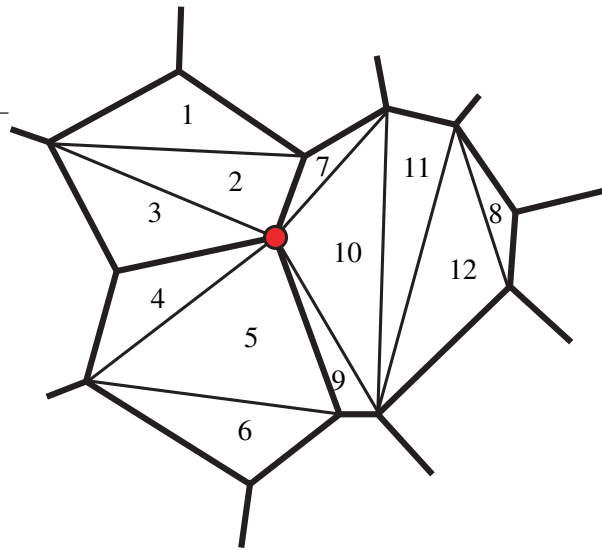
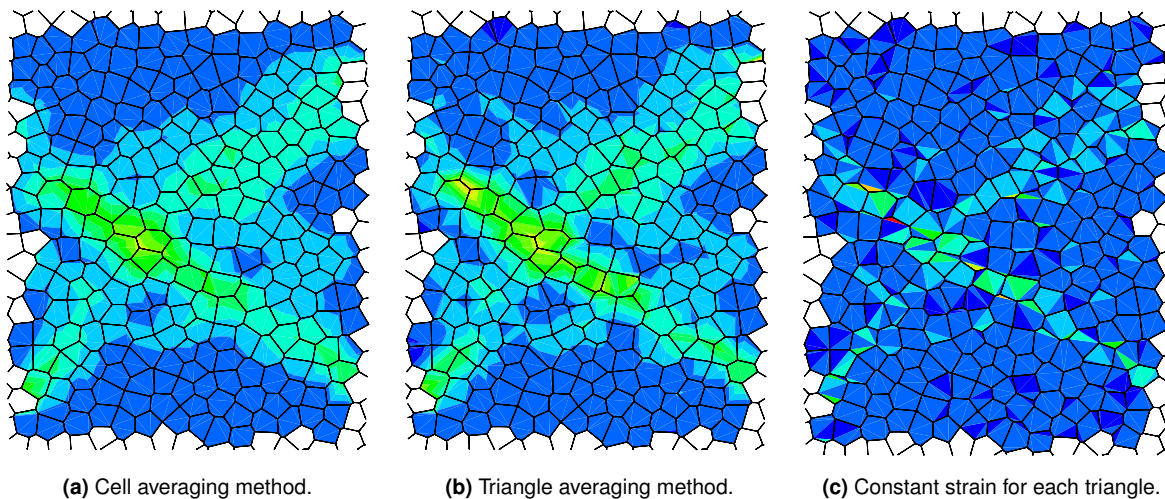


Figure 3.2: Schematic picture of a part of a 2D foam sample.

will be called the “triangle averaging” method. The other method is by taking the average incremental strain of all surrounding cells normalized by the area of these cells (the incremental strain in a cell is the average strain of its triangles normalized by the triangle’s area). This will be called the “cell averaging” method.

Please refer to figure 3.2 for the following explanation about the strain calculation methods. If one would like to calculate the incremental strain in the red node, the cell averaging method will result in

$$\Delta\varepsilon = \left(\sum_{i=1}^3 \frac{\Delta\varepsilon_i A_i}{\sum_{j=1}^3 A_j} + \sum_{i=4}^6 \frac{\Delta\varepsilon_i A_i}{\sum_{j=4}^6 A_j} + \sum_{i=7}^{12} \frac{\Delta\varepsilon_i A_i}{\sum_{j=7}^{12} A_j} \right) / \sum_{j=1}^{12} A_j, \quad (3.4)$$



(a) Cell averaging method.

(b) Triangle averaging method.

(c) Constant strain for each triangle.

Figure 3.3: The different strain map methods. Shown for a 16×20 Voronoi with fully constrained boundary conditions (please see the next chapter for an explanation of these boundary conditions). Please note that the color levels of the figures 3.3a and 3.3b correspond with each other and that the color levels in figure 3.3c are a different set.

while the triangle averaging method will result in

$$\Delta\epsilon = \frac{\sum_{i=2,3,4,5,7,9,10} \Delta\epsilon_i A_i}{\sum_{i=2,3,4,5,7,9,10} A_i}. \quad (3.5)$$

The numbers refers to the triangles in figure 3.2: $\Delta\epsilon_i$ stands for the incremental strain in triangle i and A_i is the area of triangle i .

Figure 3.3 shows the two different strain mapping methods and also a strain map with constant strain per triangle for reference.

The disadvantage of the triangle averaging method is that it depends on the way of discretization of the cells into triangles. There can be more than one triangulation of the same domain depending on the way the Delaunay triangulation is performed. This can be done per cell or over the whole structure. These two yield different results. It can be seen in figure 3.4 that the strain map can look very different if the triangle discretization in a single cell is changed. An advantage, however, is that a more detailed strain map can be constructed. A strain map in which smaller localized strains will be visible. In a strain map from the cell averaging method the strain will be more ‘smeared out’, but the strain map will not depend on the discretization of the cells. Because of this last reason a decision was made to use the strain map with the cell averaging method.

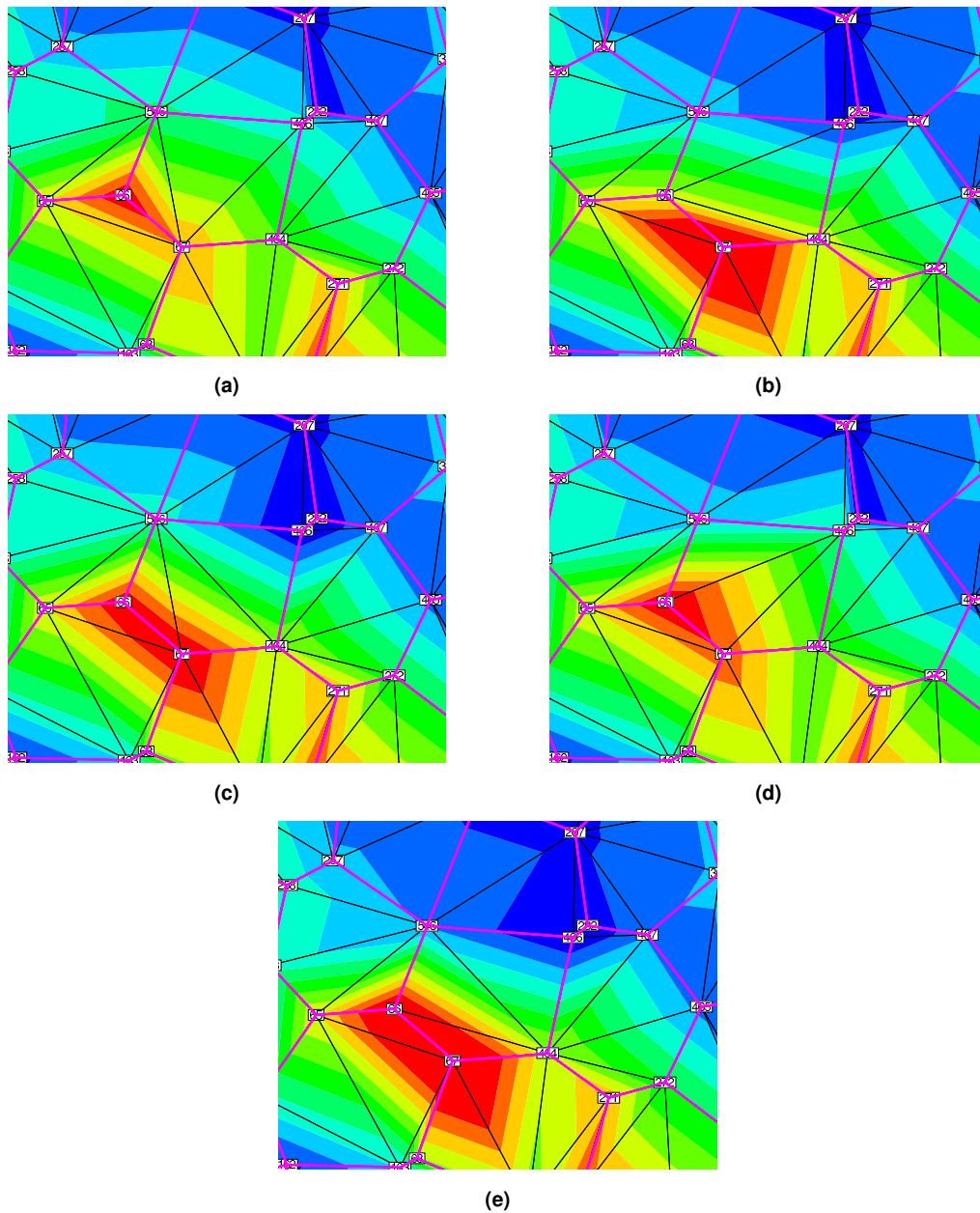


Figure 3.4: Different strain maps for different cell discretizations for the triangle averaging method. Snapshots of strain maps of a 16×20 cells Voronoi network in compression. The middle cell's discretization is changed. Even if the discretization of only one cell is changed the strain map still can look very different. Compare for example figure 3.4a to figure 3.4e.

4

Sample size effects

It is known that as the sample gets smaller, the boundary effects become more influential and as a result foam properties will be very different. Therefore it is important to use a sample size for which these effects are absent. To find out the optimal sample size of the network, which will be used as a standard size for the rest of the simulations, a number of sample sizes has been analysed in order to find a converged sample size. Convergence in Young's modulus, yield stress (tension) and peak stress (compression) is considered to get rid of the sample size effects. Finally, a comparison between tension and compression is made using strain maps.

4.1 Boundary conditions

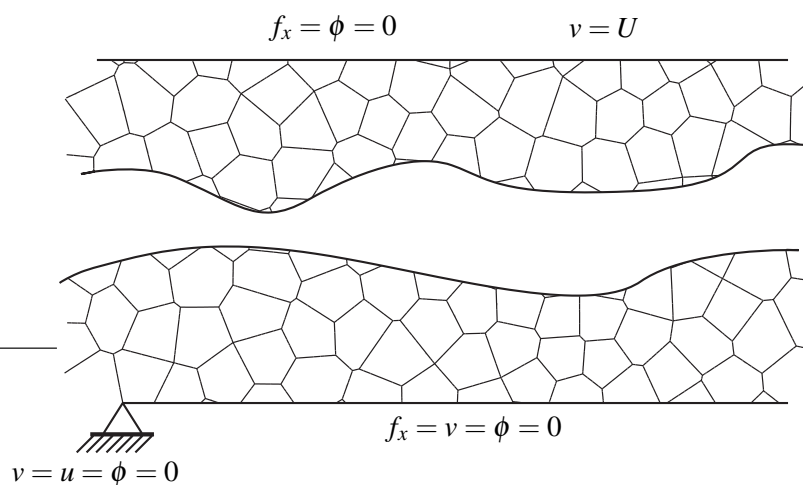


Figure 4.1: The boundary conditions chosen for the Voronoi networks.

In order to make the simulations comparable with experiments on bulk materials one needs to find the best boundary conditions for the problem at hand. The best choice in this case is shown in figure

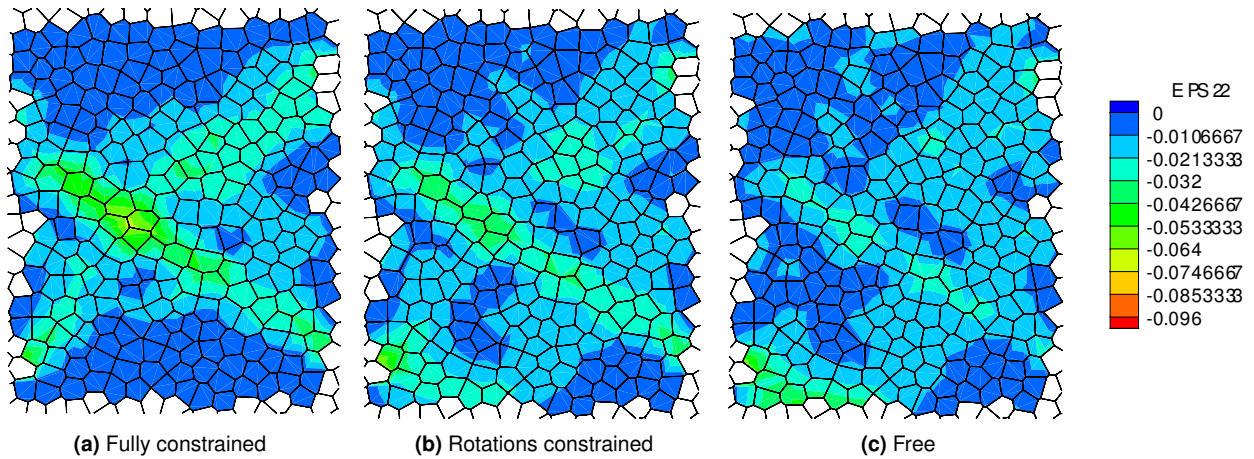


Figure 4.2: Compression strain maps for different boundary condition sets at an overall strain of $\epsilon^* = 0.014$.

4.1. Here the lower boundary nodes are constrained to move in the vertical direction and to rotate. Furthermore the most bottom left node is also constrained to move in the horizontal direction. The left and right boundary nodes are free. The top boundary nodes are constrained to rotate and free to move in the horizontal direction. To deform the structure a displacement in the vertical direction is applied to the top boundary nodes.

Why are these the chosen boundary conditions? This set of boundary conditions is the result of a study where the strain maps with different boundary conditions sets were compared. Figure 4.2 shows the strain maps for these different sets of boundary conditions. In all of the sets the most bottom left node is fully constrained. Besides the set shown in figure 4.1 (and also 4.2b) called ‘rotations constrained’ there also is a set called ‘fully constrained’ where additionally the top and bottom nodes are constrained in the horizontal direction (see figure 4.2a). The third set is called

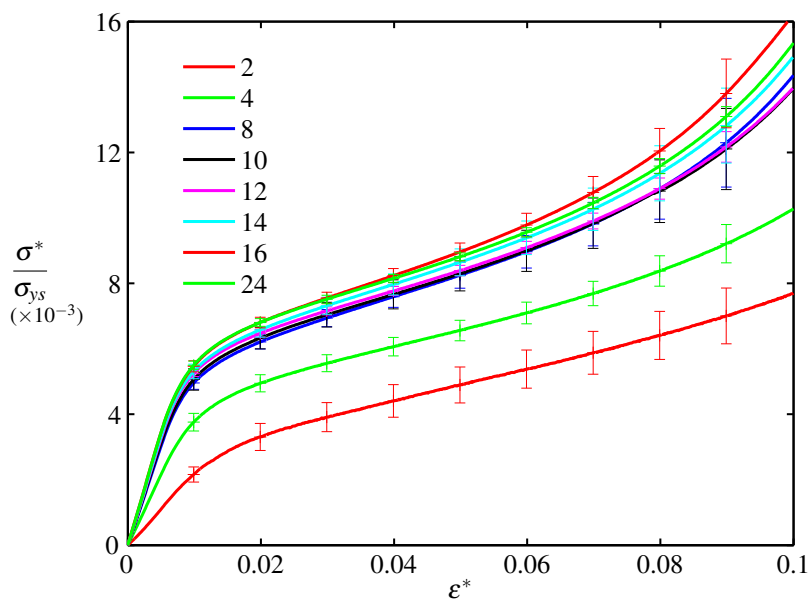


Figure 4.3: Average stress strain curves for different sample sizes in tension. The average is taken over five different random realizations with the same size. The error bars indicate the standard deviation of these five samples.

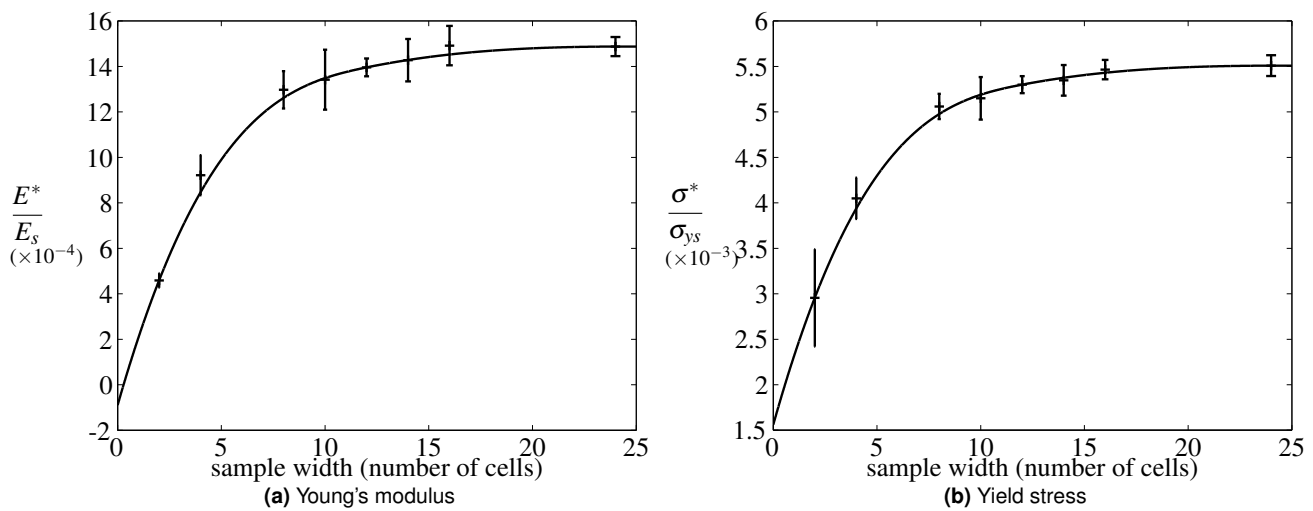


Figure 4.4: Sample size effect on Young's modulus and the yield stress in tension. Young's modulus is the slope of the $\sigma - \varepsilon$ curve over initial elastic range. The yield stress is the 0.2% offset stress.

'free'. Here, the top and bottom nodes' rotations and horizontal movement are not constrained (figure 4.2c).

The first observation which can be made from this figure is that the more constraints are added the more strain will localize. For the fully constrained case strain seems to localize in two bands. This effect gets smaller if constraints on the structure are removed. By fully constraining the top and bottom nodes we basically are excluding the top and bottom region from the simulation. It is clear that the amount of strain in these regions is almost zero. This would be a waste of computational power, because the elements in these regions still need to be accounted for in the calculation. These boundary conditions are not an option. The free and the rotation constrained set look very alike, but there is a reason why the rotation constrained set's boundary conditions are used. When rotation is not constrained in the top and bottom nodes displacement in the horizontal direction of the top and bottom can be an unrealistic large influence on the strain maps, especially in compression. For large strains struts touching the top or bottom boundary can start intersecting each other causing a huge interference in the strain map. For future prospects when fracture will be incorporated into the model constraining the rotation also will prevent these boundary struts from fracturing prematurely.

4.2 Tension

In figure 4.3 different stress strain curves in tension are plotted for different sample sizes. Only the width of the sample size is changed, varying from 2 to 24 cells. The height remains constant at 20 cells. Furthermore all other input parameters (of the solid material) including relative density of the sample, yield strength and Young's modulus are kept constant at respectively $\rho^*/\rho_s = 10\%$, $\sigma_{ys} = 150\text{MPa}$ and $E_s = 70\text{GPa}$. These simulations were performed for power law hardening, where the hardening exponent was $m_s = 0.2$. Convergence is sufficient when the sample size 16×20 cells is reached.

Young's modulus and the yield stress also are converging when sample size is increased. For each size the Young's modulus and yield stress are calculated for all the five different random realizations. Young's modulus is the slope of the stress strain curve in the initial elastic range. The yield stress is

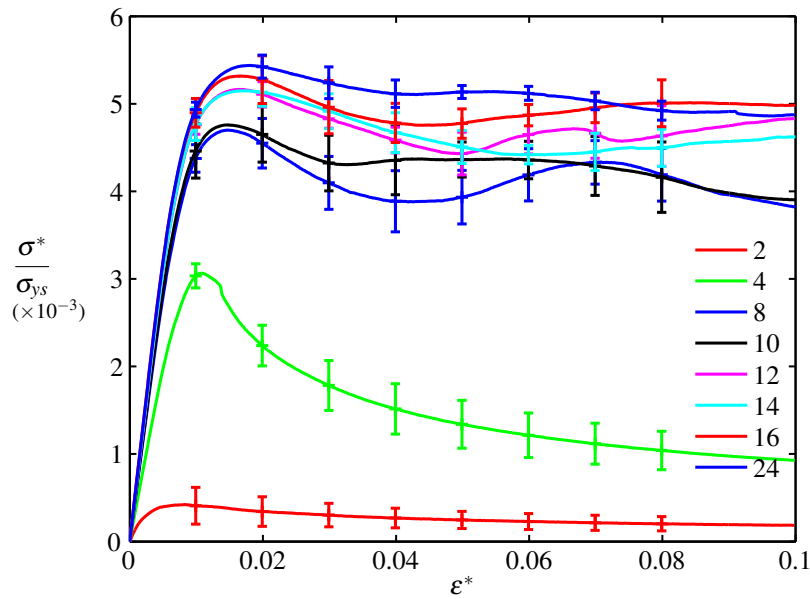


Figure 4.5: Average stress strain curves for different sample sizes in compression. The average is taken over five different random realizations with the same size. The error bars indicate the standard deviation.

defined at the intersection of the stress strain curve with a straight line of slope E intersecting at the $y = 0$ axis at $\epsilon^* = 0.002$ (this definition of yield stress is called the 0.2% offset stress). Respectively the average value and the standard deviation of these Young's moduli and yield stresses are plotted in figure 4.4a and 4.4b. For the Young's modulus as well as the yield stress one observes convergence around 16×20 cells.

4.3 Compression

Figure 4.5 shows an overview of the stress strain behaviour for different sample sizes in compression. This figure is generated in an analogous way as figure 4.3, but now for compressive boundary

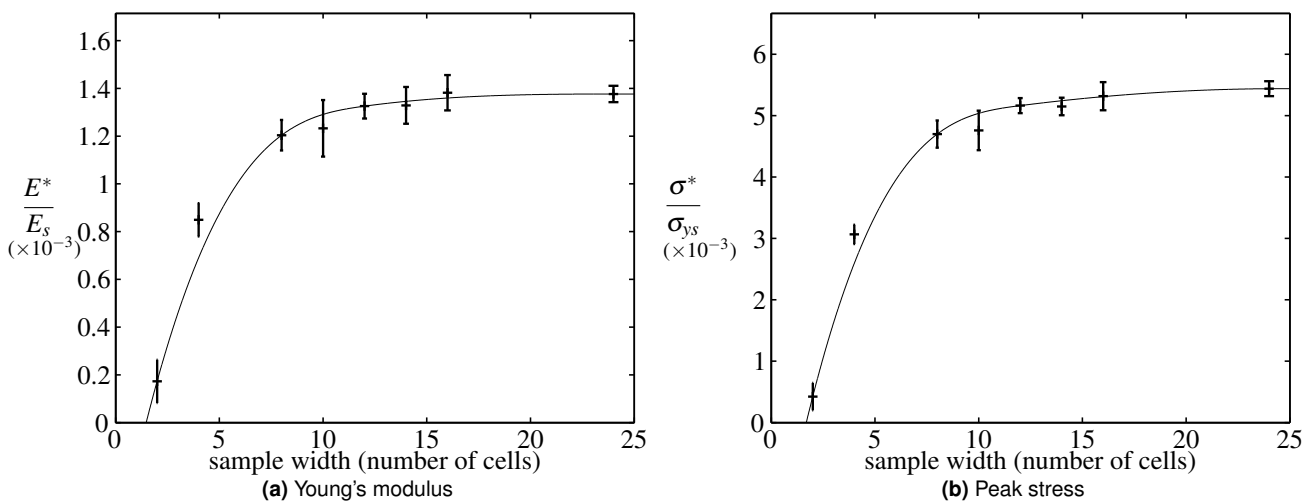


Figure 4.6: Sample size effect on Young's modulus and the peak stress in compression.

conditions. It is clear that the curves are converging, but it is not so obvious where this is happening exactly. For compression bands of collapsed cells form in the foam, resulting in hardening and softening of the stress strain curves after the peak stress. Since all of these curves are averages of different random realizations, this effect of hardening and softening is blurring our vision. Increasing the number of realizations taken for each sample size would diminish this effect. However, these results combined with the results in figure 4.6 are sufficient to choose a converged sample size.

In figure 4.6a Young's modulus of the foam is shown for different sample sizes. Young's modulus is defined in the same way as for the tension simulations. A different foam parameter - peak stress - is displayed in figure 4.6b. It is defined to be the maximum stress value of the stress strain curve of a foam sample. In figures 4.6a and 4.6b the average and standard deviation of five realization per sample size are shown. Again we decide that the converged sample size is 16×20 cells.

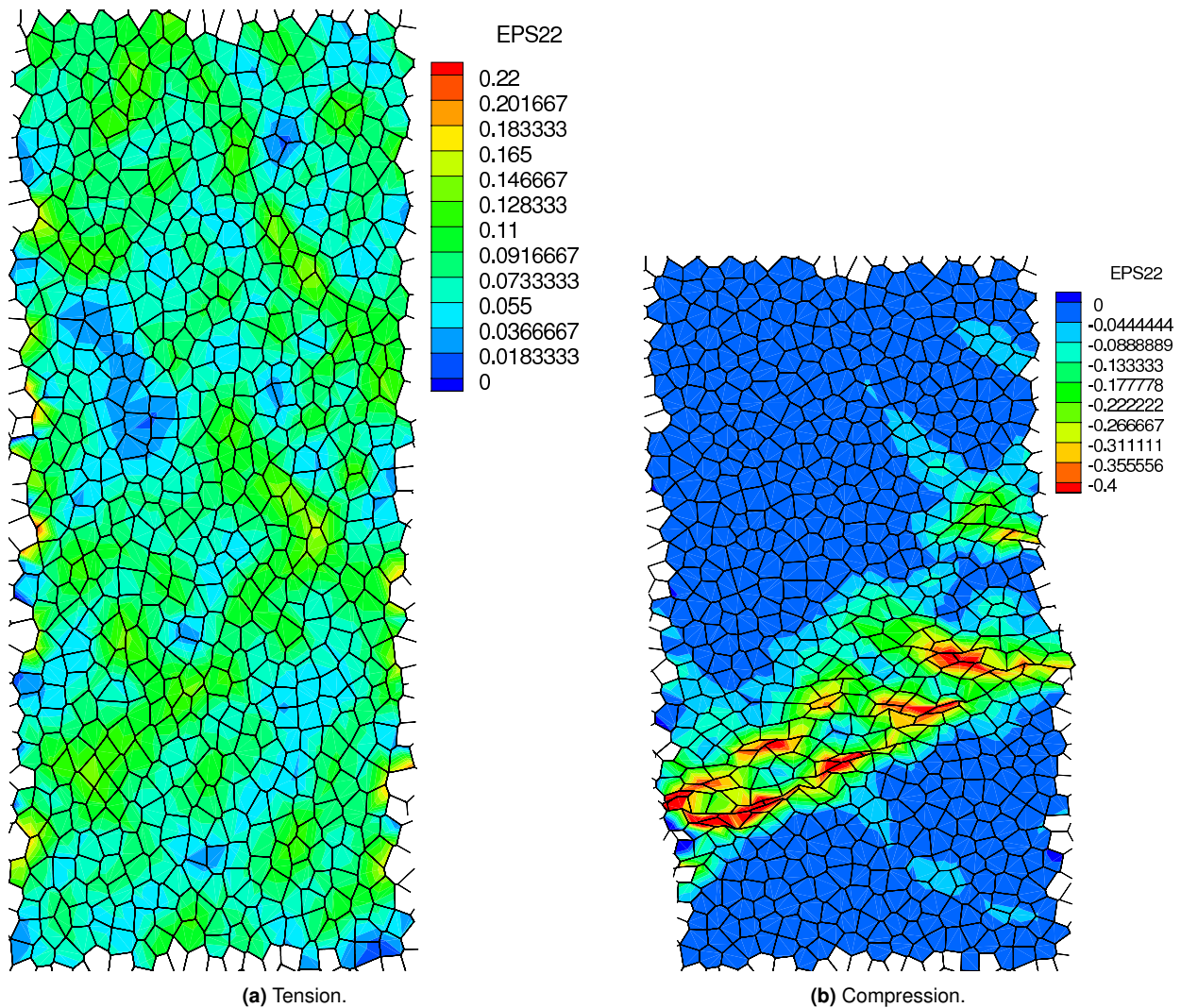


Figure 4.7: Strain maps for tension and compression on a 40×20 Voronoi network.

4.4 Strain maps: compression and tension

In figure 4.7a and 4.7b one will find strain maps in tension and compression respectively for a 40×20 Voronoi at a strain of $\varepsilon^* = 0.077$. A clear difference between tension and compression is the localization of strain. In tension the strain map looks homogeneous, whereas the strain map for compression shows a clear localization of strain in two bands formed in the middle. In tension the struts will try to align making the foam stiffen and spreading the strain throughout the network. In compression, on the contrary, the deformation will localize in the weakest regions of the foam. Once a cell starts to collapse in one of these weak regions it will also affect its neighbouring cells, starting the formation of a band of collapsed cells. In experiments one will observe the same effect, however there bands most often occur at 90° to the loading direction, while in the 2D simulations only inclined bands at 60° to the loading direction were observed [12],[8].

5

Hardening effects

Strain hardening of the foam material plays a significant role after the foam has started to yield. It also has a very important influence on the onset of failure. In this chapter we start with simple linear hardening, where the solid material of the foam has a bilinear stress strain curve. The relationships between the yield strength, Young's modulus and the plastic modulus of the solid material and the foam will be investigated. After this we proceed with power law hardening, a more realistic model, for which the same relations are studied as a function of the relative density of the foam. Finally, the hardening exponent's influence on strain maps is studied followed by a short section on the non-uniform cross-section.

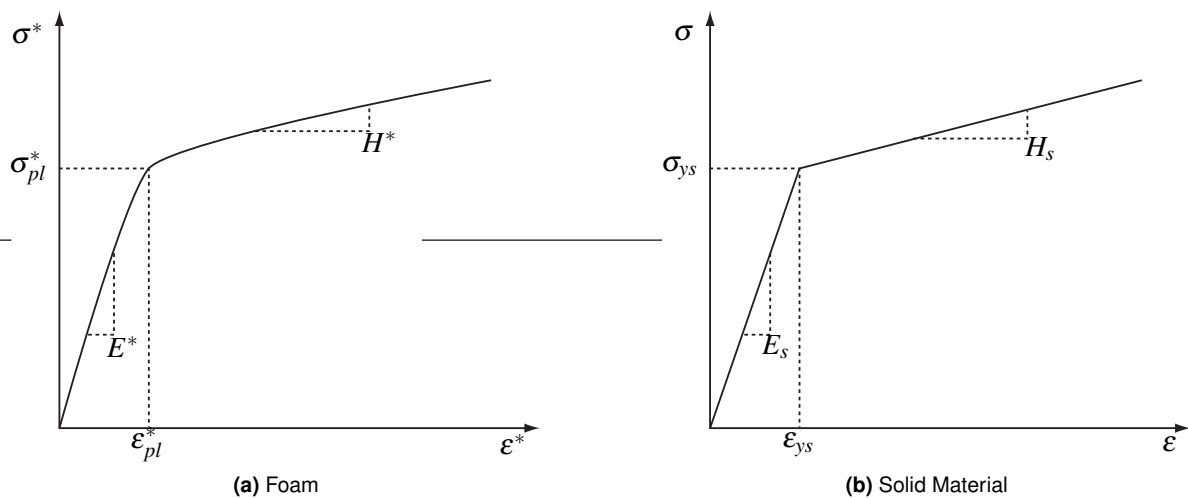


Figure 5.1: Bilinear response of the foam and the solid material.

5.1 Linear hardening

As stated before, a material which hardens linearly exhibits a bilinear stress strain curve, as shown in figure 5.1b. The material behaviour will take the form $\sigma_0 = \text{sign}(\epsilon)(\sigma_{ys} + H_s|\epsilon^p|)$, where $\sigma_{ys} = 150\text{MPa}$ and $H_s = 5\text{GPa}$ are used in the simulations presented here. Analytical expressions for relationships between the foam and the solid material for Young's modulus and the plastic collapse strength for regular hexagons can be found in the literature [1]. An additional relationship for the plastic modulus is derived in this section. One has to keep in mind that - strictly speaking - these expressions are only valid for the uncoupled model, although the outcome of simulations on the unit cell does not significantly differ with the coupled model. A more detailed study of the difference between the coupled and the uncoupled and other properties are discussed in the following section.

5.1.1 Deformation of a strut in an hexagonal unit cell

A simplification of a regular hexagonal honeycomb structure is the unit cell. Making use of the hexagon's symmetries the honeycomb structure can be greatly simplified. The unit cell only exists out of two struts, making it computationally convenient. This unit cell is used to simulate regular hexagonal structures.

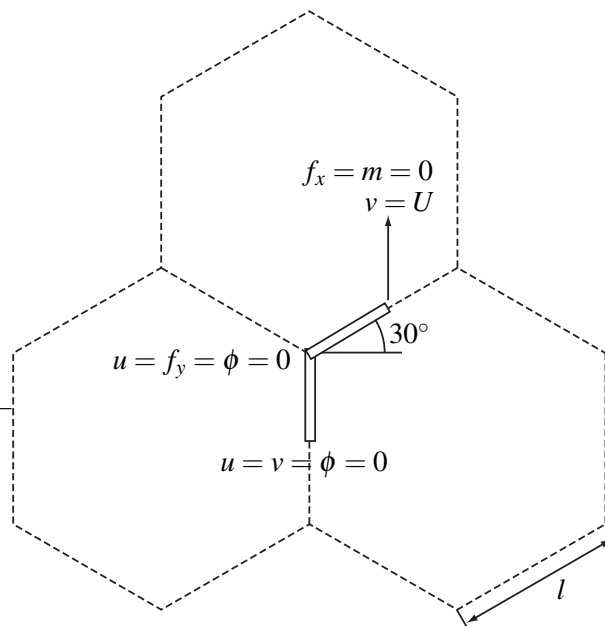


Figure 5.2: The unit cell and its (free) boundary conditions.

In figure 5.2 a schematic drawing of the unit cell can be found including the applied boundary conditions. The stress (σ^*) and the strain (ϵ^*) are calculated through $\epsilon^* = 4U/(3l)$ and $\sigma^* = 2F/(\sqrt{3}l)$. The force F is obtained from the simulation for a prescribed macroscopic displacement U . The point where the two struts of the unit cell intersect, will be called the triple point. The two struts in the unit cell actual are half of a strut in the hexagonal structure. The other half does not need to be accounted for since it is symmetrical to the first half included in the unit cell. If a reference is made to a strut in the unit cell, what is meant is the half of a strut in the regular hexagonal honeycomb structure.

The boundary conditions described in figure 5.2 are from now on called the “free” boundary conditions. The majority of the simulations are done with these boundary conditions. When it is not mentioned otherwise, the free boundary conditions are used. If also the horizontal movement in the most upper point of the unit cell is constrained ($u = 0$) we will call it the “constrained” boundary conditions. These boundary conditions are used in some of the more detailed studies.

In chapter 2 we mentioned two hardening models: the coupled and the uncoupled model. Having explained the unit cell and its possible boundary conditions we now can look at the effect of coupling.

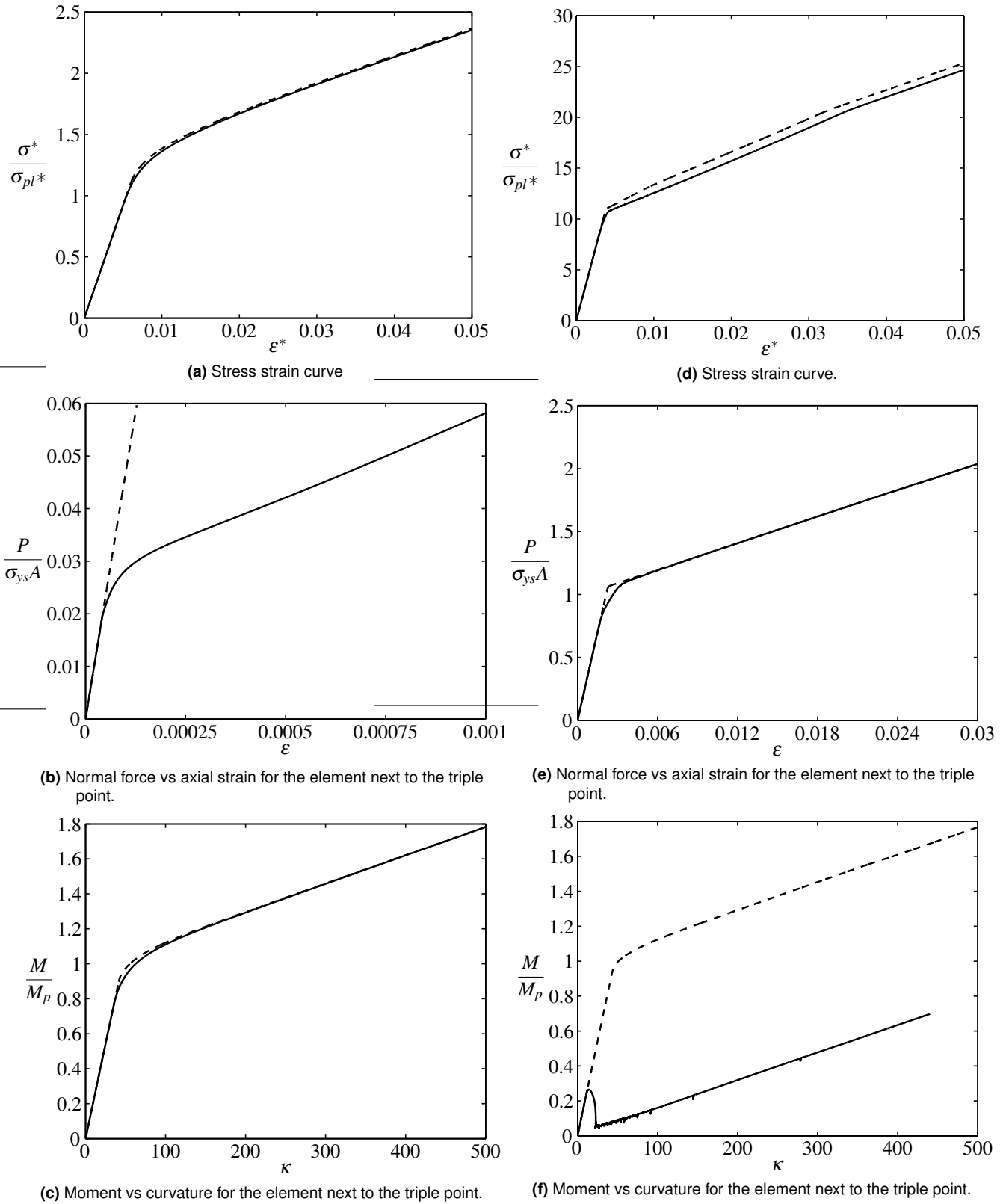


Figure 5.3: Comparison between the unit cell with the coupled model (solid lines) and with the uncoupled model (dashed lines). Linear hardening. Images 5.3a-5.3c consider the free boundary conditions, images 5.3d-5.3f consider the constrained boundary conditions. The stress strain curves are normalized with $\sigma_{pl}^* = 2/3\sigma_{ys}(\rho^*/\rho_s)^2$.

In figure 5.3 the results of the coupled and the uncoupled model for linear hardening are shown. First we focus on the case with the free boundary conditions (figures 5.3a-5.3c). The difference of the overall behaviour is small if not negligible. Note that the stress strain curves are normalized with $\sigma_{pl}^* = 2/3\sigma_{ys}(\rho^*/\rho_s)^2$, this value is used throughout the thesis to normalize stress strain curves of the unit cell and Voronoi networks. By looking at the force and moment plots of the element next to the triple point, one notices that for the uncoupled model the force remains elastic. However, the force curve of the coupled model is non-linear. This can be explained by the combined influence of the moment and force on the strain. Besides the axial strain the force is also influenced by the curvature. This curvature is rather large compared to the axial strain in a bending structure like the unit cell with free boundary conditions. Because the strains and forces in figure 5.3b are small and the moment curves in figure 5.3c are very similar the flaws of the uncoupled model barely are noticeable in the overall behaviour.

The difference of the stress strain curve for the constrained boundary conditions (figures 5.3d-5.3f) is on the other hand more significant. Now, the force curves of the coupled and uncoupled model are pretty similar and that the difference appears in the moment curve. Apparently the constrained boundary conditions are forcing the structures to be more in axial tension. The uncoupled model is unable to show the large influence of the axial straining in the moment curve. As soon as the element next to the triple point starts to yield the moment curve of the coupled model starts unloading, while the moment curve of the uncoupled model keeps on loading until it reaches M_p where it starts to yield. Since the moments and curvatures in figure 5.3e are not so small the difference in the overall behaviour is also larger.

However, in all the simulations for the scaling relationships the unit cell with the free boundary conditions is used, where the coupled and the uncoupled model are almost similar.

We also can take a closer look on how plasticity evolves throughout the upper strut in the unit cell. In figure 5.4 and figure 5.5 the stress strain curves, stress profiles for the element next to the triple point and the development of plasticity are shown respectively for the free and constrained boundary conditions. The results in these figures are with coupling.

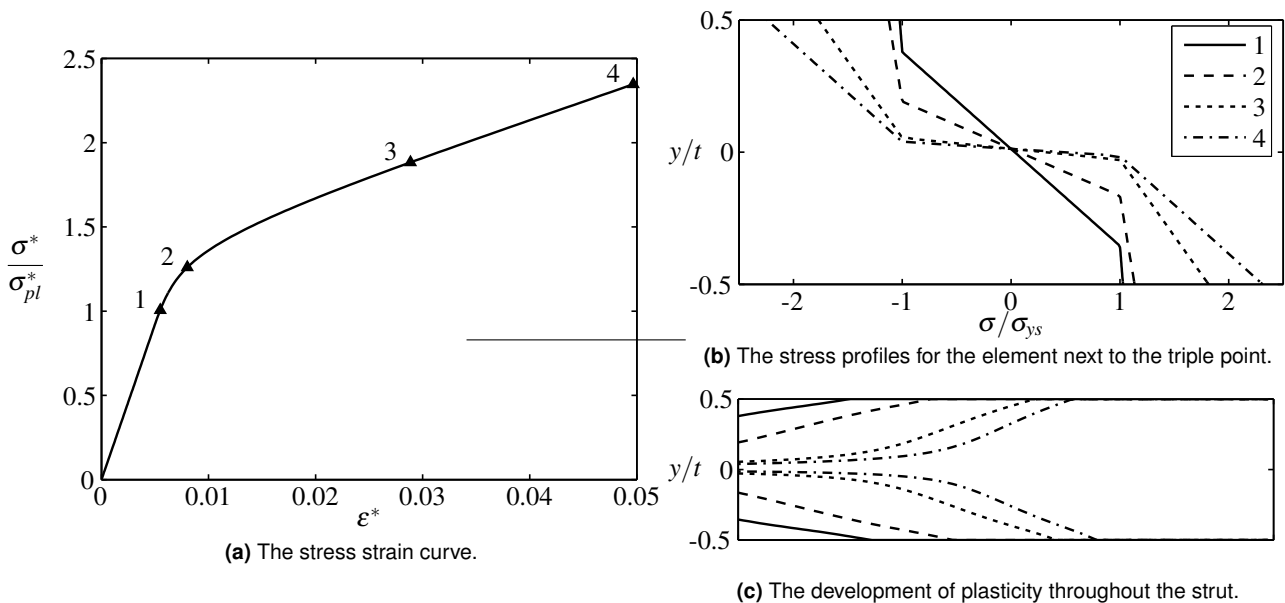


Figure 5.4: The development of plasticity in a unit cell with linear hardening and free boundary conditions.

In figure 5.4a the indicated points correspond to the numbers in figure 5.4b. The linestyles of figure 5.4b and figure 5.4c also do correspond. The lines in figure 5.4c mark the boundary between the elastic and plastic portions of the upper strut of the unit cell. The upper lines mark the boundary ζ^{\oplus} and the lower lines mark the boundary ζ^{\ominus} (the reader is referred to chapter 2 for an explanation of these boundaries).

The stress profiles are nearly symmetrical, the neutral fiber is very close to the middle of the beam element (where $y = 0$). After the initial yielding of the element next to the triple point the stress strain curve stays linear for a while, because the behaviour is stil dominated by the larger elastic core. In the beginning the plasticity evolves laterally, but after a while it spreads to the center. However, there always remains a elastic core, even for the element next to the triple point. When point 4 is reached 50%-60% of the beam elements have started yielding and 40%-50% of the volume of the strut has become plastic.

The constrained case (figure 5.5) on the other hand looks very different. The stresses are an order of magnitude higher and the beam elements are always in tension (figure 5.5c only shows the boundary ζ^{\ominus}). This is consistent with the results shown for the constrained boundary conditions for the coupling comparison. The way of loading for these boundary conditions is very much alike axial tension. Plasticity starts spreading from the bottom and quickly spreads from there to the top of the strut. At the top left of the strut a small parts remains to be elastic for a short while, but soon after that the complete strut becomes plastic. At a strain of $\epsilon^* \cong 0.035$ there is a small slope change in the stress strain curve. Because of the high stress levels the beam elements of the lower strut of the unit cell also have started yielding. All of these elements yield at the same moment and this changes the slope of the stress strain curve.

Figures 5.4c and 5.5c display for different increments in the same picture the boundary between the elastic and plastic regions. Another way to visualize the stress profiles of all the elements in the strut is showing the stress levels for one increment with a stress map. One can find these stress maps in the appendix.

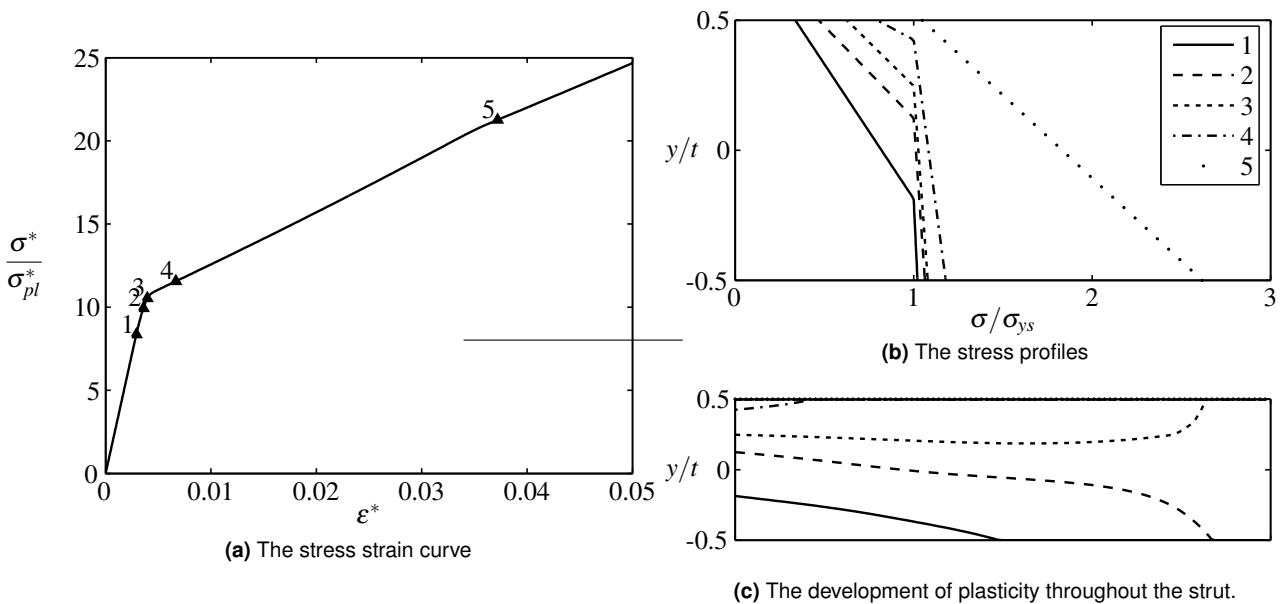


Figure 5.5: The development of plasticity in a unit cell with linear hardening and constrained boundary conditions.

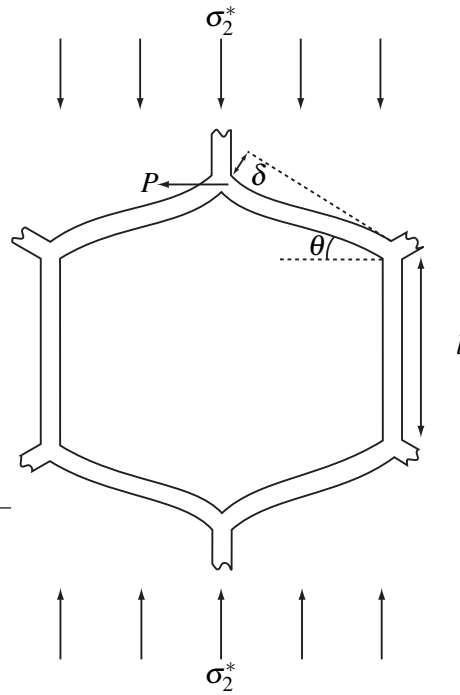


Figure 5.6: Deflection of a cell wall in a hexagonal honeycomb structure.

5.1.2 Scaling relationships for regular hexagonal honeycombs

In [1] several scaling relations between foam properties and solid material properties are derived. For example, the relationship between the plastic collapse strength of the foam ($(\sigma_{pl}^*)_1$ or $(\sigma_{pl}^*)_2$, depending on the loading direction) and the solid material (σ_{ys}) for regular hexagonal honeycombs with walls of uniform thickness is

$$\frac{(\sigma_{pl}^*)_1}{\sigma_{ys}} = \frac{(\sigma_{pl}^*)_2}{\sigma_{ys}} = C_1 \left(\frac{t}{l}\right)^2, \quad (5.1)$$

where $C_1 = 2/3$ is a constant. Another relationship for regular hexagons with walls of uniform thickness is

$$\frac{E_1^*}{E_s} = \frac{E_2^*}{E_s} = C_2 \left(\frac{t}{l}\right)^3, \quad (5.2)$$

which relates Young's modulus of the foam (E_1^* or E_2^* , depending on the loading direction) to Young's modulus of the solid material (E_s). $C_2 = 2.3$ and again is a constant.

Making use of these equations a relationship between the plastic modulus of the foam (H^*) and the solid material (H_s) is derived.

The deflection of a cell wall in a regular hexagonal honeycomb structure has an elastic and a plastic contribution:

$$\delta = \delta_{el} + \delta_{pl}. \quad (5.3)$$

A cell wall deflects elastically, according to standard beam theory, by [1]

$$\delta_{el} = \frac{Pl^3 \sin \theta}{12E_s I}, \quad (5.4)$$

where $P = \sigma_1^*(1 + \sin \theta)lb$ and $I = \frac{1}{12}bt^3$. Plastic deflection takes the form

$$\delta_{pl} = \frac{l^4 b (\sigma_1^* - \sigma_{pl}^*) (1 + \sin \theta) \sin \theta}{H_s t^3}. \quad (5.5)$$

When equation (5.5) and (5.4) are combined, equation (5.3) becomes

$$\delta = l(1 + \sin \theta) \sin \theta \frac{\sigma_1^* \eta + \sigma_1^* - \sigma_{pl}^*}{H_s} \left(\frac{l}{t}\right)^3, \quad (5.6)$$

where $\eta = H_s/E_s$. Now, ε_1^* can be calculated:

$$\varepsilon_1^* = \frac{\sin \theta}{l \cos \theta} \delta = \frac{1}{C_2} \frac{\sigma_1^* \eta + \sigma_1^* - \sigma_{pl}^*}{H_s} \left(\frac{l}{t}\right)^3. \quad (5.7)$$

Making use of equation (5.1) and (5.2) one can derive the relationship for the plastic modulus:

$$\frac{H_1^*}{H_s} = \frac{H_2^*}{H_s} = \frac{1}{H_s} \frac{\sigma_1^* - \sigma_{pl}^*}{\varepsilon_1^* - \varepsilon_{el}^*} = \frac{C_2}{1 + \eta} \left(\frac{t}{l}\right)^3. \quad (5.8)$$

Although, equation (5.7) will look different for an arbitrary angle θ , for regular honeycombs ($\theta = 30^\circ$) relationship (5.8) looks the same in the 1- and 2-direction.

Results

For relative densities from 4% up to 24% tension and compression tests for a unit cell were simulated. To investigate the impact of the geometry or finite strain effects two sets of simulations were performed. In one set of simulations the geometry has been frozen, where as in the second set the

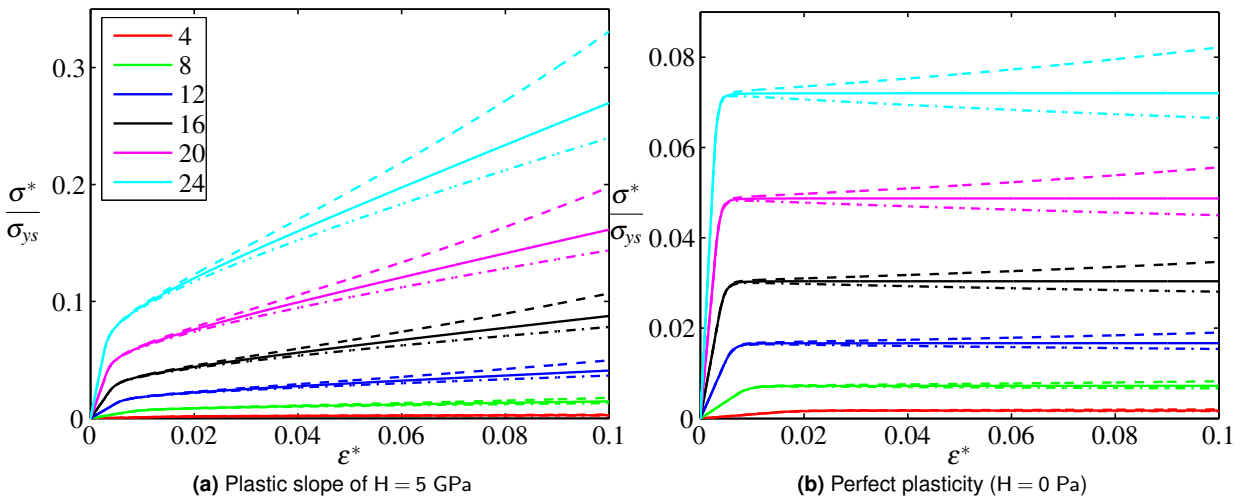


Figure 5.7: Overview of the linear hardening results for the unit cell. The different colors refer to the relative density percentages, which can be found in the legend. Furthermore, the solid lines are tension and compression curves for fixed geometry. These curves fall on top of each other and are therefore indistinguishable. The dashed lines and dash-dotted lines are respectively the tension curves and the compression curves for updated geometry.

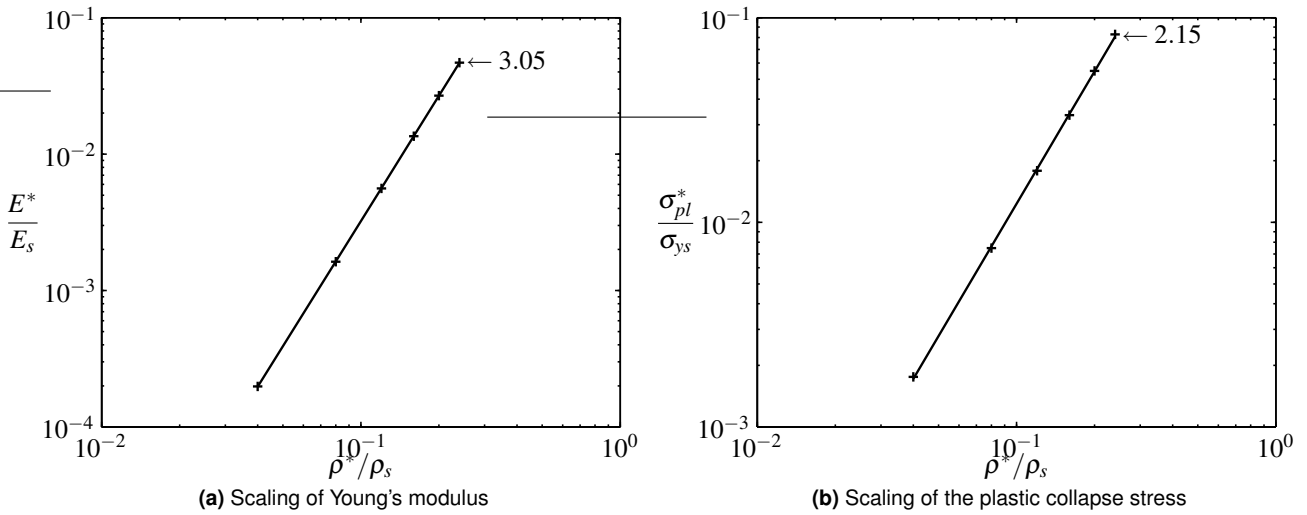


Figure 5.8: Scaling of Young's modulus and the plastic collapse strength. The numbers next to the curves in these figures indicate the power of the function and correspond to the powers in relations (5.1) and (5.2). Only the results for the tension simulations with updated geometry are presented here, since the fixed geometry results and the compression results for an updated geometry produce nearly the same curves and powers.

geometry has been updated. From now on the set of calculations with frozen geometry will be referred to as “fixed geometry” simulations and those with finite strain effects included will be called “updated geometry” simulations. The curves can be found in figure 5.7a.

In figure 5.7b one can find similar results as in figure 5.7a, but now the plastic modulus of the solid material is set to $H_s = 0$ Pa. This figure only represents change in the plastic slope due to geometry hardening. The material hardening is ruled out. This data will be used later on.

First we check if our model complies with the scaling relationships for Young's modulus and the plastic collapse strength, respectively equation (5.1) and (5.2). These foam parameters are extracted

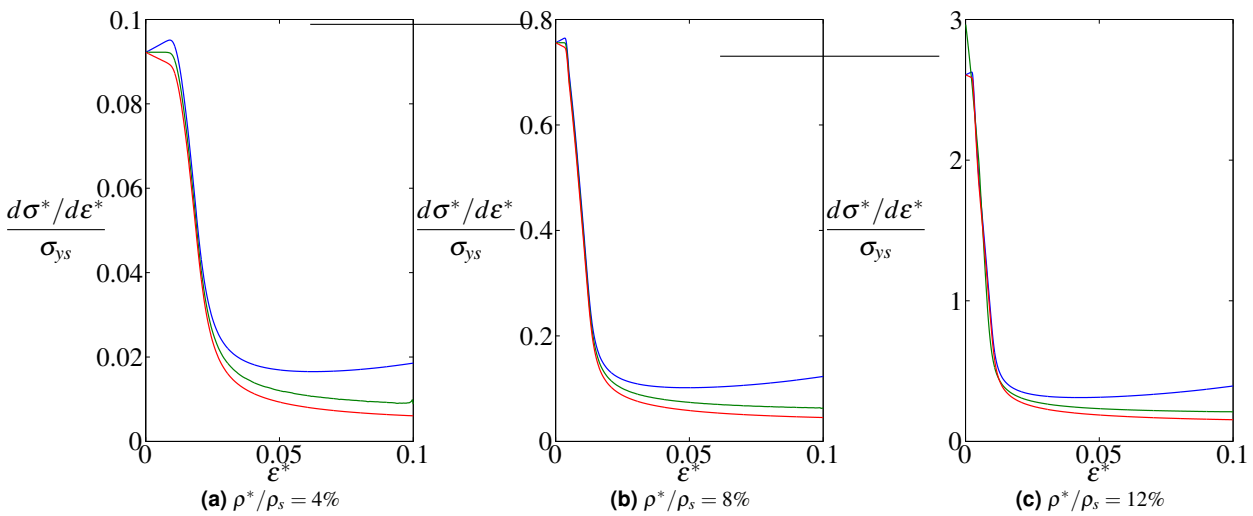


Figure 5.9: Change in slope of the stress strain curves for relative densities 4%-12%. The blue lines are for updated geometry in tension, the green lines are for fixed geometry in tension and the red lines are for updated geometry in compression.

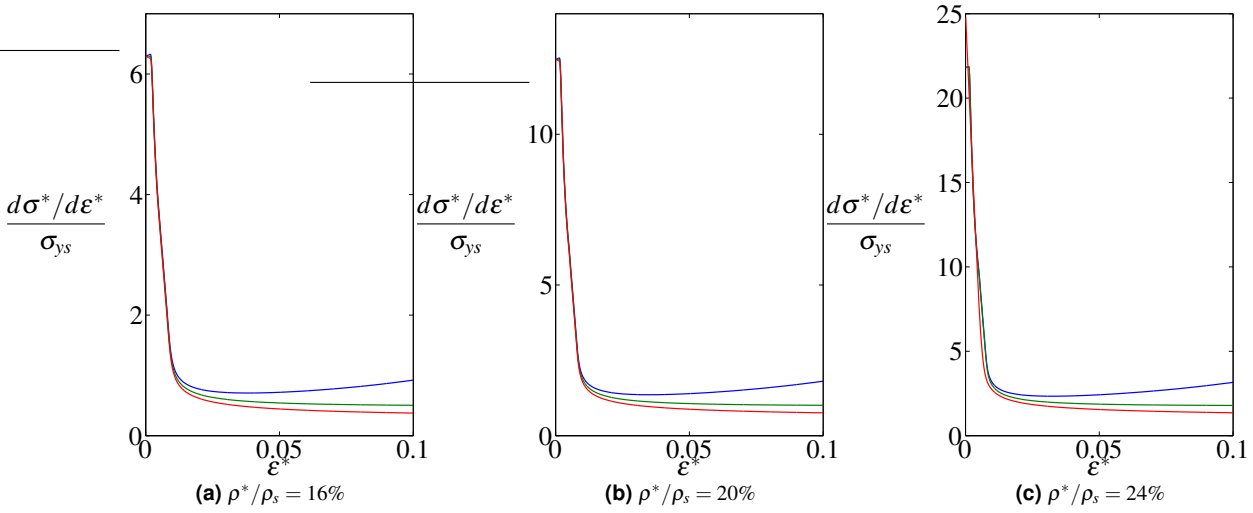


Figure 5.10: Change in slope of the stress strain curves for relative densities 16%-24%. The line colors are similar as in figure 5.9.

from the data in figure 5.7a. The yield stress is the 0.2% offset stress and the Young's modulus is the slope of the initial elastic range. We check if the powers of our simulations correspond to the powers in the previously mentioned theoretical relationships. The powers plotted next to the curves in figure 5.8a and 5.8b agree with the powers of the theoretical relationships. We also can look at the constants C_1 and C_2 respectively in equations (5.1) and (5.2). It turns out that for the simulations $C_1 = 1.17$ and $C_2 = 2.78$, where theory states that $C_1 = 2/3$ and $C_2 = 4/\sqrt{3}(= 2.3)$. Although there is an error the values still agree roughly with theory.

In order to check if the relationship in equation (5.8) agrees with the simulations, the power of this equation is compared to the theoretical value. To determine the value of the plastic modulus H^* the slopes in figure 5.7a are calculated. One can find these in figure 5.9 and 5.10. Normally these curves

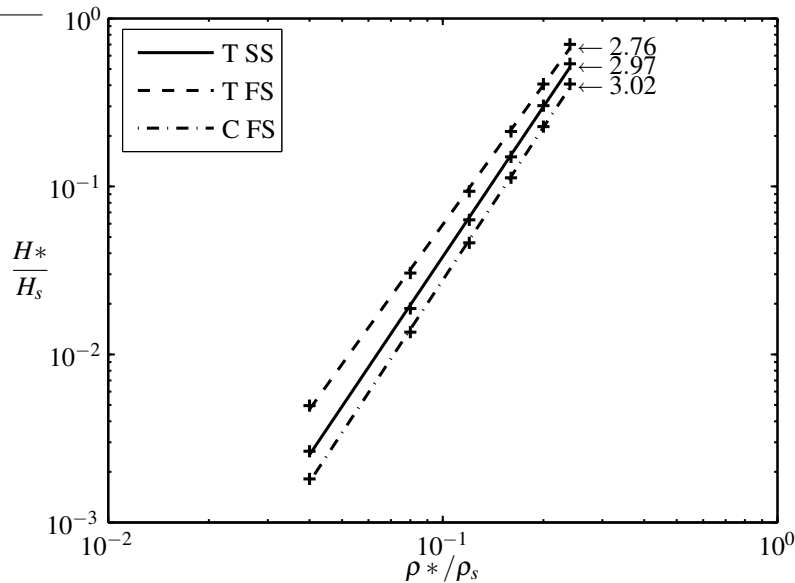


Figure 5.11: Scaling of H^* for the unit cell. The solid line represents tension (and compression which appears to be the same) for fixed geometry, the dashed line represents tension for updated geometry and the dashed-dotted line represents compression for updated geometry.

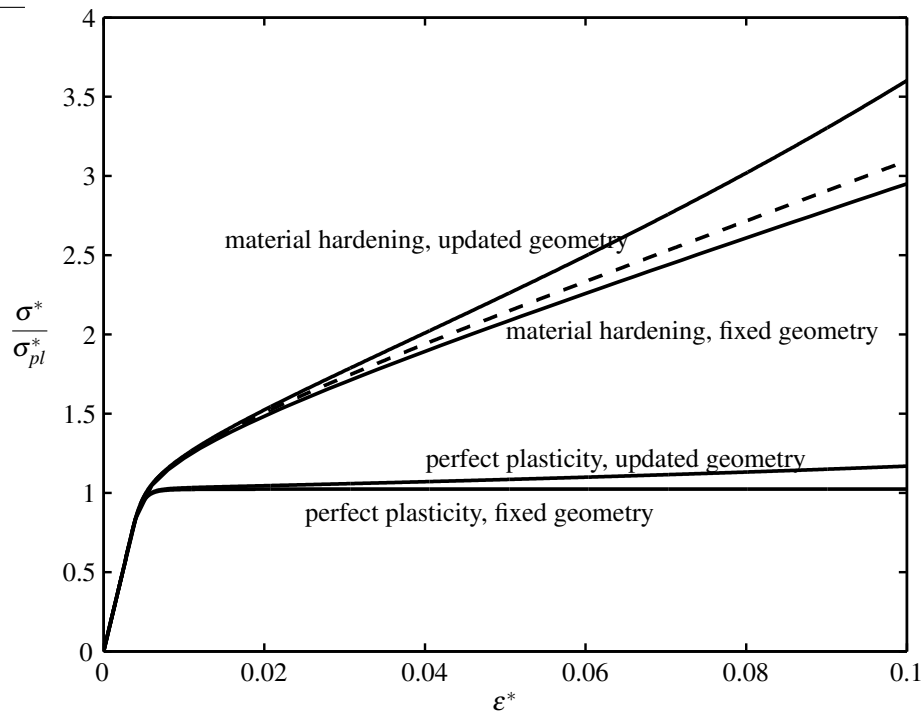


Figure 5.12: Reconstruction of the stress strain curve of the unit cell for linear hardening. This plot only shows a relative density of 16%. All the solid lines are the results of simulations in tension. A description of the simulation is stated next to each curve. The dashed line is an attempt to reconstruct the updated geometry curve with material hardening. There is a clear difference between the reconstructed and the actual curve.

would look really rough, because the stress strain curves never are completely smooth. Therefore, a smoothening algorithm is used to get rid of this roughness. Ultimately, to obtain the plastic modulus H^* , the minimum value of the slope curve is taken.

Now that we have the slope curves we can determine the plastic moduli for the different densities and conditions and see if their power matches the power in relation (5.8). The plastic moduli which were found are plotted on a double logarithmic scale in figure 5.11. The powers of the curves are indicated next to each curve.

What one would expect in figure 5.11 is that the tension curve for updated geometry scales according to the scaling relation in equation (5.8) so that all the curves scale with a power of three. This turns out not to be the case for the tension test with updated geometry. The two other curves seem to agree with the expected power. Now the question arises what could be the reason for this difference? To be able to answer this question the difference between the dashed and the solid curves in figure 5.7a needs to be understood. For this we go back to figure 5.7b where the plastic modulus of the solid material is set to zero. In other words, the material hardening is ruled out in this picture. The only difference between the dashed lines (updated geometry) and the solid lines (fixed geometry) is the influence of geometry. The difference between the solid lines (for the same colour) in figure 5.7a and 5.7b will be called the difference due to material hardening.

An attempt is made to reconstruct the actual updated geometry curves with material hardening, building it up from material hardening and geometrical hardening. This is done for one relative density in tension in figure 5.12. The solid lines in this figure represent actual simulation results, only the dashed line is a reconstructed curve. This reconstructed curve is the accumulation of

three parts: The curve for fixed geometry and perfect plasticity (for simplicity reasons this will be called the base curve), the difference between the curve for updated geometry combined with perfect plasticity and the base curves (geometrical hardening) and the difference between the curve for fixed geometry combined with material hardening and the base curve (material hardening).

If material hardening and geometrical hardening were independent effects the reconstructed curve should fall on top of the curve for updated geometry combined with material hardening. This, however, is not the case. There is still a significant gap between the reconstructed curve and the actual curve. Apparently, if these two kinds of hardening are combined they will make each other stronger, in other words there is a synergy between geometrical and material hardening.

The same effect is observed for the compression tests. Only here the difference between the reconstructed curve and actual curve is negative. This difference is smaller than the difference for the tension simulations. This can explain the larger differences for tension in the power for the scaling relationship H^*/H_s than compression. See figure 5.13 for reconstructed curve in compression.

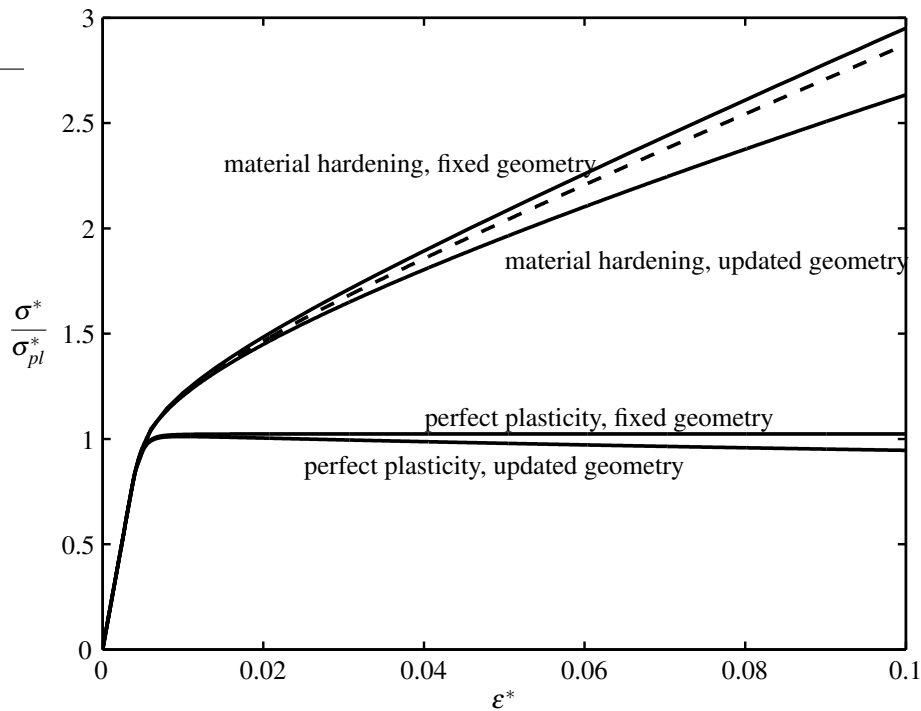


Figure 5.13: Reconstruction of the stress strain curve of the unit cell for linear hardening in compression. The linestyles and density are analogous to figure 5.12.

5.1.3 Scaling relationships for converged Voronoi networks

The same relationships from the previous section will be discussed for a converged Voronoi network. In chapter 4 we concluded that the 16×20 cells Voronoi network has reached convergence, so this sample size is used for the simulations. The applied boundary conditions for voronoi networks also were discussed in this chapter and are chosen accordingly.

In figure 5.14 the stress strain curves are plotted for a converged Voronoi network. The tension curves for updated geometry and for fixed geometry are comparable to their corresponding curves in figure 5.7a. However, as a result of the formation of bands of collapsed cells the compression curve's slope for updated geometry goes to zero and even becomes negative. It is not appropriate to consider hardening relations with interfering behaviour like this. Therefore, the analysis of the plastic modulus for the compression curves in updated geometry for Voronoi networks is omitted.

The foam to material relationships for Young's modulus and the plastic collapse strength are checked. The log-log plots showing the power of the curves varying relative density are shown in figure 5.15a and 5.15b. The power of the collapse strength agrees with the theoretical expected value of two for regular hexagons. This does not hold for Young's modulus, where one would expect a power of 3. The actual power is somewhat lower, namely 2.87. Although, a converged Voronoi sample is used there still is an error in Young's modulus and the plastic collapse stress as illustrated in figure 4.4a and 4.4b. Simulations on more different realizations are needed to prove this.

Also now the scaling relationship of the plastic modulus is studied. The same methods used for the unit cell to obtain the modulus are used for the foam. H^* is the minimum of the differentiated stress strain curves with respect to strain. The result can be seen in figure 5.16. Please note that now also the power of the fixed geometry simulations differs significantly from the theoretical expected value. As mentioned before there is an error in the results of the Voronoi networks, which might be the cause for this.

As was observed for unit cell it also seems to be the case for the Voronoi network that the plastic

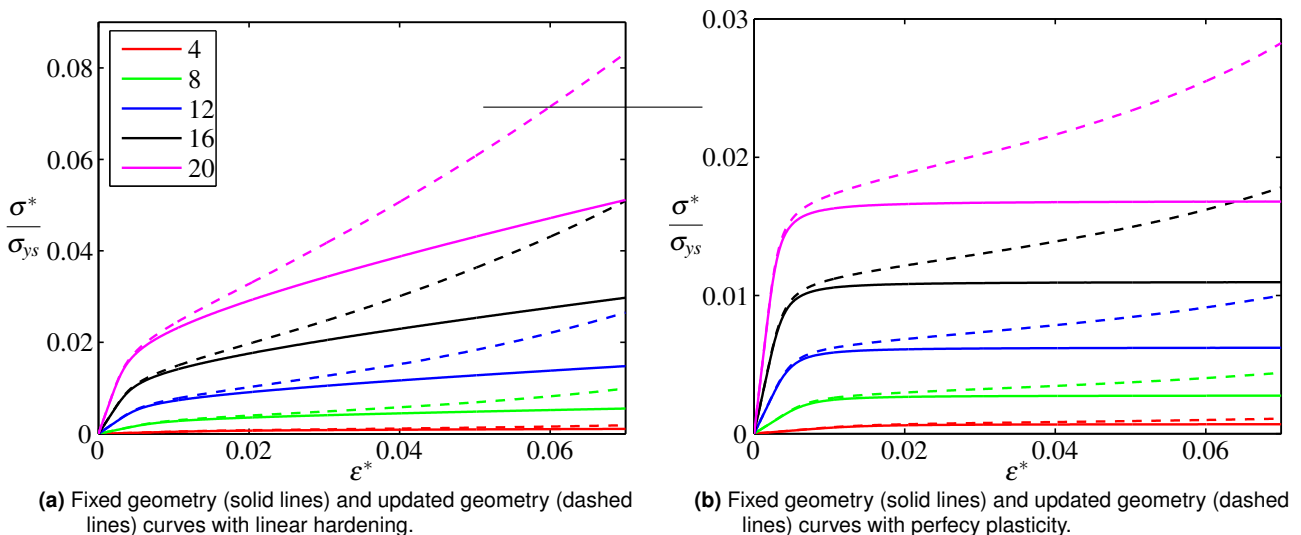


Figure 5.14: Stress strain curves of a 16×20 Voronoi network in tension with bilinear solid material input curves. The solid lines represent the simulation results for fixed geometry. Here, the compression and the tension curve fall on top of each other and are therefore indistinguishable. The dashed line is for updated geometry in tension. The different colors refer to relative density (in percentages), which is found in the legend.

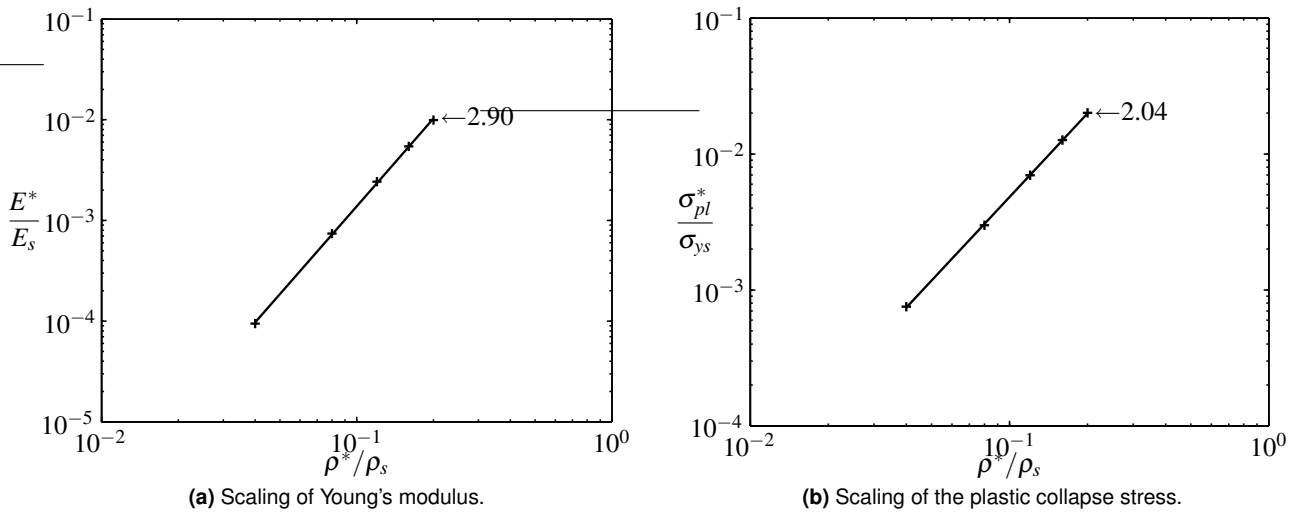


Figure 5.15: Scaling of Young's modulus and the plastic collapse strength. The numbers next to the curves in these figures indicate the power of the function and correspond to the powers in relations (5.1) and (5.2). Only the results for the tension simulations with updated geometry are shown here, since the fixed geometry results and the compression results for updated geometry produce nearly the same curves and powers.

modulus differs from the theoretical expected value. A similar reconstruction as in figure 5.12 is performed and its results are shown in figure 5.17. The relative differences in this figure are larger, but apart from that it looks quite similar to the reconstruction curves for the regular hexagons. Especially the influence of geometrical hardening seems much larger. This is easily understood since now is being dealt with a much more geometry dominated structure where there are practically no symmetries. This greater influence combined with the error on the stress strain curves due to the random nature of voronoi networks might be an explanation for the unexpected values of

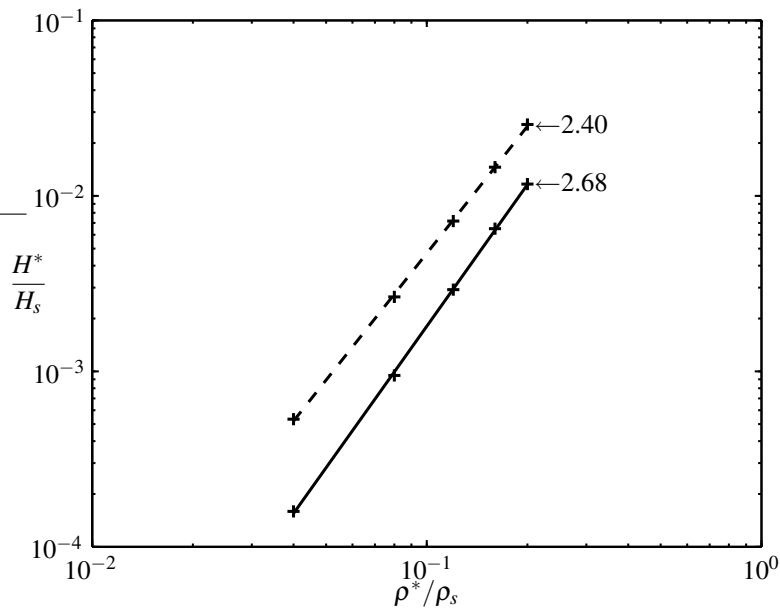


Figure 5.16: Scaling of the plastic modulus for a Voronoi network. The solid line represents tension/compression for fixed geometry, the dashed line represents updated geometry in tension.

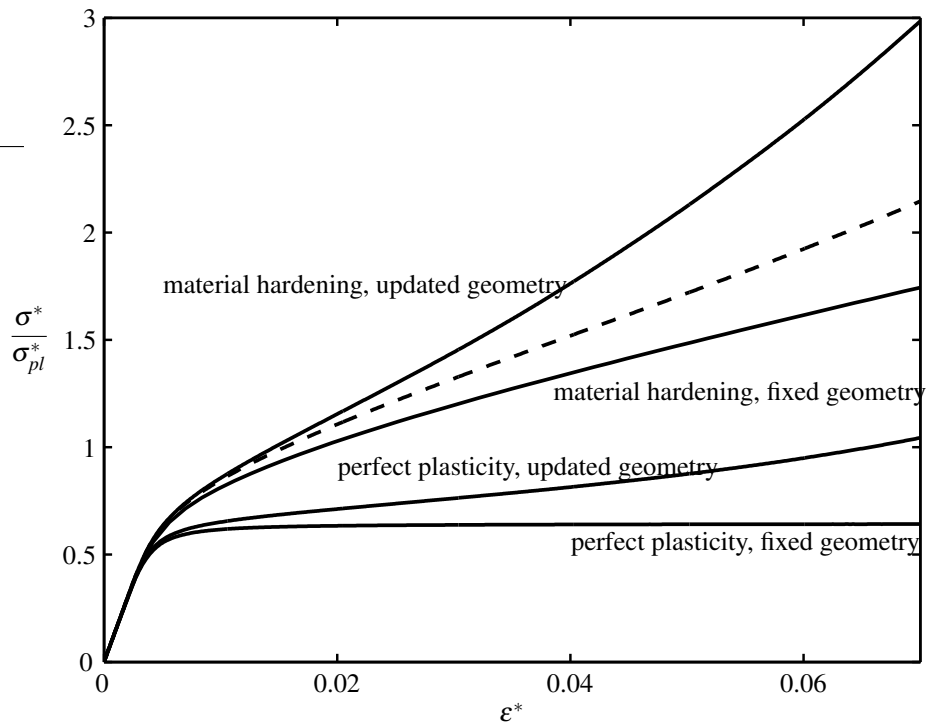


Figure 5.17: Synergy of material and geometrical hardening in the Voronoi network. This figure is constructed analogous to figure 5.12. Again we note that $\sigma_{pl}^* = 2/3\sigma_{ys}(\rho^*/\rho_s)^2$, however the foam does not yield at $\sigma^* = \sigma_{pl}^*$. See the text for an explanation.

the powers of the scaling relationships of the plastic modulus. It should also be noted that the boundary conditions of single struts in a foam are very different from the free boundary conditions described earlier in this chapter for the unit cell. The real boundary conditions will be some sort of combination of the constrained and the free boundary conditions from the unit cell. However, the coupled and uncoupled model are not that similar for the constrained boundary conditions (see figure 5.3d - 5.3f). The difference is more significant and it will influence the final outcome of the power.

An additional note has to be made on the stress values in figure 5.17. It turns out that the foam does not yield at $\sigma^* = \sigma_{pl}^*$, but at a lower stress (remember that $\sigma_{pl}^* = 2/3\sigma_{ys}(\rho^*/\rho_s)^2$). This is also seen in literature [13],[14]. For 2D Voronoi networks the yield stress is lower compared to those of regular hexagonal honeycombs.

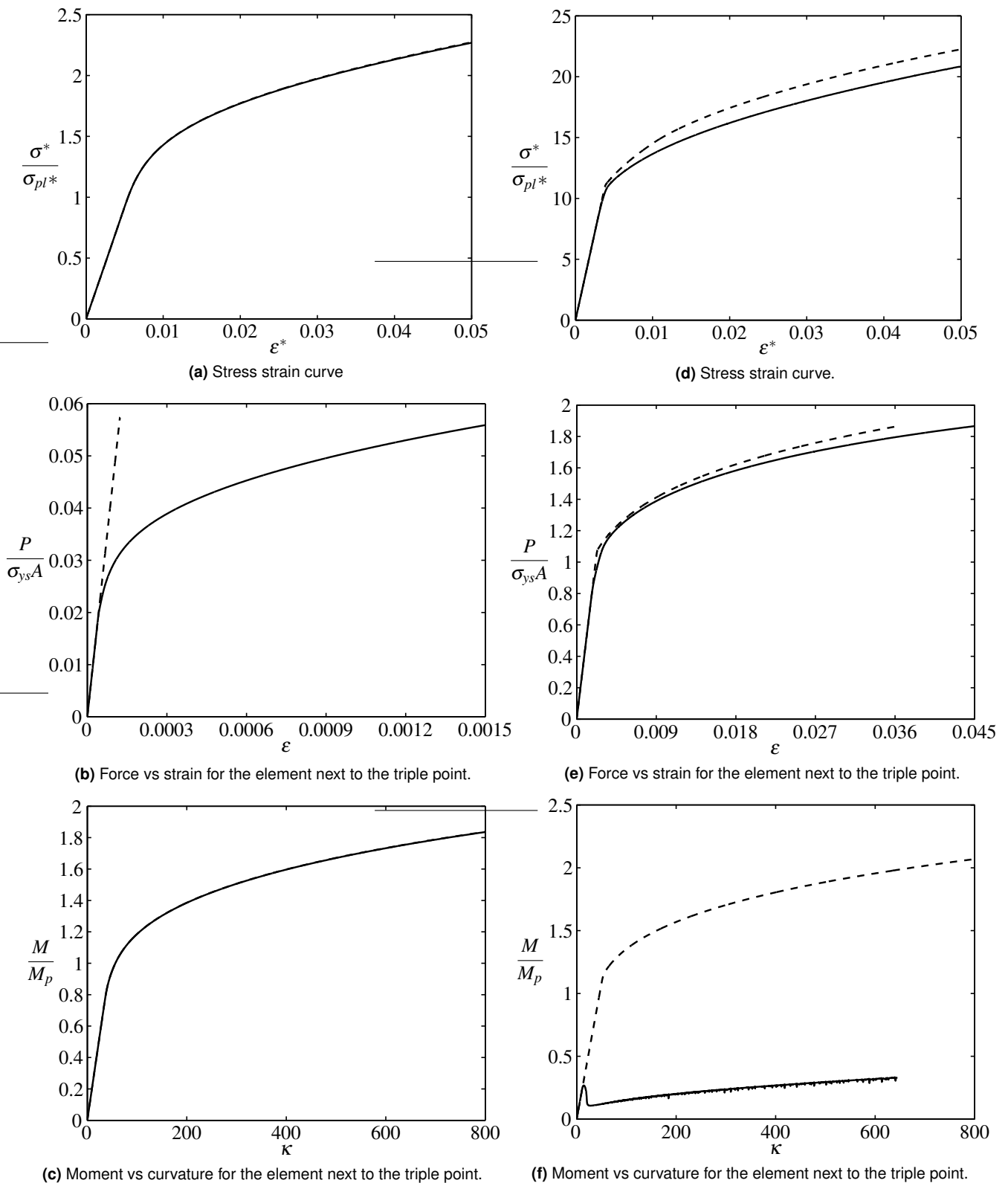


Figure 5.18: Comparison between unit cell with the coupled model (solid lines) and with the uncoupled model (dashed lines). Power law hardening. Figures 5.18a-5.18c consider the free boundary conditions, figures 5.18d-5.18f consider the constrained boundary conditions.

5.2 Power law hardening

Now the material behaviour is changed to a power law. For the moment it will be written as

$$\sigma_0(\epsilon_{pl}) = \sigma_{ys} \left(1 + \frac{E}{\sigma_{ys}} \epsilon_{pl} \right)^{m_s}, \tag{5.9}$$

where m_s is the (solid material) hardening exponent and ϵ_{pl} represents plastic strains ($\epsilon_{pl} = \epsilon - \sigma_{ys}/E$).

The effect of coupling will be studied for a power law hardening material and the plasticity development in the strut will be analysed and compared for different hardening exponents. For different relative densities simulations are performed on the unit cell and on 16×20 Voronoi networks for different hardening exponents and a fixed yield stress. A fitting method to obtain the hardening exponent of the foam will be proposed and described. Finally, the scaling of the hardening exponent of the foam (m^*) versus the hardening exponent of the solid material (m_s) will be investigated and discussed.

5.2.1 Deformation of a strut in an hexagonal unit cell

In figure 5.18 on page 42 the coupled and uncoupled model are compared for the unit cell with two boundary conditions (free and constrained). The difference occurs in similar places if the figure is compared to figure 5.3. The stress levels are a bit lower because for power law hardening the solid material's rate of hardening is low at larger material strains. Since all of the simulations concerned with power law hardening are performed with the coupled model, we do not have to worry about the differences (and possible errors) between the coupled and uncoupled model for the constrained boundary conditions. Figure 5.18 is shown for completeness. From now on all the results will be with the coupled model.

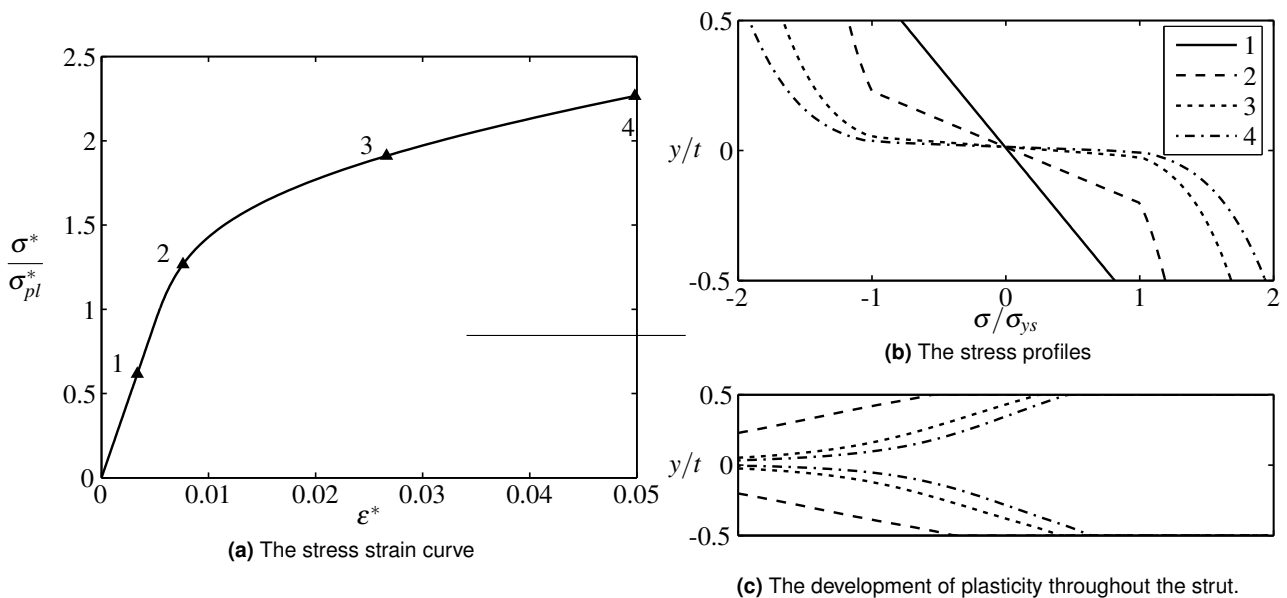


Figure 5.19: Development of plasticity for power law hardening and free boundary conditions.

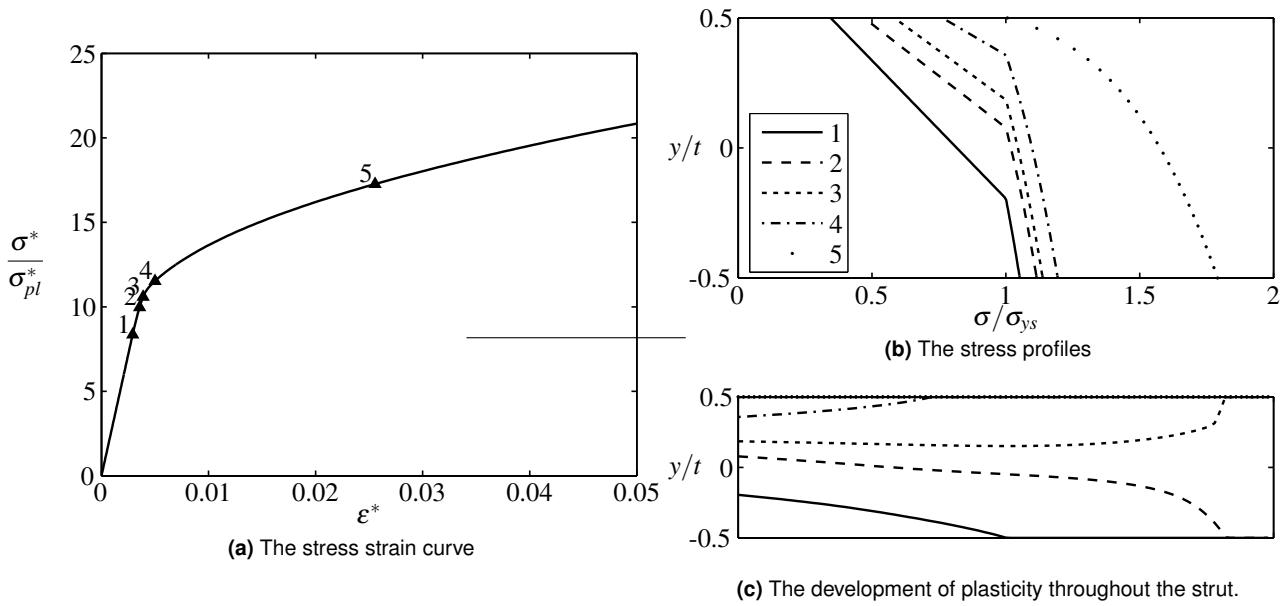


Figure 5.20: Development of plasticity for power law hardening and constrained boundary conditions.

Continuing on similar lines as for linear hardening the stress profiles and development of plasticity are shown for the upper strut in the unit cell. The stress levels are a bit lower than for linear hardening, but apart from this the pictures look similar to those with linear hardening. See figure 5.19 for the case with the free boundary conditions and figure 5.20 for the case with the constrained boundary conditions. In the appendix one can find the stress profiles within the upper strut for the corresponding increments selected from the simulations.

It will be more interesting to see the effect of the hardening exponent at a strut level. This will be done in a quantitative manner in the next section by comparing the input hardening exponent of the material (m_s) with the hardening exponent of the foam (m^*). In this section only the influence of hardening on the development of the stress profiles and plasticity is studied. For the unit cell simulations with fixed geometry and updated geometry conditions were performed using different

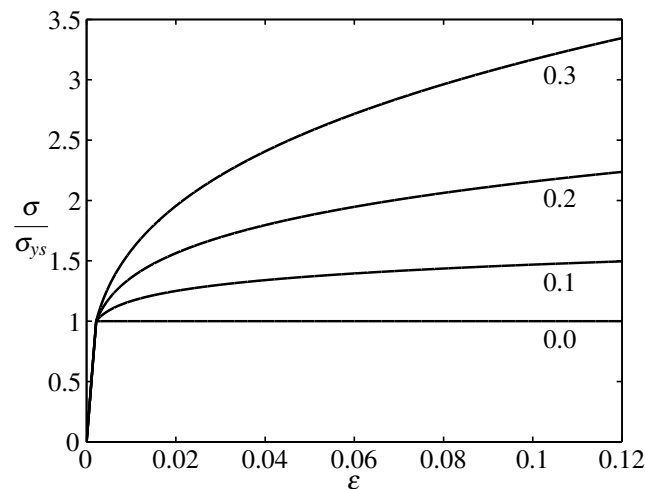


Figure 5.21: Solid material stress strain curves with different hardening exponents (see the numbers in the plot) and with a fixed yield stress ($\sigma_{ys} = 150\text{MPa}$).

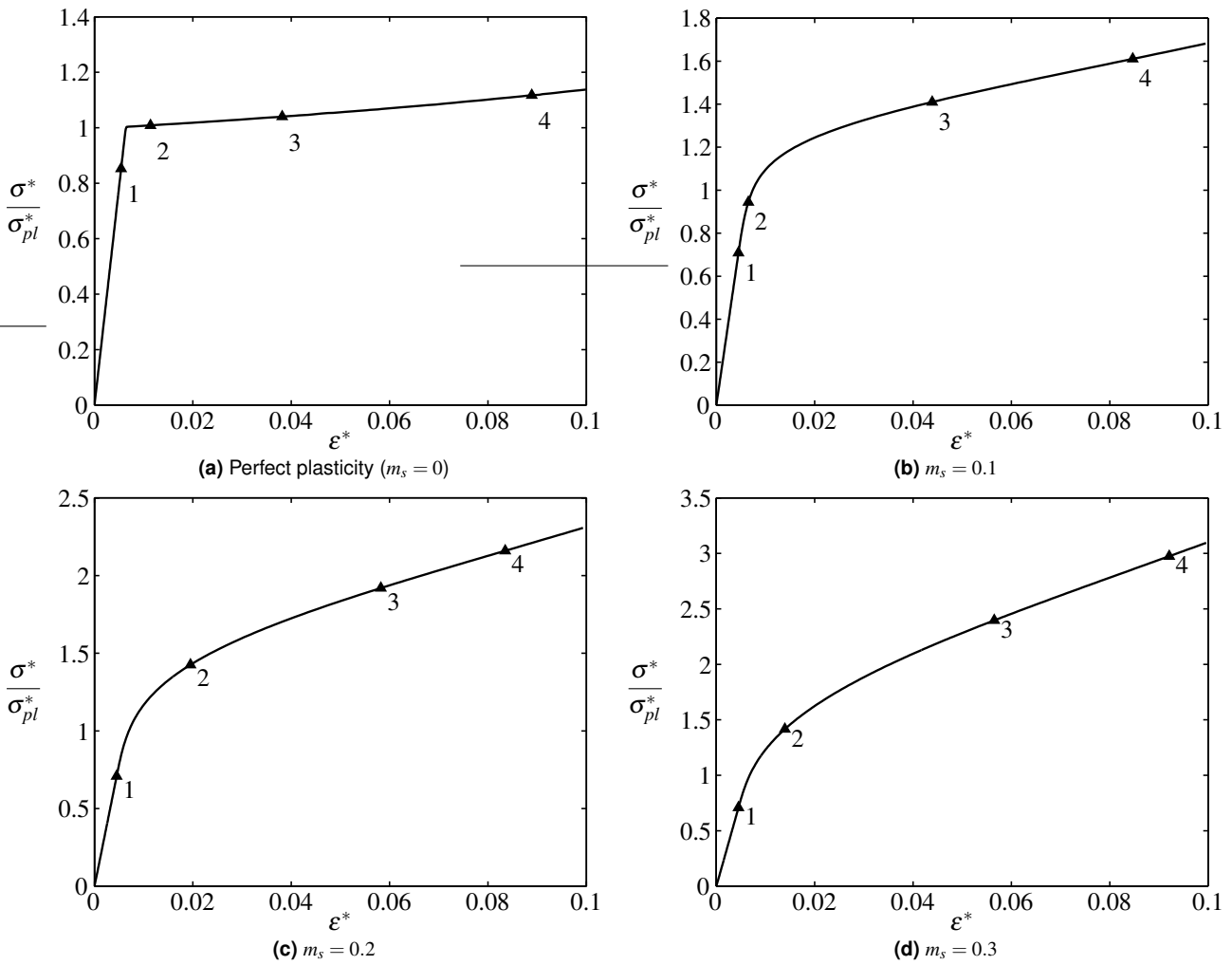


Figure 5.22: Stress strain curves for the unit cell with finite strain, different hardening exponents and a fixed yield stress.

hardening exponents for the solid material (see figure 5.21 for the input curves). The free boundary conditions are used.

Figure 5.22 shows the stress strain curves of the unit cell with different solid material hardening behaviour (shown in figure 5.21). The perfect plasticity case clearly shows a slope discontinuity. This is where the plasticity localizes in the elements close to the triple point. After this slope discontinuity the curves keeps slowly increasing. This does not happen for the fixed geometry case where the lines continues to be straight at the same stress level. The trends in the other curves (figure 5.22b - 5.22d) correspond to their input curves. A higher hardening exponent m_s will result in more hardening and higher stress values for the unit cell.

The stress profiles of the element next to the triple point in the upper strut are shown in figure 5.23. The numbers in the legend in figure 5.23c correspond to the indicated points in the stress strain curves in figure 5.22. When the hardening exponent increases the stress profiles reach higher stress levels at their outer (plastic) fibers for the same applied strain. This is expected since these curves are directly related to the solid material behaviour.

In figure 5.24 one will find the development of plasticity for the upper strut of the unit cell for different hardening exponents. Figure 5.24a shows the case for perfect plasticity. After a short

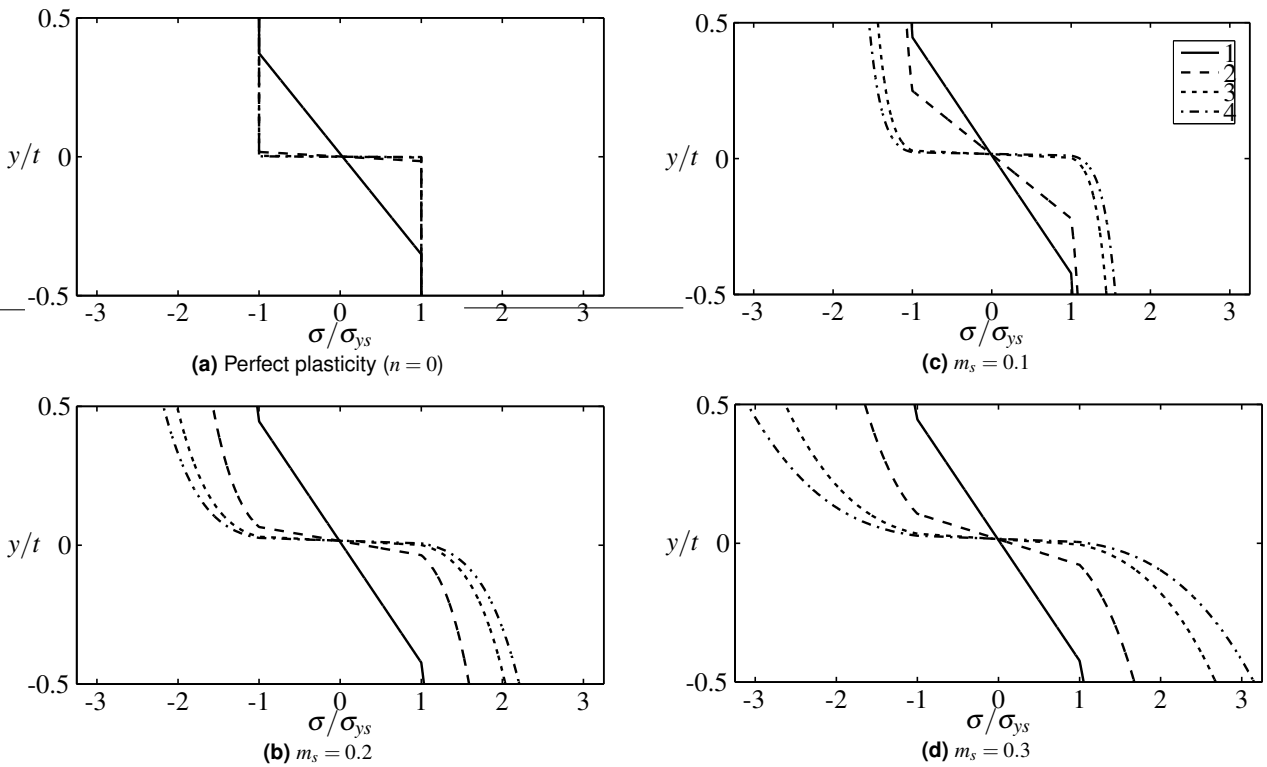


Figure 5.23: Stress profiles for the unit cell with updated geometry, different hardening exponents and a fixed yield stress.

period of lateral spreading, plasticity localizes in the elements close to the triple point and keeps on spreading - although very slow - further along the beam. It clearly shows the formation of a hinge next to the triple point. For the last printed increments the elastic core has almost vanished and has become unobservable in this figure. This clearly is different for figures 5.24b - 5.24d, where it is not so obvious that plasticity localizes in a few elements next to triple point. Plasticity does spread inwards for the elements next to the triple point, but this also happens for many more elements along the strut. The more the hardening exponent is increased the further plasticity spreads along the strut and inwards the beam elements. For the perfect plastic case only a small percentage of the

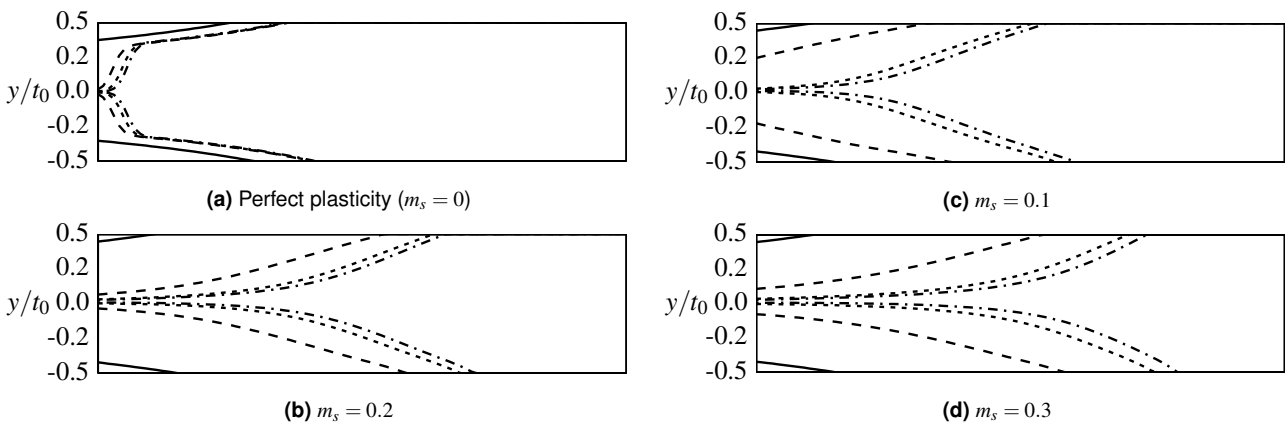


Figure 5.24: Spread of plasticity throughout the beam of the unit cell with finite strain, different hardening exponents and a fixed yield stress.

area has become plastic for the final increment, but for the case where $m_s = 0.3$ almost 75% of the beam elements has started yielding. The last three cases are clearly not hinging, they look more like bending structures.

5.2.2 Scaling relationships for regular hexagonal honeycombs

This and the next subsection will deal with the fitting and comparison of the hardening exponent of the foam and the solid material. For input the same curves as in the previous section are used. The reader is referred to figure 5.21. It also was mentioned in the previous section that the difference between the curves for a fixed geometry and an updated geometry is small for regular hexagons. In figure 5.25 this indeed turns out to be the case.

The next step is to fit our hardening relation (equation (5.9)) to the stress strain curves of the unit cell and compare its hardening exponent with the solid material hardening exponent.

A nice property of equation (5.9) is that it can be rewritten to

$$\sigma_0(\varepsilon) = \sigma_{ys}^{1-m} E^m \varepsilon^m, \tag{5.10}$$

which is a function of total strain ε instead of plastic strain ε_{pl} . To make a proper fit of the plastic part of our curve, first the elastic part needs to be excluded. This is achieved by drawing a line parallel to the elastic part of the curve with a small (positive) offset. The initial point of yielding lies on the intersection of these curves. By doing this we obtain the point where the curve starts to deviate from the elastic curve and which also is the end point of the elastic range¹.

Young's modulus is easily obtained since it is the slope of the elastic range. The yield stress is also obtained prior to the fitting. How this is done will be explained later on. The nice property of this hardening relation is that the fitting only depends on the hardening exponent m .

In principal Young's modulus and yield stress should be filtered out when fitting by this procedure, but unfortunately there still is some bias when fitting for different relative densities. Therefore, for

¹This method is analogous to the .2% offset method, however here the offset is taken very small.

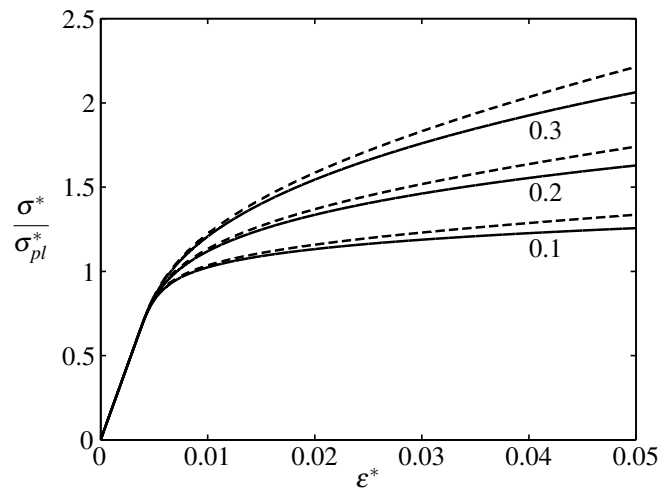


Figure 5.25: Stress strain curves of the unit cell for the different input hardening exponents (see the numbers in the figure next to the curves) for updated geometry (solid lines) and fixed geometry (dashed lines). These curves are for the relative density of $\rho^*/\rho_s = 12\%$.

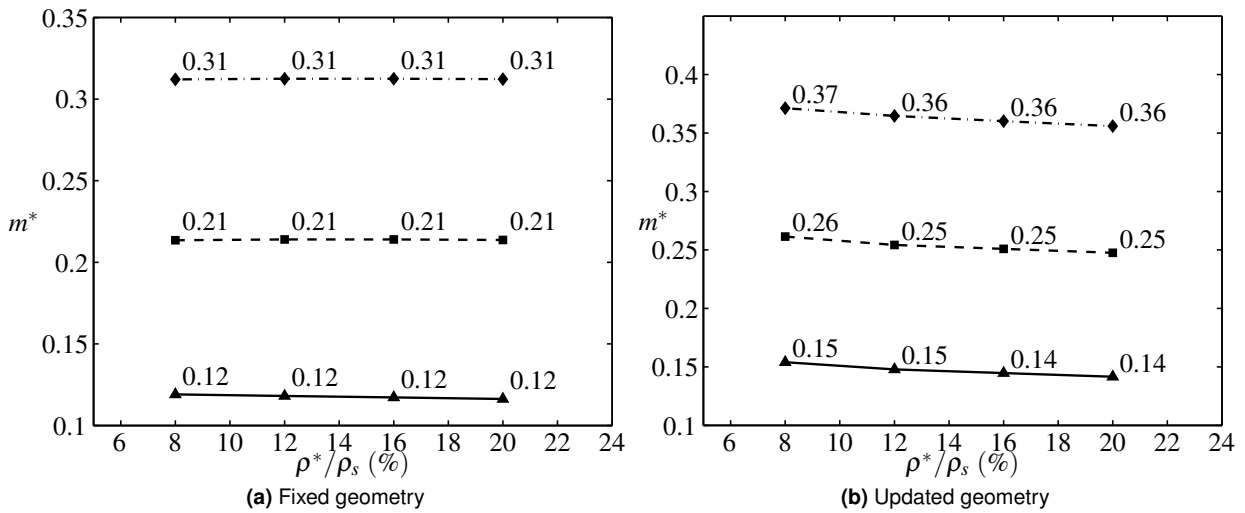


Figure 5.26: Hardening exponents versus relative density for different input hardening exponents. The corresponding hardening exponent of the foam is mentioned in the graph near the curves. The solid curves have $m_s = 0.1$, the dashed curves have $m_s = 0.2$ and the dashed-dotted curves have $m_s = 0.3$.

all relative densities the curves are scaled such that the initial point of yielding falls on $(\sigma^*)' = 1$ and $(\epsilon^*)' = 1$. This can be achieved when for each density $(\sigma^*)' = \sigma^*/\sigma_{pl}^*$ and $(\epsilon^*)' = \epsilon^*/\epsilon_{pl}^*$. Another difficulty is that the input function which is used for fitting has a slope discontinuity. This slope discontinuity can clearly be seen in figure 5.21 on the point where the material starts to yield. Although the elastic range is ignored for fitting the fitting function cannot take into account the smooth transition between the elastic and plastic part of the stress strain curve of the foam. To be able to make a correct fit a small range after the initial point of yielding should also be ignored. Finally, the simulation with an updated geometry starts to harden more at larger strains. This happens because the struts in the foam start to align, which make the foam stronger. Obviously this effect needs to be ignored. The solution is to take different fitting ranges for different densities keeping the lower and upper bounds of the ranges very close (in a low relative density foam struts tend to align sooner than in a high relative density foam).

Figure 5.26 shows the hardening exponents of the unit cell versus relative density for the situation with fixed geometry and the situation with updated geometry. The foam's hardening exponents for fixed geometry clearly match the material's hardening exponents with a small error. Furthermore, they are independent of the relative density. When the geometry is updated during the simulation, there appears a dependency on the relative density. Also it is evident that the foam's hardening exponent (m^*) is not equal to its solid material's exponent (m_s) anymore.

5.2.3 Scaling relationships for converged Voronoi networks

The same study is performed for Voronoi networks. Networks of 16×20 cells are used with the boundary conditions mentioned in the previous chapter. The results for one relative density ($\rho^*/\rho_s = 12\%$) are shown in figure 5.27. Please observe the greater relative difference between the fixed geometry and the updated geometry curves compared to figure 5.25.

Looking at figure 5.28 one observes the same trend as for the unit cells. For fixed geometry the hardening exponent matches the solid material's hardening exponent and is independent of density.

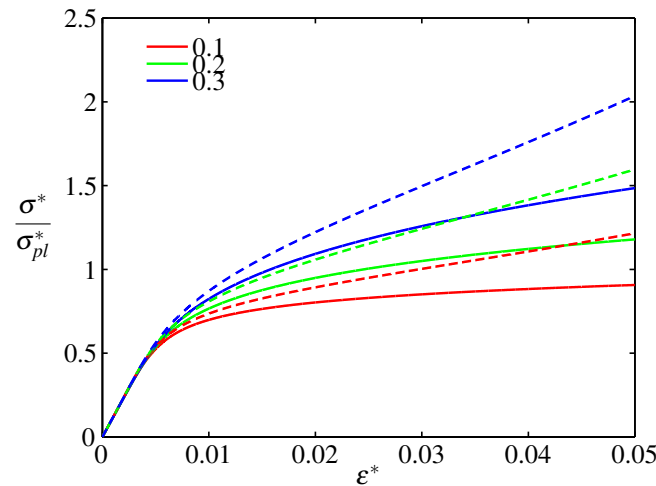


Figure 5.27: Stress strain curves of Voronoi network for different input hardening exponents (the numbers in legend are the hardening exponents.) for finite strains (solid lines) and small strains (dashed lines). These curves only are for the relative density of $\rho^*/\rho_s = 12\%$

For updated geometry the foam’s hardening exponent does not match the solid material’s exponent and the difference is even larger than for the unit cell. It also is dependent on relative density.

Why the fixed geometry’s hardening exponents match those of the solid material can be understood. For a fixed geometry the realization will remain in its original configuration. All the angles, node positions and beam lengths will remain the same. For the case of the unit cell an applied displacement in the top node will result in a distribution of the axial strain and the curvature depending on the angle. Since the configuration remains constant, the overall force is just the redistributed value of the original material behaviour. Their structure exists of course out a lot of elements which make the calculations of the force more complicated, but if the geometry remains fixed it is just a distribution which remains the same if the geometry remains the same. The final outcome may differ, but the trends observed in this will match the trends of the material behaviour, including the

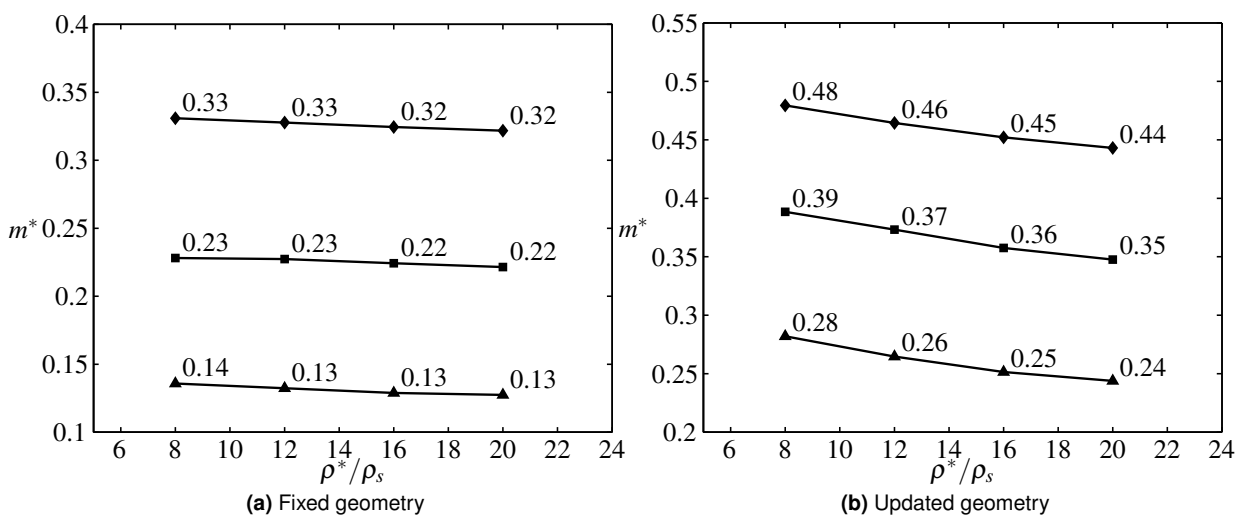


Figure 5.28: Hardening exponents of a Voronoi network versus relative density for different input hardening exponents. The curve with triangle shaped points has an input exponent of $m_s = 0.1$, the curve with square shaped points $m_s = 0.2$ and the curves with diamond shaped points $m_s = 0.3$.

hardening exponent. This argument also holds for the Voronoi networks. The distribution is simply more complex, but for a fixed geometry the trend of the curve is unchanged.

5.2.4 Strain maps for different hardening exponents

With the strain mapping method described in chapter 3 strain maps for different hardening exponents in tension and compression are produced to analyse the effect of hardening on the distribution of strain.

Figure 5.30 on page 52 shows strain maps for tension for perfect plasticity, $m_s = 0.1$ and $m_s = 0.2$. In figure 5.31 on page 53 strain maps for compression for the same solid material hardening exponents are shown. The numbers mentioned with each strain map correspond to the indicated points in figure 5.29a for tension and figure 5.29b for compression.

On average the strain maps in tension are the same for comparable strains. Taking a closer look reveals some more localization for the perfect plastic case. Compare for example figure 5.30b with figure 5.30e. The strain map for perfect plasticity shows more localization than the strain map with $m_s = 0.1$. The strain values in the regions where strain localized for the perfect plastic strain map are comparable with the values in the same regions of the strain map with $m_s = 0.1$. Even when the overall strain value of perfect plastic strain map is lower than the one with $m_s = 0.1$. However, the effect is still very small. Changing the solid material's hardening exponent does not significantly affect the strain distribution when a Voronoi network is loaded in tension.

If a voronoi network is loaded in compression the results are very different. For perfect plasticity a clear band is forming and almost all the displacement takes place in this band. For larger strains displacements also seems to occur in a second band at a different angle. In the strain maps with $m_s = 0.1$ strain again takes place in the same band as the strain maps for perfect plasticity. Now, however, the strain values are smaller and straining spreads throughout the structure, it is not localized around one of the bands as observed for perfect plasticity. Increasing the hardening exponent of the solid material results in even more spreading of strain, which is shown in the strain maps for $m_s = 0.2$.

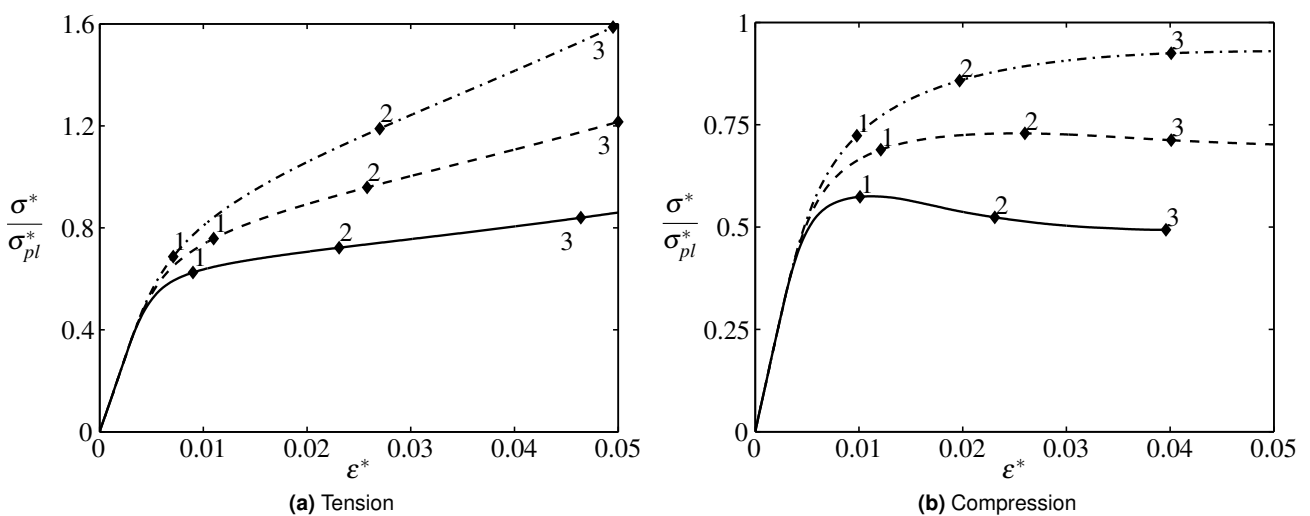


Figure 5.29: Stress strain curves of a Voronoi network for different hardening exponents. The solid lines correspond to the Voronoi with a perfect plastic material, the dashed lines are with material with $m_s = 0.1$ and the dashed-dotted lines are with $m_s = 0.2$

Thus, decreasing the hardening exponent of the solid material will result in more localized strain in a Voronoi network loaded under compression. A lower m_s results in a structure where hinge formation in struts is more common (this is shown in detail in section 5.2.1). If hinge formation is more likely, defects in the Voronoi network are also more likely to reveal themselves which results in the collapsing of cells. Once this is happening strain is more likely to localize around these defects unloading the rest of the structure.

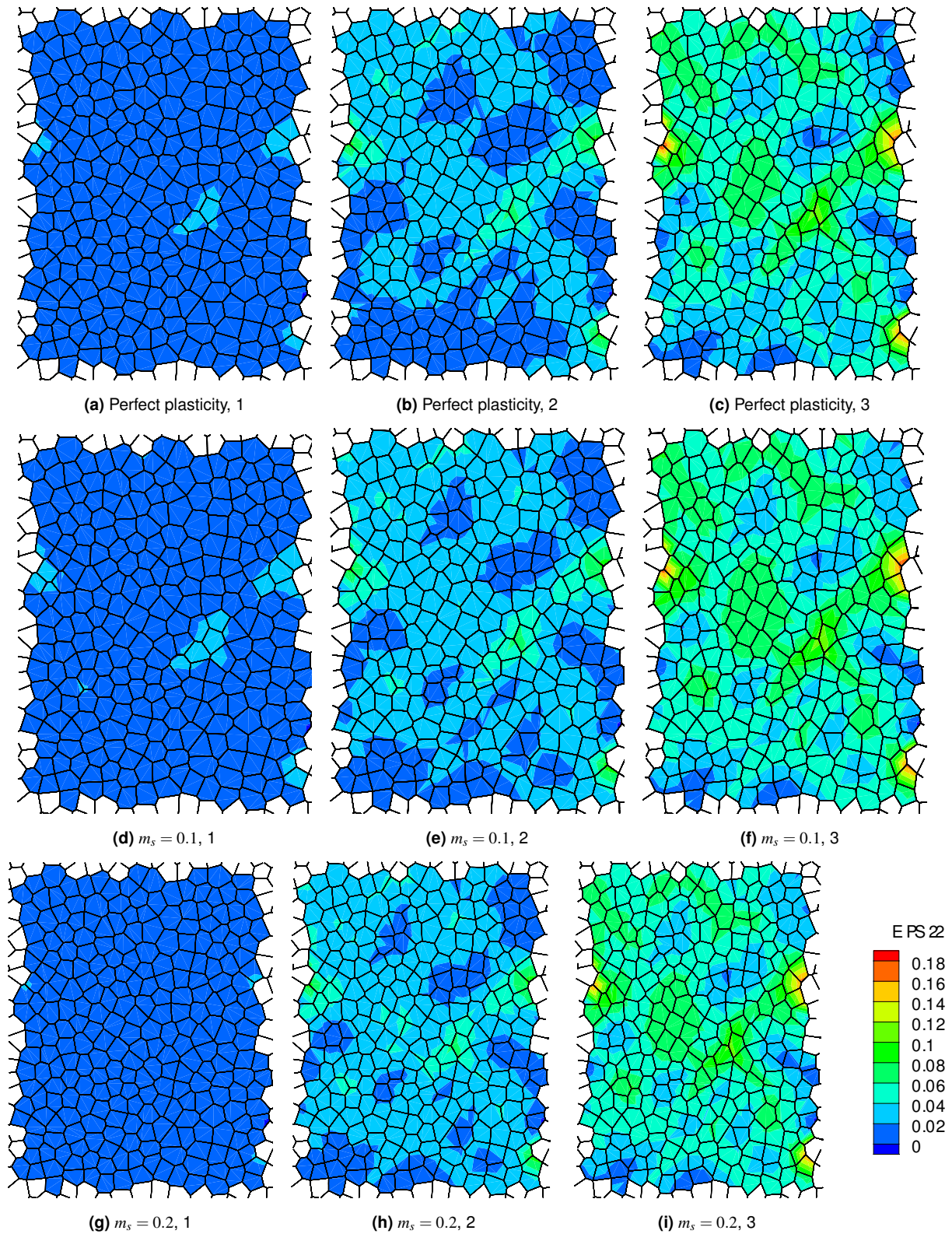


Figure 5.30: Strain maps in tension for different solid material hardening exponents.

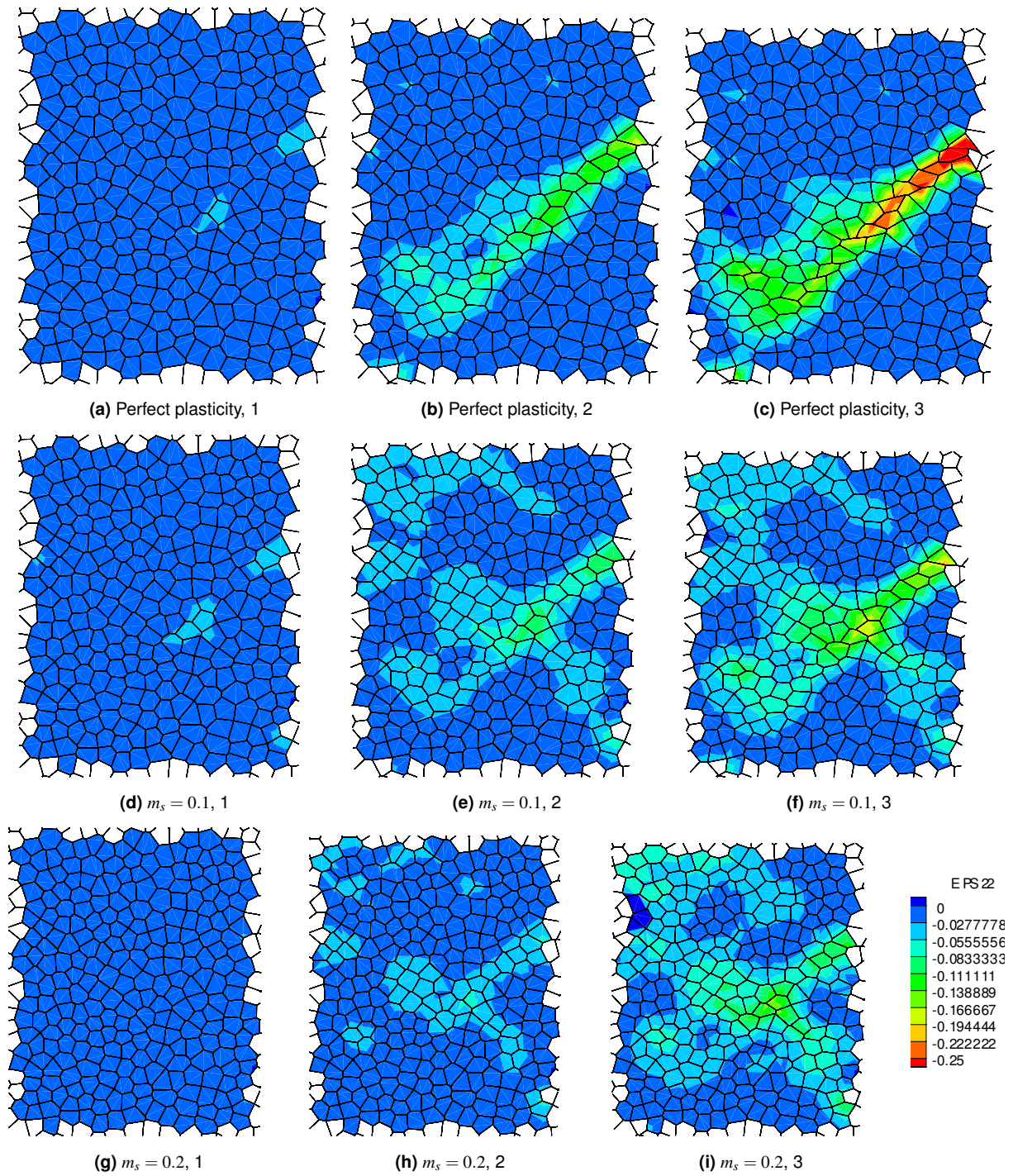


Figure 5.31: Strain maps in compression for different solid material hardening exponents.

5.3 Non-uniform cross-section

For the non-uniform cross-section a strut profile given by equation (5.11) is used. The advantage of this function is, that it always will give the same area for any relative thickness (t_{rel}), making it suitable for comparison between different relative thicknesses. This relative thickness determines the non-uniformity of the cross-section. If $t_{rel} = 1.0$ it will lead to a uniform cross-section along the strut. A value of $t_{rel} < 1.0$ will result in a concave cell wall shape, $t_{rel} > 1.0$ will result in a convex cell wall shape [11].

$$t(\xi) = t_0 \left[3(1 - t_{rel}) \left(\frac{\xi}{l} \right)^2 + t_{rel} \right] \quad (5.11)$$

Figure 5.32 shows a cell wall shape for $t_{rel} < 1.0$.

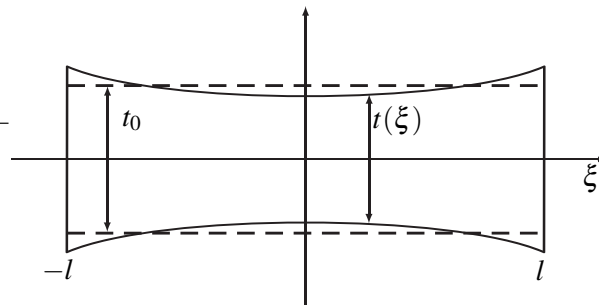


Figure 5.32: A schematic of the non-uniform cross-section keeping the area the same as for a uniform cross section with thickness t_0 .

Now, results for the unit cell with a non-uniform cross-section (NUCS) are shown. The same strut deformation analysis which was done for the unit cell with uniform cross-section (UCS) will be performed for the NUCS. For the NUCS a relative thickness of $t_{rel} = 0.7$ was used. Figure 5.33 shows the stress strain curves in comparison to those of the UCS. The indicated points in these curve correspond to the moments during the simulations where the stress profiles were taken. Figure 5.34 shows the stress profiles at the point of action, where plasticity occurs first and has a maximum depth of plasticity penetration at all the times (indicated with a vertical line in the development of plasticity plots in figure 5.35). Figure 5.35 shows the development of plasticity throughout the upper strut of the unit cell. The bottom curves for the case with free boundary conditions are ζ^{\ominus} , the top curves ζ^{\oplus} . When the constrained boundary conditions are applied one only observes ζ^{\ominus} .

The NUCS structures with free boundary conditions appear to be much stronger than the UCS structures. As was stated before, the unit cell (with free boundary conditions) is a bending structure. It will try to bend near the tripple point. Here, however, the strut is the thickest in this place. It is unlikely to bend at this location. As Figure 5.35 will point out, the majority of the plasticity takes place in the middle of the strut. Here it will be less hard to bend since the strut is less thick here (about the same thickness as the UCS), but it also will be more difficult to deform the structure since it is further away from the tripple point. The NUCS cases with the constrained boundary conditions on the other hand are weaker than UCS structures. Since the upper strut of the unit cell with these boundary conditions is for the majority under tension it depends on the weakest elements in the strut. In this case these are the thinnest elements in the upper strut of the unit cell, which are clearly not so strong as the elements in UCS's struts, which all have the same (and compared to the NUCS's thinnest elements larger) thickness.

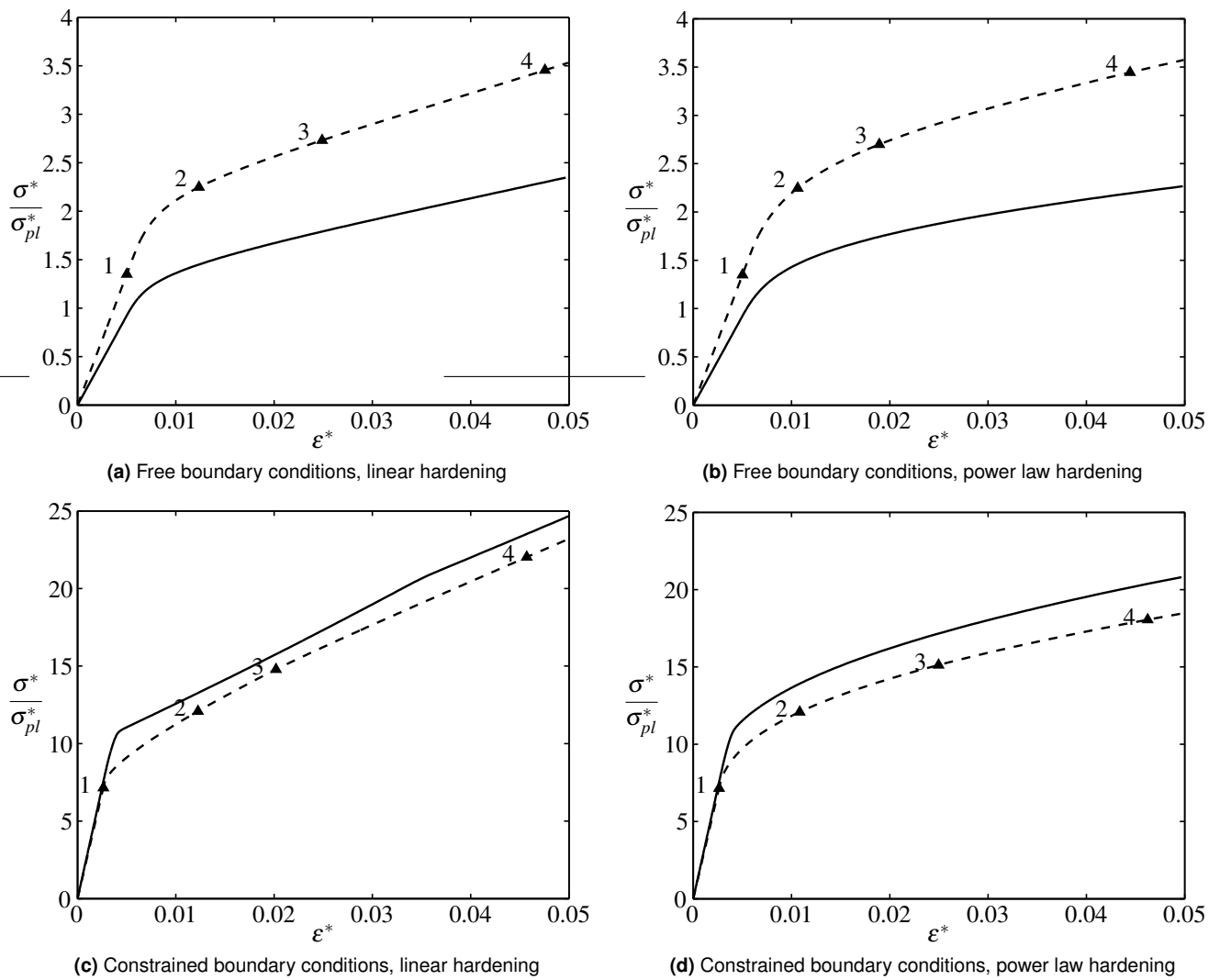


Figure 5.33: Comparison between unit cell with cell walls which have a uniform cross-section (solid lines) and cell walls with a non-uniform cross-section (dashed lines). The indicates points in each curve correspond to a linestyle in figures 5.34 and 5.35. 1 corresponds to the solid lines, 2 to the dashed lines, 3 to the dotted lines and 4 to the dashed-dotted lines in figures 5.34 and 5.35.

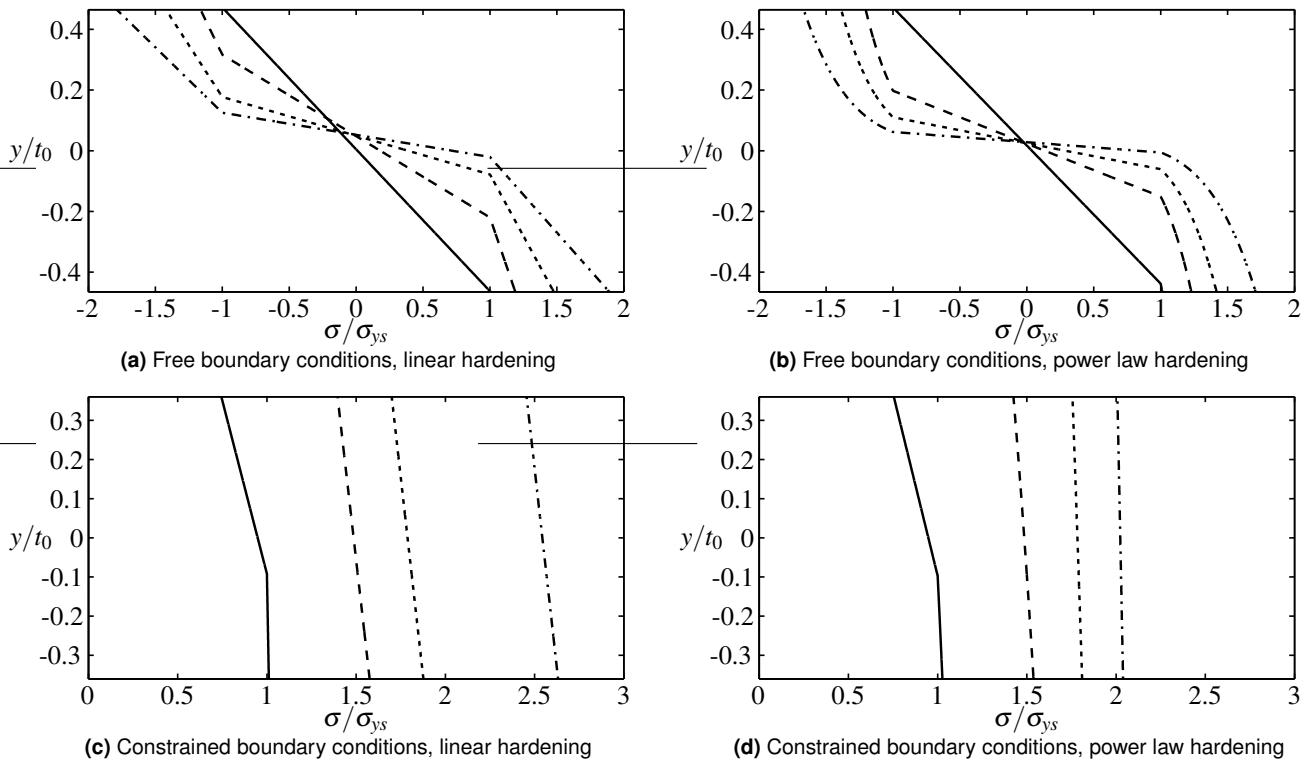


Figure 5.34: Stress profiles of the unit cell with non-uniform cross-section.

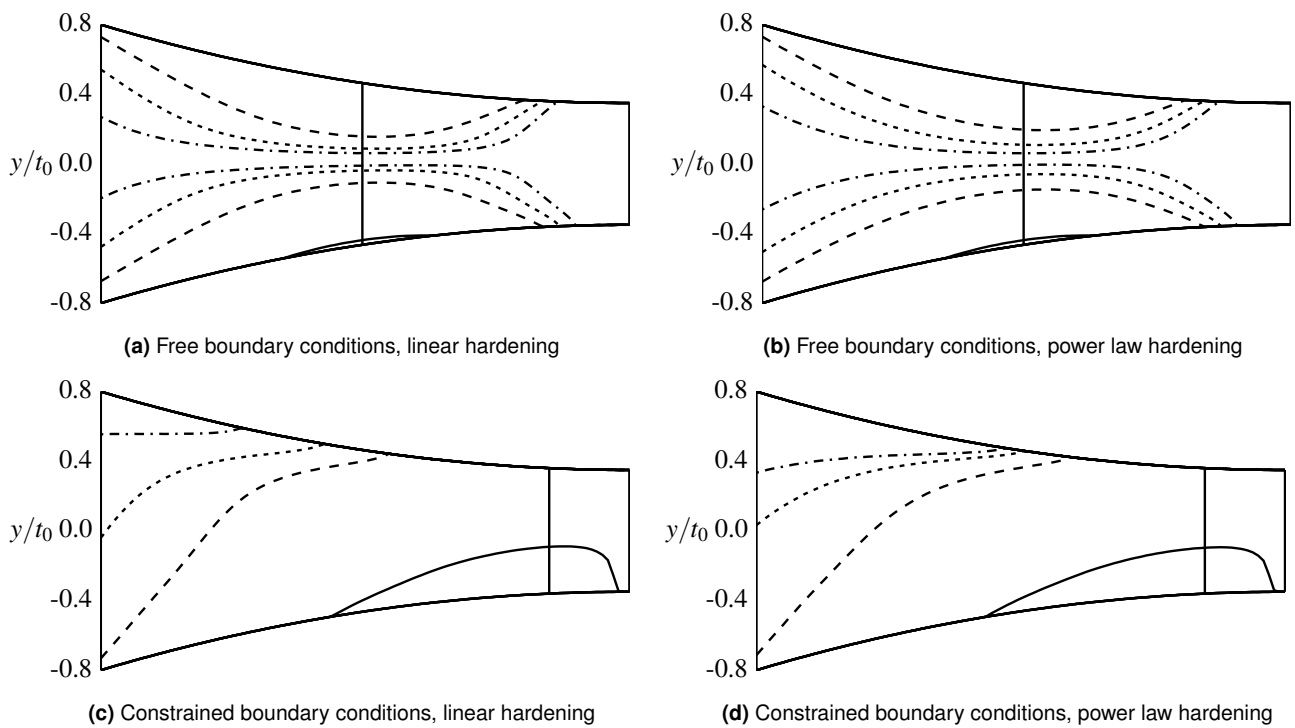


Figure 5.35: Spread of plasticity in the upper strut of the unit cell with non-uniform cross-section.

6

Heat treatments

As mentioned in the introduction heat treatments can significantly change the mechanical properties of the solid material and therefore of the foam. Thus, a more detailed look into the effects caused by these treatments is desirable.

The differences between T6-strengthened (T6) and annealed (O) foams have their origin in the microstructure. T6-strengthened material has a significantly different grain structure when compared to annealed materials. In this chapter the differences between the two heat treatments are incorporated by adjusting the material parameters such as the yield strength and the hardening exponent.

6.1 Definition of the heat treatments

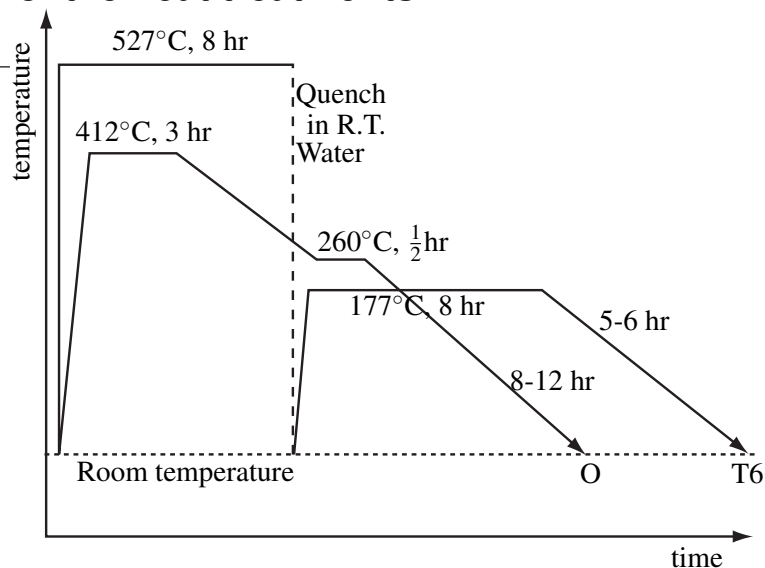


Figure 6.1: Diagram explaining the used heat treatments, T6-strengthening (T6) and annealing (O).

Two heat treatments used by industry have been chosen to use as input for the simulations. In figure 6.1 the definition of the two used heat treatments - T6 and O - is explained.

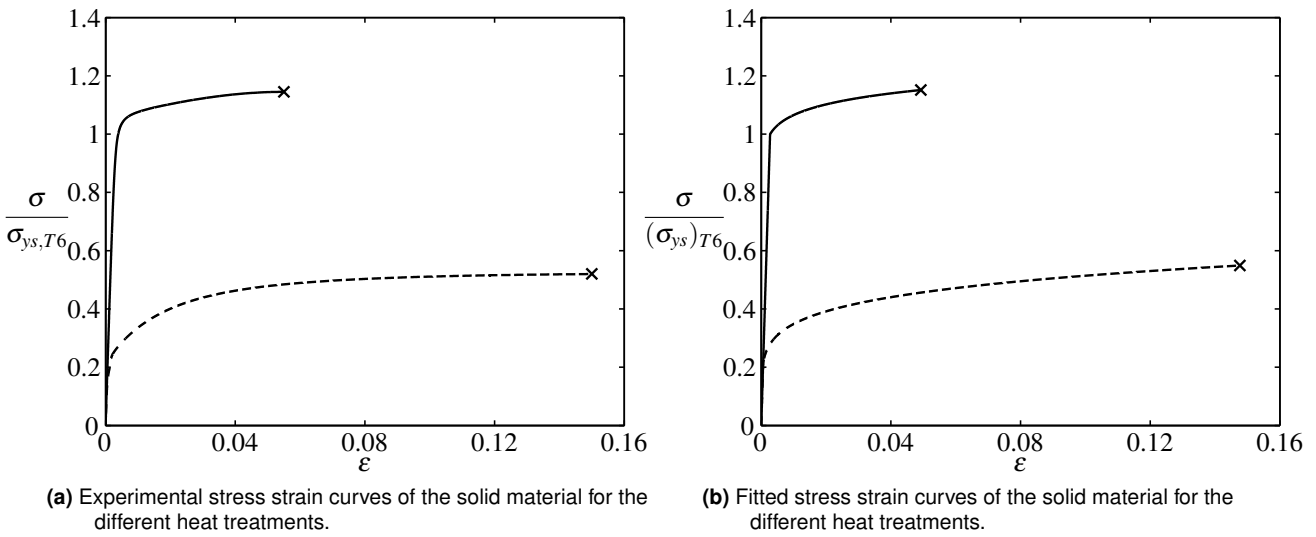


Figure 6.2: Experimental and fitted stress strain curves in tension for two solid materials subjected to different heat treatments. The solid curve is a fit for the T6 material, the dashed curve for the O material. The point where a curve stops indicates the failure stress.

During the T6-strengthening process the foam is first solutionized at 527°C for 8 hours, after which it is quenched in water to room temperature. After this the foam is aged at 177°C for another 8 hours. The annealing process involves soaking at 412°C for 3 hours followed by a two-step furnace cooling to room temperature [7].

These heat treatments significantly change the mechanical properties of the foam. T6-strengthened solid material will have a higher yield stress, but the failure strain will be lower than the failure strain of an annealed material. There also is a significant difference in the hardening. The hardening exponent of an annealed material will be higher than the hardening exponent of a T6-strengthened material. In figure 6.2 one can find the stress strain curves of two solid materials from which each was subjected to one of the heat treatments.

The function $\sigma_0 = \sigma_{ys}(1 + E_s/\sigma_{ys}\epsilon_{pl})^{m_s}$ is fitted as good as possible to the experimental curves. The parameters of these fittings can be found in table 6.1.

heat treatment	$\sigma_{ys}(\text{MPa})$	m_s	$\sigma_f(\text{MPa})$
O	41	0.169	105
T6	191	0.049	220

Table 6.1: Parameters belonging to the curves in figure 6.2b

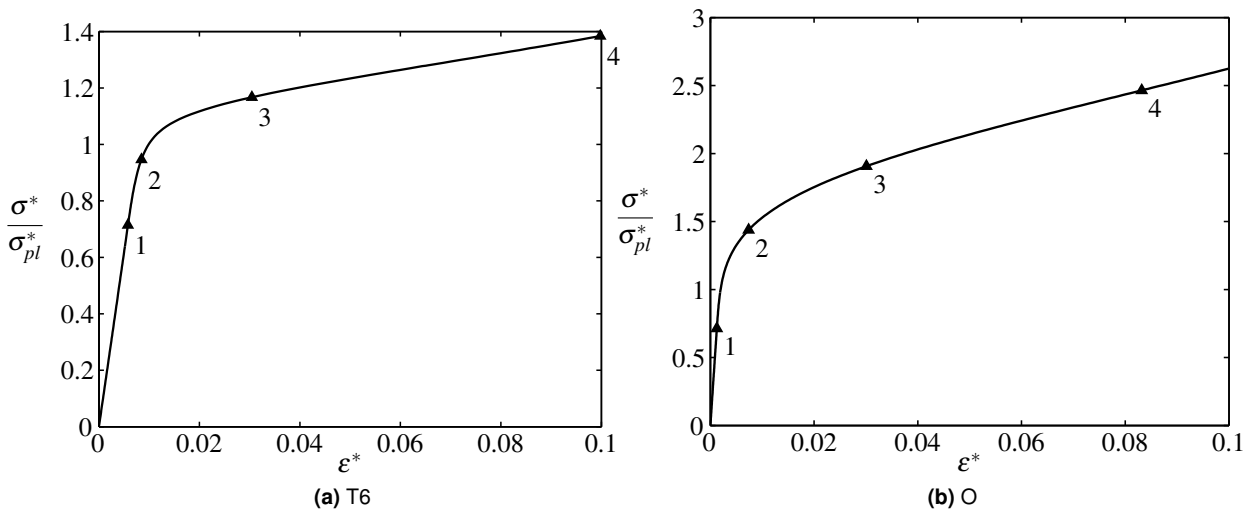


Figure 6.3: Stress strain curves for the unit cell with T6 and O heat treatment for updated geometry and a relative density of $\rho^*/\rho_s = 10\%$.

6.2 Regular hexagonal honeycombs

Now that the model is fitted to experimental data, the parameters from the fit are used for the simulations. Similar to the unit cell in the previous chapter a strut deformation study is conducted. These studies are only performed for the free boundary conditions. After this we shall also compare the hardening exponent of the solid material with the foam’s hardening exponent for the two heat treatments.

6.2.1 Deformation of a strut in an hexagonal unitcell

Figure 6.3 shows the stress strain curves for the two heat treatments for updated geometry and a relative density of $\rho^*/\rho_s = 10\%$. The different hardening exponents of the two heat treatments are reflected in the foam. Also here the indicated points in figure 6.3 correspond to the numbers in figure 6.4 and the linestyle in figure 6.4 correspond to the linestyle in figure 6.5.

Looking at the stress profiles and development of plasticity plots in the upper strut reveals that T6 tends to behave like a perfect plastic material. Especially when only looking to the stress profiles,

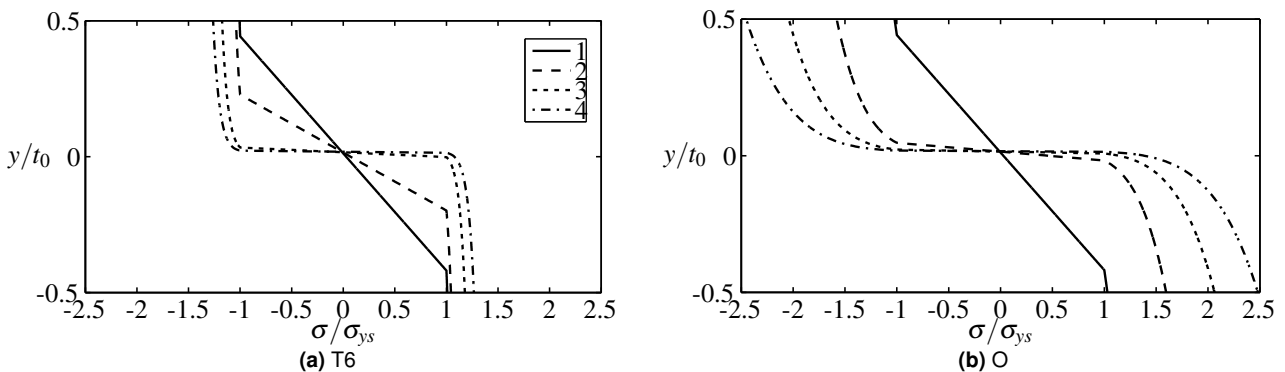


Figure 6.4: Stress profiles for the unit cell with T6 and O heat treatment.

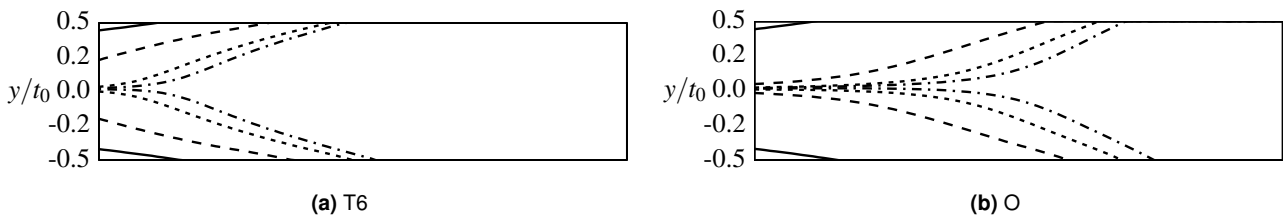


Figure 6.5: Spread of plasticity throughout the upper strut of the unit cell with T6 and O heat treatment.

which have close resemblance with figure 5.23a. It is exaggerated to say that T6 is a perfect plastic material, because there still is a larger number of elements becoming plastic compared to a perfect plastic material. But there is a clear hinge forming close the triple point and one has to conclude that the plasticity is localizing around this hinge.

This is clearly not the case for the O results. Figures 6.3b and 6.4b show a clear hardening trend and in figure 6.5b the hardening is not localizing close to the triple point but spreading throughout the strut.

6.2.2 Hardening

Subsequently the same study done for hardening exponents in section 5.2.2 is done for the different heat treatments. Stress strain curves for one relative density ($\rho^*/\rho_s = 16\%$), the two heat treatments and fixed and updated geometry are shown in figure 6.6. The hardening exponent versus relative density for a fixed and an updated geometry are found in figure 6.7. Again, we arrive at the same conclusion: for fixed geometry the foam's hardening exponent matches the solid material's hardening exponent and is independent of relative density. When the geometry is updated the hardening exponents do not match anymore and the foam's hardening exponent is dependent on relative density.

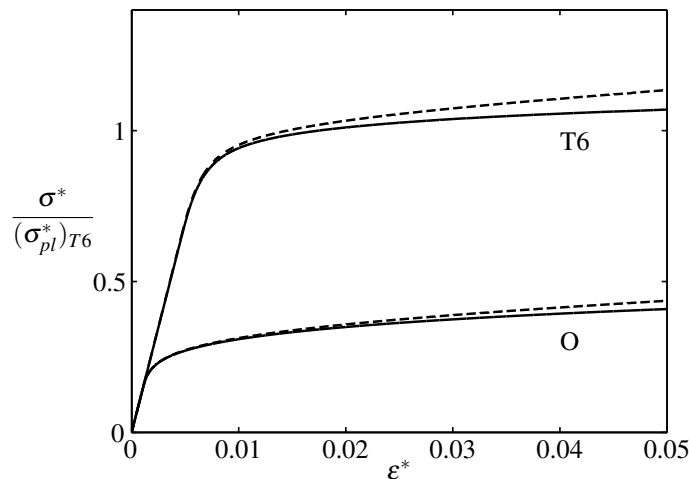


Figure 6.6: Stress strain curves of the two heat treatments for fixed geometry (solid lines) and updated geometry (dashed lines) for the unit cell in tension for a relative density of $\rho^*/\rho_s = 16\%$.

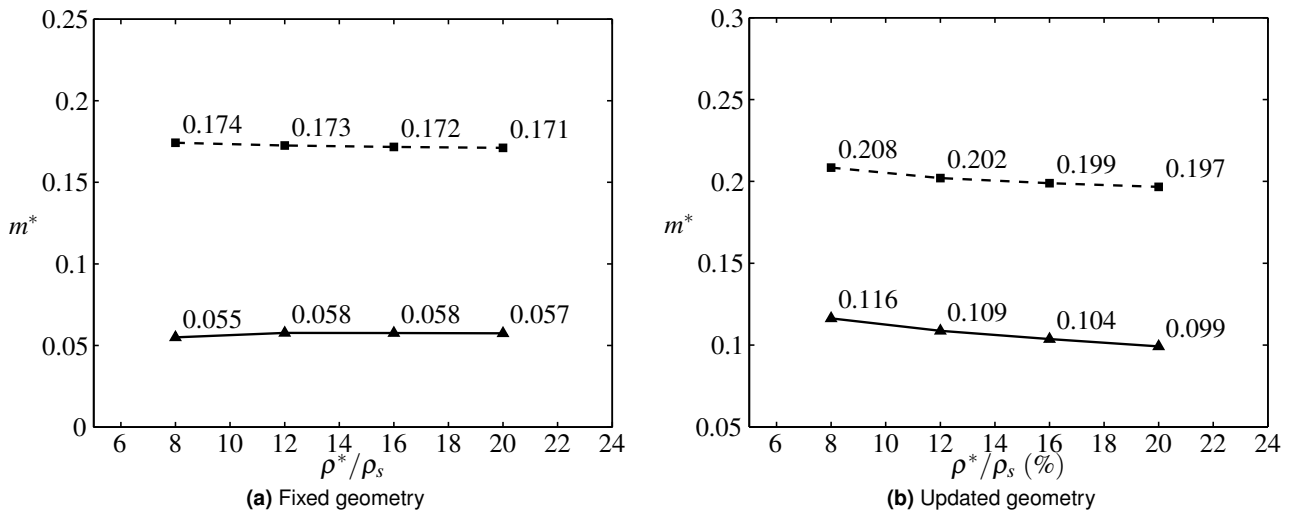


Figure 6.7: Hardening exponents versus relative density for different input hardening exponents concerning the unit cell. The solid lines have an input exponent of $m_s = 0.049$ and the dashed lines $m_s = 0.169$.

6.3 Converged Voronoi networks

The effect of the two heat treatments on the overall behaviour of Voronoi networks is studied in this section. After analysing tension and compression stress strain curves, the solid material hardening exponent (m_s) is compared to the hardening exponent of the Voronoi networks (m^*). Ultimately, a preliminary study of failure (it is called preliminary, because there is no unloading after the failure of a strut) is presented.

6.3.1 Tension versus compression

Simulations for tension and compression were performed for 16×20 Voronoi networks with different heat treatments. The curves for the tension simulations can be found in figure 6.8a and the compression curves are in figure 6.8b.

The stress values of the T6 Voronoi in figure 6.8a are higher than the stress strain curves' stress values of the O Voronoi in figure 6.8a. This is expected since the yield stress and of T6 is higher than O. At the end of the T6 curves the foam starts to harden more. This effect is also seen for the O curves, but here is less prominent. An explanation is the fact that struts will hinge more instead of bending in a T6 foam. This will lead to a foam where struts align more easily in tension, making it harden faster and more pronounced.

The compression curves (see figure 6.8b) on the other hand show a completely different behaviour. After the foam as started to yield it will reach a peak stress, after which it will start to soften. If we look to strain maps for compression we now observe band formation. These bands appear in the weakest regions of the foam. Deformation localizes first at one band after which the displacement will reach a certain limit, the foam will harden again in this band. Then deformation will switch to another band, which now has become the weakest region. Now, the same process starts all over again. This mechanism will occur in both heat treatments, however the way it happens differences for each heat treatment. T6-strengthened foams seem to form bands more easily. As was shown earlier in this chapter in T6 hinges will form more easily making the formation of bands more

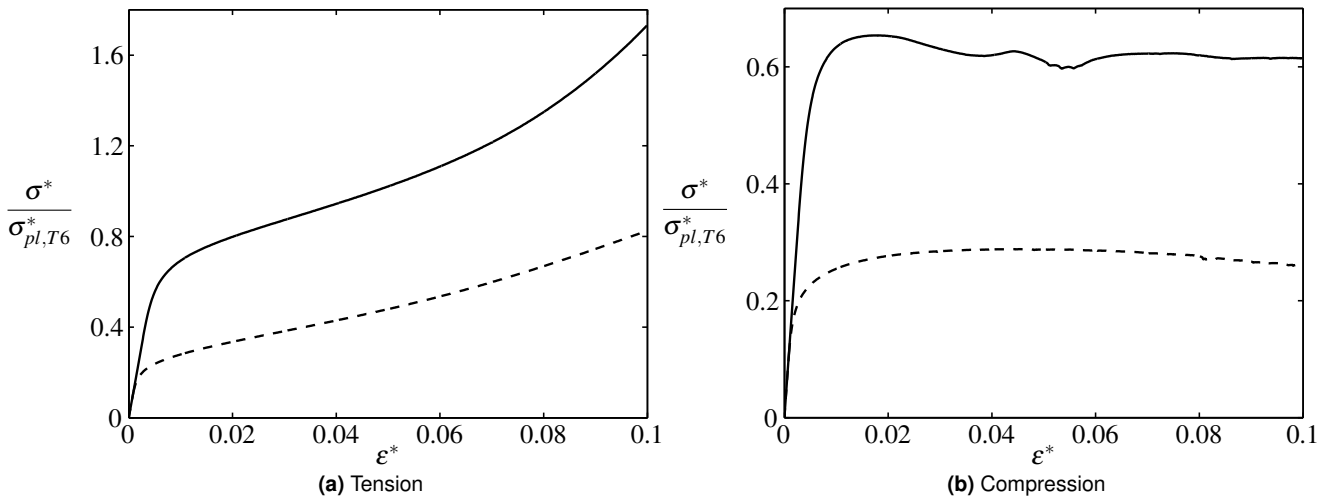


Figure 6.8: Stress strain curves for T6 (solid lines) and O (dashed lines) Voronoi networks in tension and compression.

likely. The stress strain curves of a T6 foam for compression have after the peak stress clear hills and valleys in their curves. These valleys form when the materials softens which corresponds to the formation of a band. When the stress strain curve starts to harden displacements in the current band reach a limit and the deformation switches to another band. A hill forms till the displacements have moved to the other band after it moves to a new band etc. Annealed foams do not show these hills and valleys. Because of the higher hardening exponent plasticity spreads further throughout the struts and hinges are less likely to be formed. Hence, making the formation of bands less likely.

6.3.2 Hardening

This study is completely analogous to the study performed in section 5.2.3. See figure 6.9. Also here the same conclusions hold. For fixed geometry the foam's hardening exponent matches the solid material's hardening exponent and it is independent of relative density. If geometry is updated the foam's hardening exponent does not match the solid material hardening exponent anymore. The difference is between the two hardening exponents is now even larger than for the unit cell and it also is dependent on relative density.

6.3.3 Failure

With the coupled model described in chapter 2 the exact stress in the top and bottom fibers of each beam element can be extracted. If one of these stresses exceeds the failure stress mentioned in table 6.1 the element will be set failed. If an element in a strut exceeds this failure stress, the strut also will be regarded as failed and all other beam elements in this strut will cease to be monitored during the remainder of the simulation. Note that the stresses are only *monitored*, there is no feedback to the simulation when a struts is set as failed, i.e. there is no unloading and the stresses in the beams and struts can continue to increase. We now define a damage parameter D , which is defined as the number of failed struts divided by the total number of struts.

Figure 6.10a shows the stress curves of a T6 and O Voronoi for different relative densities. The relative densities are mentioned inside the figure next to each curve. Also the point of failure for the

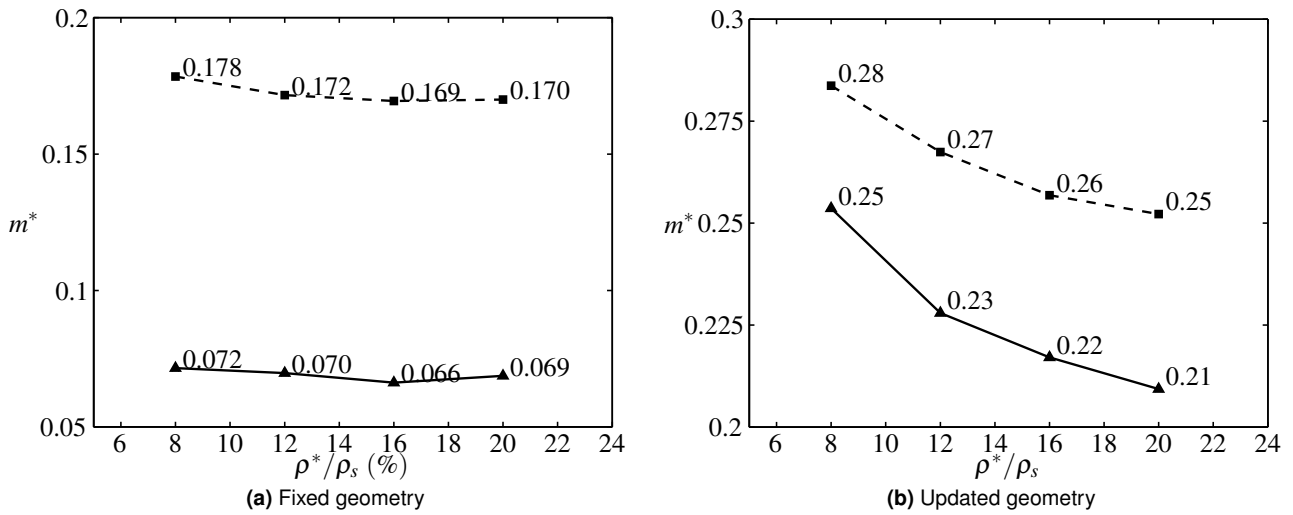


Figure 6.9: m^* versus relative density for a Voronoi structure of 16×20 cells.

complete structure is indicated in this figure. This point of failure is defined at the moment when the damage exceeds $D = 0.25$, which is drawn by dotted in figure 6.10b. This figure shows the damage curves versus strain for both heat treatments. The fact that the O Voronoi network starts failing at higher strains but lower stresses than the T6 Voronoi network is in accordance with the solid material curves shown in figure 6.2. For T6 damage seems to be increasing much faster than for the annealed curve. As already is pointed out the behaviour of T6's solid material is much alike a perfect plastic material. Both materials easily form hinges close to triple points, making the struts in these material easilier align. When struts are aligned the structure will be more rigid and stresses will therefore also increase more, causing the damage parameter to increase faster. This aligning effect does not occur (or at least with a smaller impact) in the O Voronoi network. Also observe the fact that for higher relative densities the damage increases faster. If the relative density is higher, the strut thickness will be larger. Thicker struts are more rigid and require more stress to achieve the same amount of straining compared to a thinner strut. If stresser increase faster, the damage

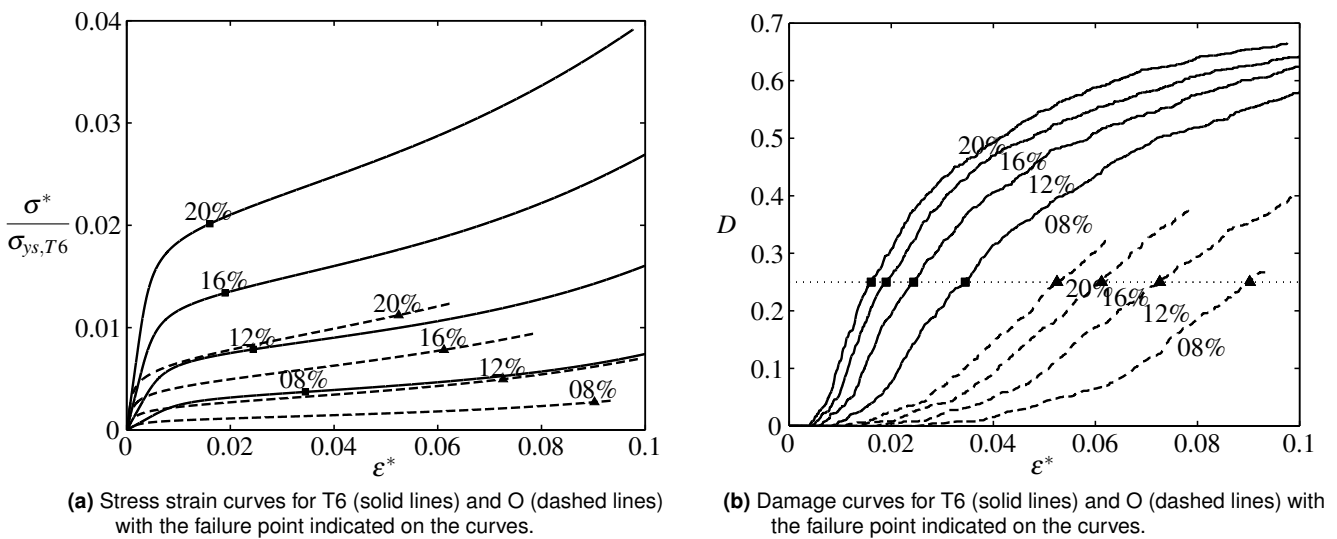


Figure 6.10: Stress strain curves and damage curves for a Voronoi network in tension.

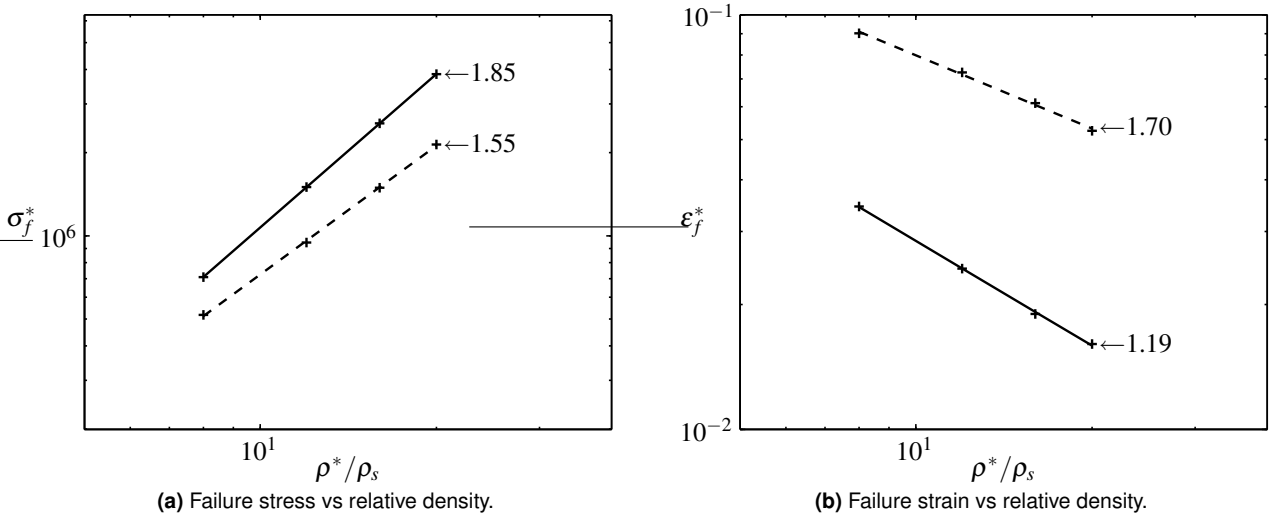


Figure 6.11: Failure stress (σ_f^*) and failure strain (ε_f^*) versus relative density for T6 (solid lines) and O (dashed lines) in log-log scales.

parameter will in its turn also increase faster, as we observe in figure 6.10b.

Finally we will examine the failure stress (σ_f^*) and failure strain (ε_f^*) as a function of relative density. These results are plotted in figure 6.11 on a log-log scale. For both heat treatments the failure stress and failure strain scale with a power to relative density. These powers are indicated next to curves in the figure. For the failure strain the absolute value of the power is shown. For an elastic material, we know that the yield stress scales with a power of two and yield strain scales with a power of minus one. For a foam with an elastic material we can write

$$\left[\frac{\sigma_{pl}^*}{\sigma_{ys}} \right]_2 = \left[\frac{E^*}{E_s} \right]_3 \left[\frac{\varepsilon_{pl}^*}{\varepsilon_{ys}} \right]_{-1}, \quad (6.1)$$

where the subscripts indicate the power of scaling of the ratio between the brackets. If this is compared to the scaling of the failure stress and strain we see that the total of both powers still is about three (if we add up the absolute values), however it has shifted to the power of the failure strain. In the range (in the stress strain curves) where all the failure stresses and strains occur, the foam is behaving in an elastic-plastic manner. This seems to change the powers in expression (6.1). Another conclusion we can draw from figure 6.11 is that the T6 Voronoi fails at higher stresses but lower strains. The exact opposite is the case for the O Voronoi, these Voronoi seem to fail at higher strains, but lower stresses. When both heat treatments are compared, we conclude that T6 Voronoi fail in a brittle manner, while the O Voronoi fail in a ductile manner.

7

Conclusion

In this chapter an overview will be given of the most important conclusions drawn throughout this thesis. Additionally, a few recommendations are listed aimed at future research in modeling of aluminum foams.

7.1 Conclusion

- The model used in this thesis is able to capture the gradual plastification of a strut cross-section and it can do this for different boundary conditions where coupling of axial strains and curvature is included.
- A postprocessing procedure called ‘strain mapping’ can be used to visualize the strain distribution inside a foam sample.
- At a sample size of 16×20 cells convergence is reached. Convergence in Young’s modulus, yield stress (in tension) and peak stress (in compression) supports this.
- The coupled and uncoupled model produce nearly the same results for regular hexagonal honeycombs. For biaxial straining the uncoupled model is not accurate anymore.
- The regular hexagonal honeycombs’ and Voronoi network’s yield stress and Young’s modulus scale according to the scaling relationships described in literature [1].
- For linear hardening the plastic modulus of regular hexagonal honeycombs and Voronoi networks does not scale with the same power as its theoretical relationship. A synergy between geometrical and material hardening is the cause of this. The error (compared to the theory) is larger for Voronoi, than for regular hexagons, since Voronoi are significantly more geometry dominated.

- When the geometry of power law hardening foam is frozen, its hardening exponent will match the hardening exponent of the solid material. When geometry is updated, the hardening exponent of the foam ceases to match the solid material's hardening exponent and becomes dependent on relative density.
- If the hardening exponent of the solid material is high, deformation spreads throughout the structure. When the hardening exponent is low deformation will localize more.
- When the T6 and O heat treatments are compared, we conclude that T6 Voronoi fails in a more brittle manner, while the O Voronoi fail in a more ductile manner.

7.2 Recommendations

- A more realistic model of the non-uniform cross-section should be implemented. How does the non-uniformity affect the behaviour of 2D foams?
- The influence of actual precipitates is not studied yet. By modifying the hardening exponent and yield stress of the foam, reasonable simulations were performed of T6-strengthened and annealed foams in this thesis. What will precipitates contribute to this?
- The hardening exponent of the foam depends on material hardening and geometry hardening. The foam's hardening exponent will look like

$$m^* = m_s + m_g(m_s, \rho^*/\rho_s, \epsilon_{ys}), \quad (7.1)$$

but how does m_g depend on m_s , ρ^*/ρ_s and ϵ_{ys} ?

- In experiments the majority of bands of collapsed cells are horizontal. Why do bands of collapsed cells in 2D foams always appear at angle of 60° to loading direction?
- All of the results presented here are for 2D foams. How will the conclusions change when the simulations are performed in 3D?

8

Acknowledgements

During this Master's project I had many help from a lot of people. First of all I would like to thank my supervisors. Kodanda, who was always there to answer my questions or help me with any problem whatsoever and Patrick with his stimulating advice and guidance, thank you. Secondly, I would like to thank Emiel Amsterdam, Hedde van Hoorn, Jeff de Hosson and Johan de Vries for the many discussions, comments and feedback during the foam meetings. They have been very helpful and inspiring. Ofcourse, I need to thank all of the members of the $\mu\text{Me}\chi$ group whom I have worked with. Erik, Yor, Monica, Ashok, Ratna, Ranjeet, Can, Syed, Goran, Peter, Jorn, Ria, Radu, Andreas, Serge, Teun and Cihan, thanks for the great time during working hours, all those colloquia and nerd dinners! Finally, I thank all of my friends and family in supporting me in my research. Without you, I could not have accomplished this.

Sietze van Buuren
November, 2007

Appendices

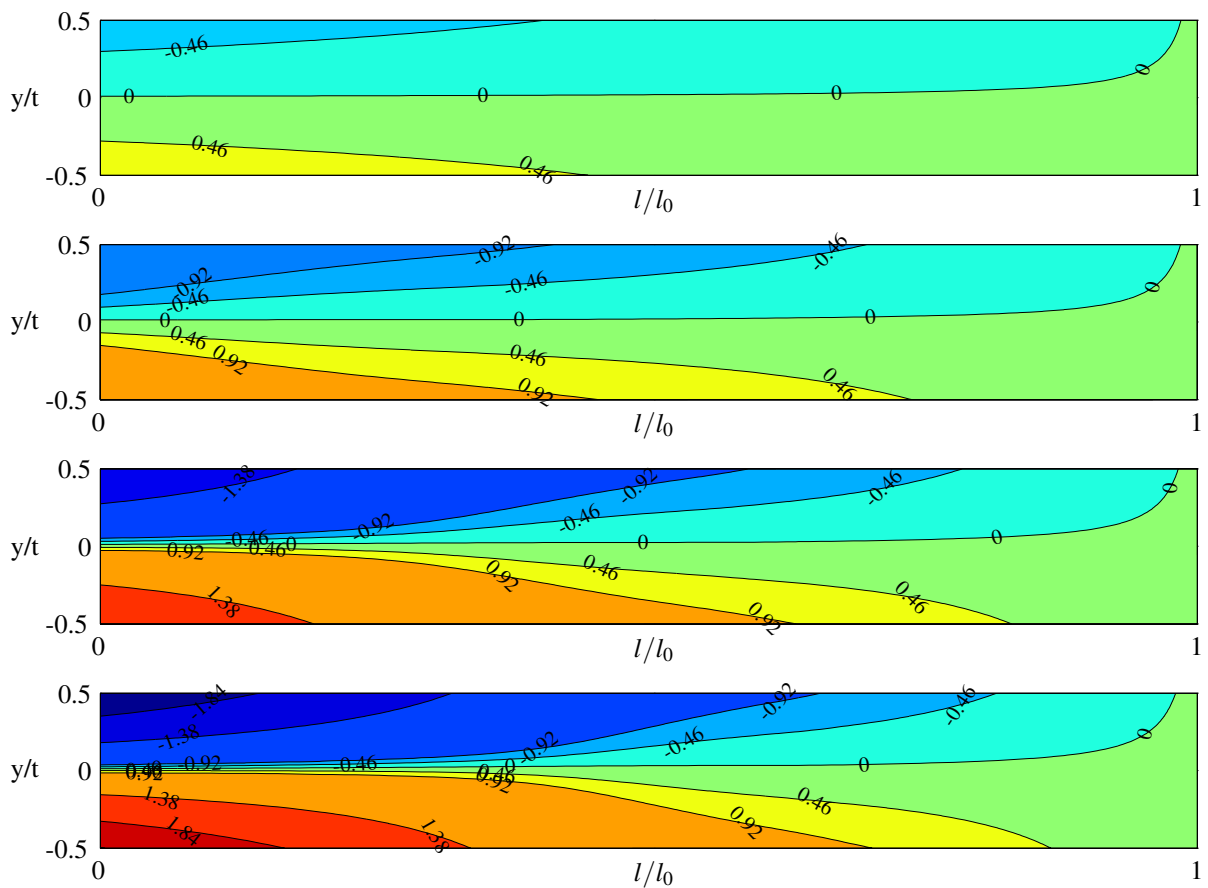


Figure 8.1: Stress contour plots at the different points on the stress strain curve for linear hardening and the free boundary conditions (from top to bottom 1-4).

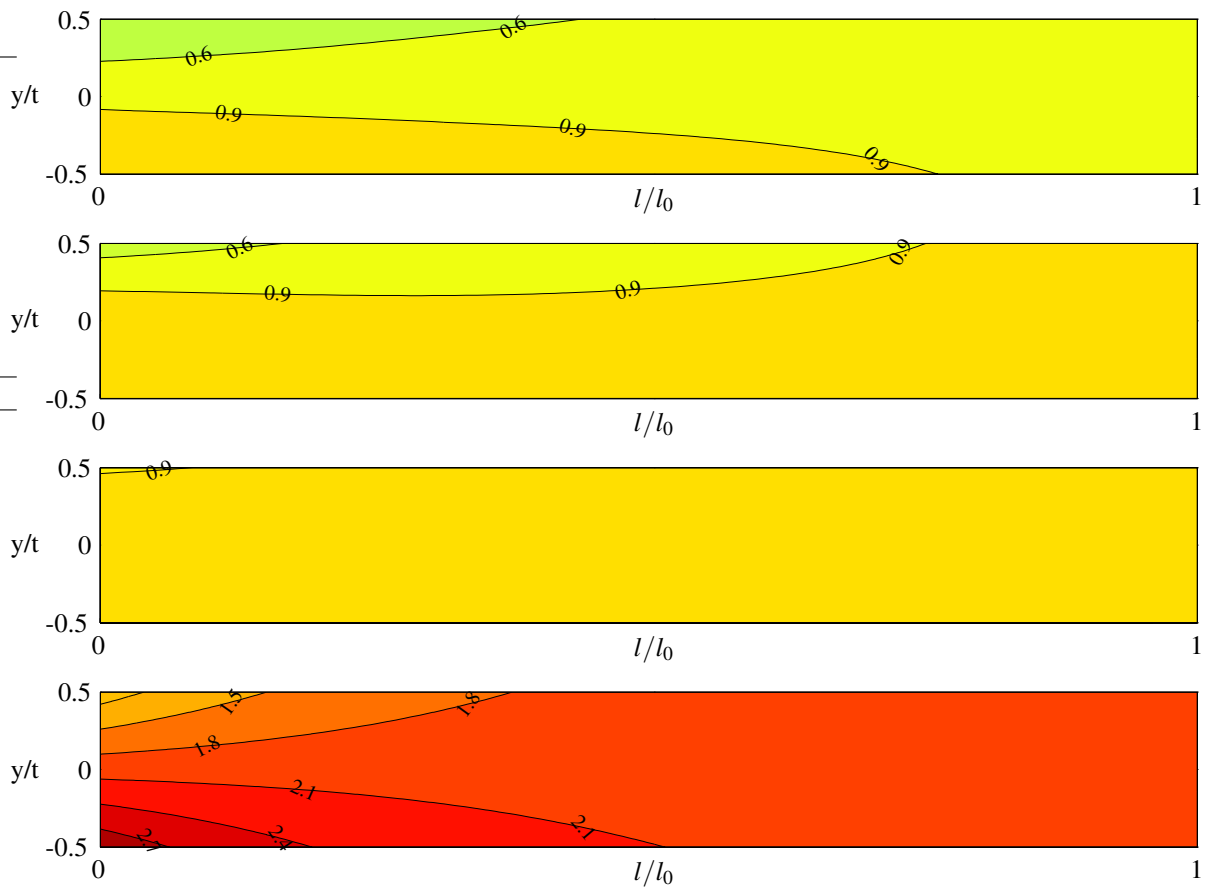


Figure 8.2: Stress contour plots at the different points on the stress strain curve for linear hardening and the constrained boundary conditions (from top to bottom 1-4).

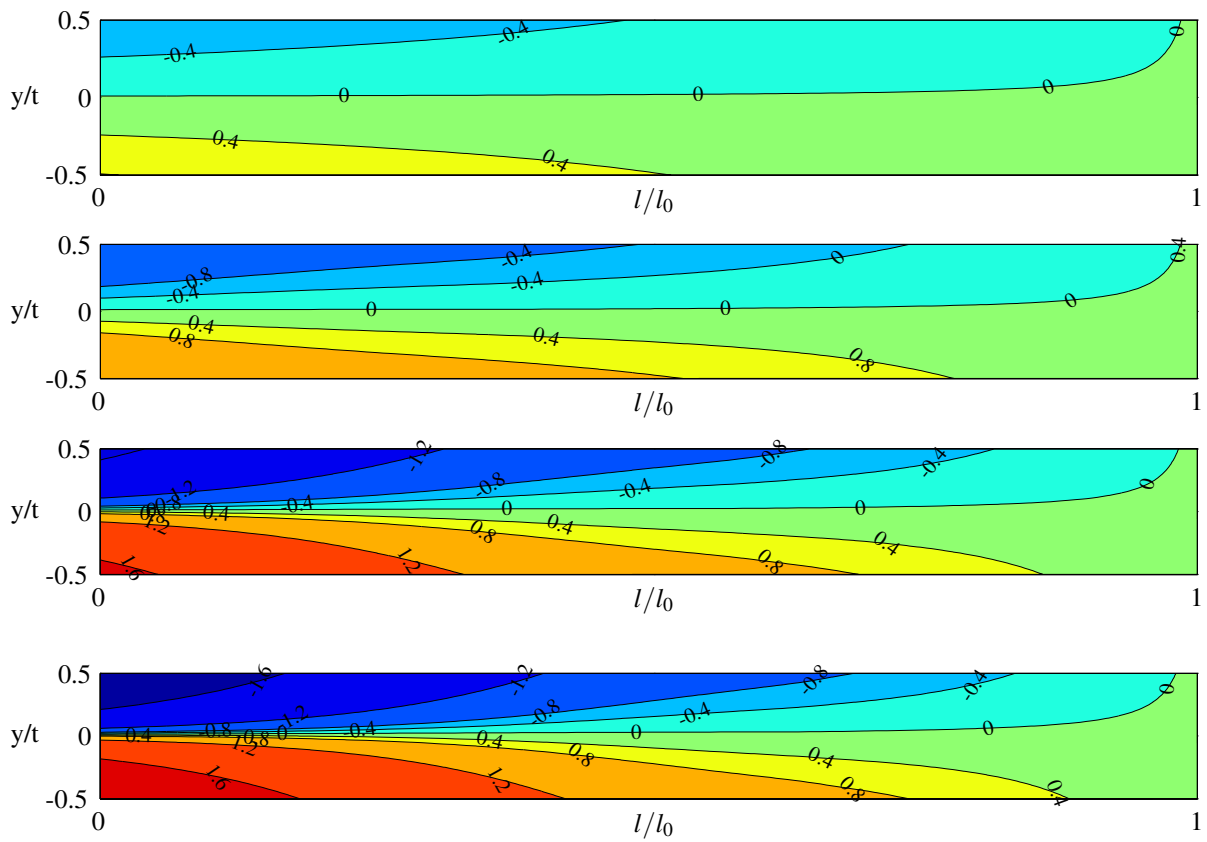


Figure 8.3: Stress contour plots for power law hardening with free boundary conditions at the different points on the stress strain curve (from top to bottom 1-4).

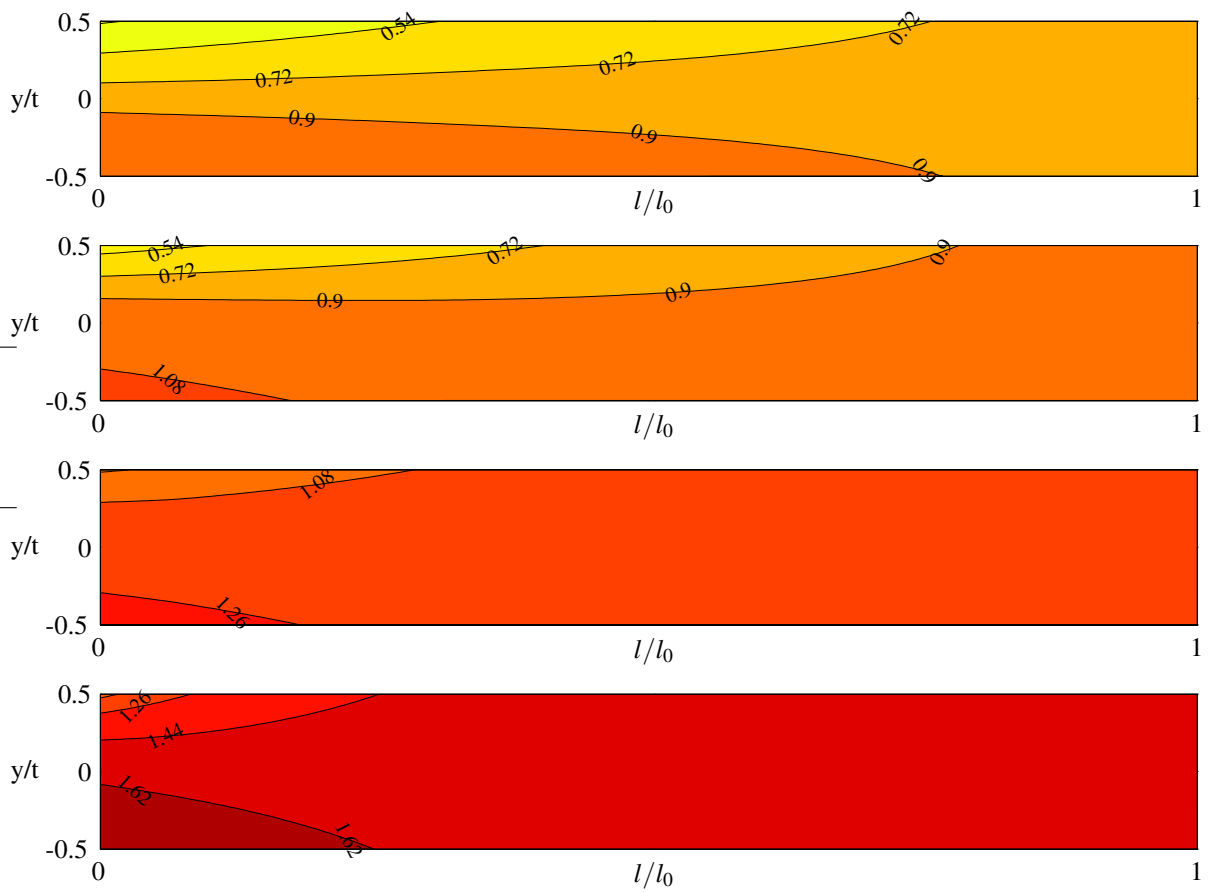


Figure 8.4: Stress contour plots power law hardening with constrained boundary conditions at the different points on the stress strain curve (from top to bottom 1-4).

References

- [1] L.J. Gibson and M.F. Ashby, *Cellular Solids, Structure and Properties*, Cambridge University Press, 1997.
- [2] K.R. Mangipudi et al *Fracture of Metal Foams*, Local approach to fracture 9th European Mechanics of Materials Conference, May 2006.
- [3] D.L. Logan, *A first course in the finite element method using Algor*, PWS Publishing company, Boston 1997.
- [4] L.J. Gibson, *Mechanical behaviour of metallic foams*, Annual reviews of material science, 2000.
- [5] C. Tekoğlu, *Size effects in cellular solids*, Rijksuniversiteit Groningen, January 2007.
- [6] J. Despois, R. Mueller, A.Mortensen, *Uniaxial deformation in microcellular metals*, Acta Materialia, **54** (2006) 4129.
- [7] J. Zhou, S. Allameh, W.O. Soboyejo, *Microscale testing of the strut in open cell aluminum foams*, Journal of Material Science **40** (2005) 429.
- [8] J. Zhou, Z. Gao, A.M. Cuitino, W.O. Soboyejo, *Effects of heat treatment on the compressive deformation behavior of open cell aluminum foams*, Materials science and engineering A **386** (2004) 118.
- [9] H.X. Zhu, S.M. Thorpe, A.H. Windle, *The geometrical properties of irregular two-dimensional Voronoi tessellations*, Philosophical Magazine A **81** (2001) 2765.
- [10] O.C. Zienkiewicz and R.L. Taylor, *The Finite Element Method, Volume 1: The Basis*, 5th edition, Butterworth-Heinemann, Oxford, 2000.
- [11] H.Harders et al *Influence of cell wall shape and density on the mechanical behaviour of 2D foam structures*, Acta Materiala, **53** (2005) 1335.
- [12] A-F. Bastawros, H. Bart-Smith, A.G. Evans, *Experimental analysis of deformation mechanisms in a closed-cell aluminum alloy foam*, Journal of Mechanics and Physics of Solids, **28** (2000) 301.
- [13] M.J. Silva, L.J. Gibson, *The effects of non-periodic microstructure and defects on the compressive strength of two-dimensional cellular solids*, International Journal of Mechanical Science, **39** (1997) 549.

-
- [14] M.J. Silva, W.C. Hayes, L.J. Gibson, *The effects of non-periodic microstructure on the elastic properties of two-dimensional cellular solids* International Journal of Mechanical Science, **37** (1995) 1161.